Precision Measurements of Electron-Proton Elastic Scattering Cross Sections at Large Q^2

by

Longwu Ou

B.S., University of Science and Technology of China (2011)

Submitted to the Department of Physics
in partial fulfillment of the requirements for the degree of

Doctor of Philosophy in Physics

at the

MASSACHUSETTS INSTITUTE OF TECHNOLOGY

February 2019

Signature redacted

Author .....
Department of Physics
November 13, 2018

Signature redacted

Certified by ....
Or Hen
Assistant Professor of Physics
Thesis Supervisor

Signature redacted

Certified by .....
Shalev Gilad
Principal Research Scientist
Thesis Supervisor

Signature redacted

Accepted by .....
Nergis Mavalvala
Associate Department Head, Physics

Precision Measurements of Electron-Proton Elastic Scattering Cross Sections at Large Q^2

by

Longwu Ou

Submitted to the Department of Physics
on November 13, 2018, in partial fulfillment of the
requirements for the degree of
Doctor of Philosophy in Physics

Abstract

The electromagnetic form factors are fundamental quantities characterizing the internal structure of the nucleon. Their measurements have provided significant insight into the spatial distribution and interaction of quarks inside the proton. The knowledge of high Q^2 form factors proves essential in understanding the properties of quantum chromodynamics in the transition region from non-perturbative to perturbative behavior. It also provides important links to generalized parton distributions, which describe the three-dimensional structure of hadrons at the parton level.

In view of the significant theoretical research activities in this field, high quality experimental data are crucial for providing stringent tests and benchmarks to guide and test different models. The form factors can be accessed in experiments by measuring elastic scattering of electrons off a hydrogen target. Experiment E12-07-108, which took place at the Thomas Jefferson National Accelerator Facility, conducted precise measurements of the unpolarized e-p elastic scattering cross section over a Q^2 range of 0.6–16.5 GeV^2. This thesis presents the results for 7 kinematic settings with total uncertainties that are 1.5 times smaller than those of the existing data at large Q^2. The proton magnetic form factors were extracted using a parameterization of the form factor ratio obtained from recent polarized e-p scattering experiments. Comparisons to existing global and phenomenological fits are presented.

Thesis Supervisor: Or Hen
Title: Assistant Professor of Physics

Thesis Supervisor: Shalev Gilad
Title: Principal Research Scientist

Acknowledgments

This thesis marks the conclusion of my adventure as a graduate student at MIT. This journey is made a success only due to the support and efforts of many, many people. I hope to express my sincere gratitude to those who have helped me, guided me and loved me in these years.

First of all, I would like to thank Prof. William Bertozzi for giving me the opportunity to join the Nuclear Interaction Group and presenting to me the various intriguing physics programs at Jefferson Lab that our group was working on during my early days at MIT. His close attention to the young students and researchers also impressed me deeply. I was more than surprised to receive an email with his best wishes the night before my dissertation defense.

Special thanks go to my thesis advisor, Dr. Shalev Gilad, for his continuing guidance, encouragement and support throughout my graduate study at MIT. Many enlightening discussions with him helped me through the experiment, data analysis and writing of this thesis.

I would also like to thank Prof. Or Hen and all the research scientists and students working at Hen Lab. I benefited from countless useful presentations and discussions in the weekly meeting of Hen Lab and learned a great deal about the short range correlations in the nuclei in my last one and a half years at MIT.

I would like to thank my academic advisor Prof. Gunther Roland for his careful guidance in my graduate courses. Many thanks to my thesis committee members, Prof. Robert Redwine and Prof. Robert Jaffe, for their valuable comments on this thesis.

I also want to express my gratitude to the scientists and staff of Jefferson Lab and the Hall A collaboration, who made this work possible. In particular, the spokespersons and students of Experiment E12-07-108 deserve credit for their efforts and contributions to make the experiment a great success. Individually, I sincerely appreciate Dr. Bogdan Wojtsekhowski and Prof. Eric Christy for leading the E12-07-108 analysis team and providing many, many insightful suggestions for resolving different prob-

lems I encountered along the way. I was very impressed by not only their dedication to high quality physics results but also their passion and patience while working with young students. My appreciation also goes to the post-docs, Vincent Sulkosky and Kalyan Allada. They helped me get acquainted with the Hall A instrumentations quickly and guided me through my first several projects at Jefferson Lab. I also want to thank the fellow students of Experiment E12-07-108, Barak Schmooker, Thir Gautam, Yang Wang, and Bashar Aljawrneh, for many experiences that we have shared while working on the experiment, such as taking night shifts during the days of data collection, and collaborating to fix numerous hardware components of the detectors. They constitute many of the fond memories I take with me from Jefferson Lab.

My sincere gratitude also goes to my friends that I have had while at MIT. Special thanks go to Dr. Xuan Wei, who gave me tremendous support during my early days at MIT and helped me get used to the environment and life in a then strange country. I still remember that he agreed with no hesitation to teach me how to drive, and was my only driver during my move to Virginia. I couldn't imagine how much more difficult my graduate life would have been without his kind friendship. My appreciation also goes to the many friends in our "division-2" basketball mailing list, including Zhan Su, Ningren Han, Yichen Shen, and Ruixun Zhang. The weekly basketball game was a great idea to keep us fit, sane and united strongly. I would also like to thank the friends I knew during my work at Jefferson Lab: Wei Liu, Tong Su, Chao Gu, Yuxiang Zhao, Li Ye, Lei Xing, Chao Peng, Ying Jin, Shujie Li, Hanjie Liu, Kai Jin, Jixie Zhang, Jie Liu, Mike Nycz, Yi Qiang, too many to name all. The uncounted interesting card games I have had with many of them greatly enriched my life in Newport News, and made the transition from living in a big city to staying at a small town much easier.

Finally, my deepest appreciation goes to my family, without whose endless love and support none of the accomplishments that I have made so far could ever be possible. I also want to express my special love to my girlfriend, Dien Nguyen. Meeting her is the best thing that has happened to me in my life. I would like to thank her for all her love and understanding during all these years together.

Contents

List of Figures

List of Tables

Chapter 1

Introduction

The electromagnetic form factors are fundamental quantities characterizing the underlying structure of the nucleon. At low momentum transfers, they are directly related to the distribution of electric and magnetic charge inside the proton. At intermediate to high momentum transfers, they reveal the properties of quark dynamics at moderate inter-quark separation and give important information about the strong force in the transition region from strong coupling and confinement to the perturbative regimes of quantum chromodynamics (QCD). The proton form factors have been extracted over a wide kinematic range in the last 60 years by various experiments measuring the elastic scattering of electrons off a hydrogen target. However, data at large momentum transfers have significant uncertainties, which limits the precision of the extracted information. Experiment E12-07-108 in Hall A at Jefferson Lab performed precision measurements of the electron-proton elastic scattering cross sections at momentum transfers up to $16.5\,\mathrm{GeV}^2$. The results at large momentum transfers improve the precision over the previous measurements by a factor of 2. These data will significantly improve the existing knowledge of the proton structure and provide constraints on the predictions of various theoretical models.

1.1 Overview

The structure of nucleons is one of the central topics in the study of nuclear physics. The relative simplicity of the structure of a single nucleon makes it an ideal object for understanding the underlying mechanism of nuclear interactions. Experimental studies are most often carried out in the form of high energy scattering experiments, where particles are accelerated to a large center-of-mass energy, collide, and the products of such a reaction are recorded by various detectors and electronics. Historically, this methodology has been proven a powerful technique for unravelling the structure of nucleons. For example, after the first indications of an internal structure of the nucleons from the deviations of their magnetic moments from the values expected for point-like Dirac particles [1], the detailed spatial distribution of the electromagnetic component inside the nucleon was first revealed by elastic electron scattering experiments on the proton and deuteron in the 1950s [2, 3]. Since then, the frontier of our knowledge on the structure of nucleons has been pushed forward by performing higher precision, higher energy scattering experiments, one of the cornerstones being the demonstration of the existence of partons inside the nucleon by a deep inelastic scattering (DIS) experiment at the Stanford Linear Accelerator Center (SLAC) [4].

After more than half a decade of theoretical and experimental studies, it is now commonly accepted that nucleons are composed of fundamental particles—quarks and gluons—interacting with each other through the strong interaction described within the framework of Quantum Chromodynamics (QCD). When the scattering process involves sufficiently large transfers of energy and momentum, the quarks are effectively viewed at very small length scales, where their interactions become asymptotically weaker, and the QCD Lagrangian can be solved in a perturbative manner, whose results have been verified by numerous experiments. On the contrary, at low energies the interaction is strong, making the pursuit of a rigorous prediction based on the QCD extremely difficult. The latter scenario is commonly referred to as the non-perturbative regime, where various phenomenological models are proposed to explain the experimental results.

Elastic scattering of electrons off a nucleon target is of special interest to both nuclear theorists and experimentalists. On the one hand, the usage of an electromagnetic probe means that the interaction takes place through the exchange of a virtual photon and is dictated by quantum electrodynamics (QED), whose effects can be exactly calculated to any order. On the other hand, the particles involved in this reaction are a structureless electron and the simplest baryon, and the final state is unambiguously determined, which makes it possible to perform precision measurements.

From a theoretical standpoint, such reactions are typically studied in the framework of one-photon-exchange (OPE) approximation, where a single virtual photon is exchanged between the incident electron and the struck proton. In this formalism, the e-p elastic cross section can be parameterized by two scaler functions of the four-momentum transfer squared Q^2, G_{Ep} and G_{Mp}, which are also known as the proton electric and magnetic form factors. These two form factors characterize the electric and magnetic interactions between the virtual photon and the proton in the so-called Breit frame [5], where the momentum of the proton is reversed in the scattering process.

Measurements of proton electromagnetic form factors date back to the early usage of particle accelerators in nuclear physics experiments and were based on the results of unpolarized elastic cross section experiments. After several decades' arduous effort, the proton form factor data have had much improved precision and cover a Q^2 range up to $30\,\mathrm{GeV}^2$, which provides tremendous insight into the internal structure of the nucleon and QCD. One prominent feature revealed by these data is the scaling of electric and magnetic form factors at large momentum transfer. This behavior is consistent with the dimensional scaling rule [5] in perturbative QCD. However, since the elastic scattering cross section decreases rapidly as Q^2 goes up, a very limited number of measurements of the form factors were carried out at high Q^2, and their uncertainties are large (Fig. 1-1). With the construction of new electron accelerator facilities at the Thomas Jefferson National Accelerator Facility, new physics programs targeted at understanding the structure of nucleons and nuclei at large Q^2 were proposed. A large number of nuclear experiments in these programs use the elastic

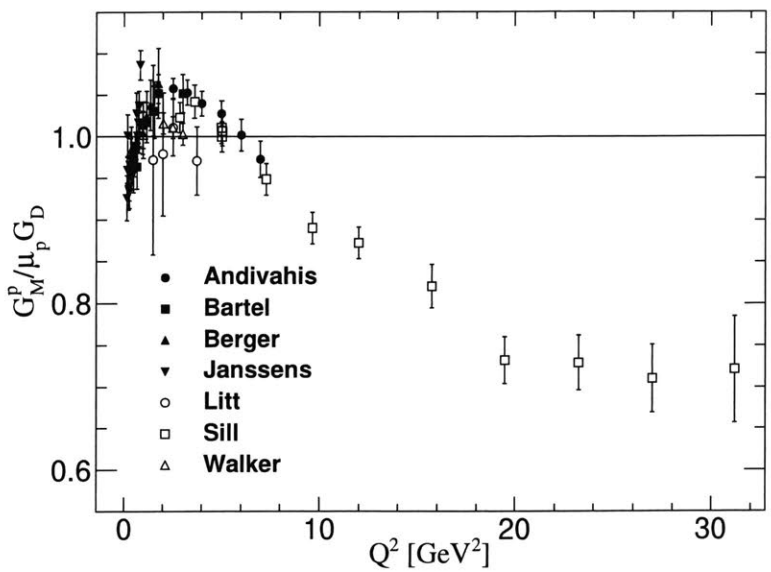

Figure 1-1: The proton magnetic form factor G_{Mp}, normalized by the dipole form factor G_D (Sec 1.4), extracted from unpolarized electron scattering cross section measurements. The data included in this figure come from Andivahis [6], Bartel [7], Berger [8], Janssens [9], Litt [10], Sill [11] and Walker [12] respectively.

electron-nucleon scattering cross section as a normalization input. The existing form factor data in this Q^2 range were measured at very different kinematics and, when extrapolating to the kinematics of interest, inevitably bring in additional uncertainties. Thus the old data cannot fulfill the requirement of future high precision nuclear experiments, and new precision measurements of e-p elastic cross sections are called for.

Precise data on the e-p elastic cross section are also essential for understanding a puzzle that lies in the form factor physics itself, which revealed itself as a striking result about twenty years ago. At that time, with the advent of the technology of intense polarized electron beams, polarized targets and polarimetry, a new type of form factor measurements was performed which relied on the spin degrees of freedom of the nucleon. The polarization technique reliably measured the ratio of the electric to magnetic form factors in a Q^2 range up to 8.5 GeV^2. The data showed that the ratio decreases with Q^2, and drops to about 0.145 at $Q^2 = 8.5\,\mathrm{GeV}^2$—in stark disagreement

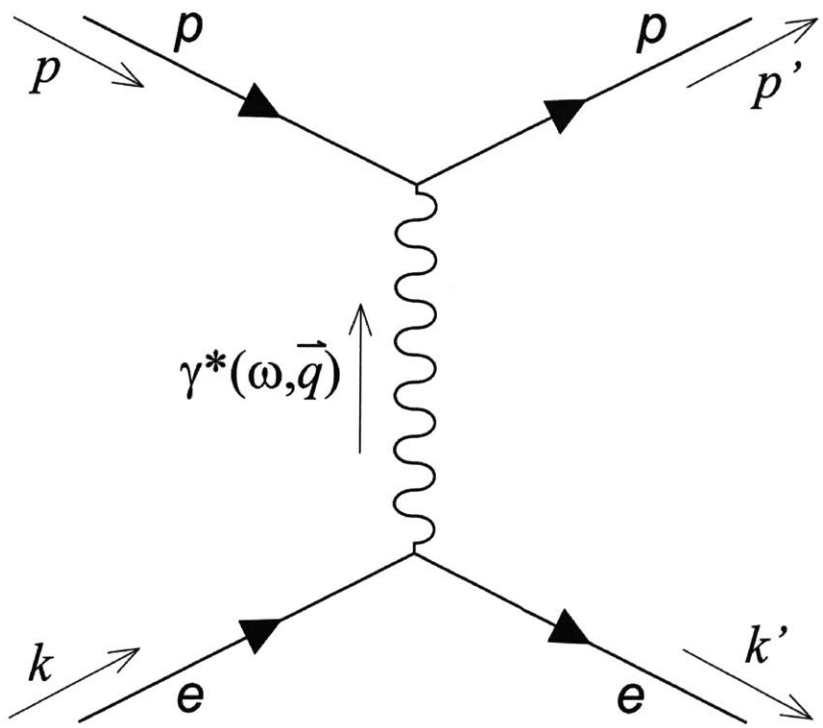

Figure 1-2: The Feynman diagram of *ep* elastic scattering in the single photon exchange approximation.

with the scaling behavior seen in the unpolarized cross section measurements. This discrepancy has led to renewed interest in the proton electromagnetic form factors at intermediate to large Q^2.

At the same time, it is intriguing to study the behavior of the proton electromagnetic form factor at large Q^2 from the theoretical point of view. The flavor-separated form factors for valence quarks can be combined with DIS data to provide insight into the structure of the nucleon within the framework of generalized parton distribution (GPD) [13, 14]. In addition, the elastic nucleon form factors can be viewed in the framework of Dyson-Schwinger equations, where they are especially sensitive to the momentum-dependent dressed-quark mass function [15]. Furthermore, the question about the onset of perturbative QCD in the elastic scattering process remains an open question and can only be answered with the availability of high precision form factor measurements at large Q^2.

This thesis presents Experiment E12-07-108, which was carried out at Hall A of

Jefferson Lab in 2015 and 2016 and measured the e-p elastic scattering cross section with improved precision over the Q^2 range of 0.66–16.5 GeV^2.

1.2 Formalism of e-p Elastic Scattering

1.2.1 Definitions

The Feynman diagram for e-p elastic scattering, in the one-photon-exchange approximation, is illustrated in Fig. 1-2. This approximation is justified due to the fact that the electromagnetic interaction is governed by the very small fine structure constant $\alpha = e^2/4\pi \simeq 1/137$. The initial and final four-momenta of the electron are denoted by $k = (E, \mathbf{k})$ and $k' = (E', \mathbf{k'})$ respectively, and $p = (E_p, \mathbf{p})$ and $p' = (E'_p, \mathbf{p'})$ are the four-momenta of the proton before and after the scattering process. According to the requirement of momentum conservation at each vertex, one can determine the four-momentum $q = (\omega, \mathbf{q})$ of the exchanged virtual photon as

$$\omega = E - E', \tag{1.1}$$

$$\mathbf{q} = \mathbf{k} - \mathbf{k'}. \tag{1.2}$$

In addition, the initial and final states are on-mass-shell for both the electron and proton in the elastic scattering process:

$$p_\mu p^\mu = p'_\mu p'^\mu = M_p^2, \tag{1.3}$$

$$k_\mu k^\mu = k'_\mu k'^\mu = m_e^2, \tag{1.4}$$

$$\tag{1.5}$$

where m_e and M_p are the masses of the electron and proton respectively. The electron mass can be safely neglected for the purpose of this thesis since all initial and final four-momenta are in the few-GeV regime. Under this approximation, the Lorentz-

invariant four-momentum transfer squared Q^2 is defined as

$$Q^2 = -q^2 = -(\omega^2 - \mathbf{q}^2) \approx 4EE' \sin^2 \frac{\theta}{2}, \tag{1.6}$$

with θ being the electron scattering angle in the laboratory frame. The constraint that the final hadronic state contains a single proton and nothing else leads to the equation:

$$x \equiv \frac{Q^2}{2M_p\omega} = 1. \tag{1.7}$$

This equation is only a function of the electron kinematics and, when combined with Eq. 1.6, determines a relationship between the initial and final electron energies and the scattering angle:

$$E' = \frac{E}{1 + \frac{E}{M_p}(1 - \cos\theta)}. \tag{1.8}$$

1.2.2 Formalism

The coupling of the electron with the virtual photon is fully described by QED. The electron current in the one-photon-exchange approximation, neglecting the trivial phase factor, is given by [16]

$$j^\mu = -e\bar{u}(k')\gamma^\mu u(k), \tag{1.9}$$

where $u(k)$ is the Dirac spinor for a spin-1/2 particle with four-momentum k, and $\bar{u}(k)$ is its Dirac adjoint:

$$\bar{u}(k) = u^\dagger(k)\gamma^0. \tag{1.10}$$

The set of Gamma matrices γ^μ, with $\mu = 0, 1, 2, 3$, are the well known Dirac 4×4 matrices that satisfy the following anti-commutation relation:

$$\{\gamma^\mu, \gamma^\nu\} = \gamma^\mu\gamma^\nu + \gamma^\nu\gamma^\mu = 2g^{\mu\nu}, \tag{1.11}$$

with $g^{\mu\nu}$ denoting the Minkowski metric:

$$g^{\mu\nu} = \begin{pmatrix} 1 & & & \\ & -1 & & \\ & & -1 & \\ & & & -1 \end{pmatrix}. \tag{1.12}$$

There are a number of equivalent representations of the Dirac matrices γ^μ that satisfy Eq. 1.11. We follow the standard "Bjorken and Drell" [17] convention and have:

$$\gamma^0 = \begin{pmatrix} 1 & 0 \\ 0 & -1 \end{pmatrix}, \quad \gamma^i = \begin{pmatrix} 0 & \sigma^i \\ -\sigma^i & 0 \end{pmatrix}, \tag{1.13}$$

where 1 denotes the 2×2 unit matrix, 0 is the 2×2 matrix of zeros, and σ^i ($i = 1, 2, 3$) is the standard Pauli spin matrix:

$$\sigma^1 = \begin{pmatrix} 0 & 1 \\ 1 & 0 \end{pmatrix}, \quad \sigma^2 = \begin{pmatrix} 0 & -i \\ i & 0 \end{pmatrix}, \quad \sigma^3 = \begin{pmatrix} 1 & 0 \\ 0 & -1 \end{pmatrix}. \tag{1.14}$$

If the proton was a structureless Dirac particle as the electron is, the hadronic current $\mathcal{J}^\mu$ would take a very similar form to Eq. 1.9. Since this is not the case, we have to write it as a general Lorentz four-vector constructed from p, p', q and the Dirac gamma matrices. Considering the constraint of on-mass-shell initial and outgoing proton and parity conservation in electromagnetic interactions, we may write the proton current as

$$\mathcal{J}^\mu = e\bar{v}(p')\Gamma^\mu v(p) = e\bar{v}(p')\Big[\gamma^\mu F_{1p}(Q^2) + \frac{i\sigma^{\mu\nu}q_\nu}{2M_p}\kappa F_{2p}(Q^2)\Big]v(p), \tag{1.15}$$

where

$$\sigma^{\mu\nu} \equiv \frac{i}{2}(\gamma^\mu\gamma^\nu - \gamma^\mu\gamma^\nu), \tag{1.16}$$

and $\kappa \simeq 1.793$ is the proton anomalous magnetic moment. The $v(p)$ and $\bar{v}(p')$ in Eq. 1.15 are the proton correspondents of the $u(k)$ and $\bar{u}(k')$ in Eq. 1.9 respectively.

The two unknown functions, F_{1p} and F_{2p}, of Q^2 are known as the Dirac and Pauli form factors of the proton, respectively. They contain information about the internal structure of the proton. In particular, $F_{1p}(Q^2)$ describes the helicity-conserving scattering amplitude, while $F_{2p}(Q^2)$ represents the helicity-flipping part. They are normalized at $Q^2 = 0$ according to

$$F_{1p}(0) = 1, \quad F_{2p}(0) = 1. \tag{1.17}$$

It is customary to work with the Sachs electromagnetic form factors G_{Ep} and G_{Mp} instead because they can be easily separated in the analysis of elastic scattering cross section experiment. They are defined as linear combinations of the Dirac and Pauli form factors:

$$G_{Ep} = F_{1p} - \frac{\kappa Q^2}{4M_p^2} F_{2p}, \tag{1.18}$$

$$G_{Mp} = F_{1p} + \kappa F_{2p}. \tag{1.19}$$

The Sachs form factors also have particular values at $Q^2 = 0$ according to the static properties of the proton:

$$G_{Ep}(0) = 1, \quad G_{Mp}(0) = \mu_p, \tag{1.20}$$

where $\mu_p = \kappa + 1$ is proton's magnetic moment.

1.3 Techniques for Form Factor Measurements

1.3.1 Rosenbluth Form Factor Separation Method

The electric and magnetic form factors can be extracted from the unpolarized electron elastic scattering cross section. We consider the scattering amplitude $\mathcal{M}_{1\gamma}$ of the Feynman diagram in Fig. 1-2, which can be expressed in terms of the electron and

proton current derived in Eqs. 1.9 and 1.15 as

$$i\mathcal{M}_{1\gamma} = \frac{i}{Q^2} j^\mu \mathcal{J}_\mu. \tag{1.21}$$

The elastic differential cross section in the laboratory frame is equal to the squared amplitude multiplied by a kinematic factor and a delta function that enforces the four-momentum conservation:

$$\mathrm{d}\sigma = \frac{|\mathcal{M}_{1\gamma}|^2}{4(k\cdot p)}(2\pi)^4\delta^4(k+p-k'-p')\frac{\mathrm{d}^3\mathbf{k}'}{(2\pi)^3 2E'}\frac{\mathrm{d}^3\mathbf{p}'}{(2\pi)^3 2E'_p}. \tag{1.22}$$

The electron mass has been neglected in deriving Eq. 1.22. The integral over $\mathbf{k}'$ and $\mathbf{p}'$ can be performed explicitly to yield

$$\frac{\mathrm{d}\sigma}{\mathrm{d}\Omega} = \frac{E'^2}{64\pi^2 M_p^2 E^2}|\mathcal{M}|^2. \tag{1.23}$$

In an unpolarized electron scattering experiment, the detectors are not sensitive to either the polarization states of the initial particles or those of the final particles. Thus Eq. 1.23 is averaged over the spins of the incident particles and summed over those of the outgoing particles to generate the formula for unpolarized cross section:

$$\begin{aligned}\frac{\mathrm{d}\sigma}{\mathrm{d}\Omega} &= \left(\frac{\mathrm{d}\sigma}{\mathrm{d}\Omega}\right)_{\text{Mott}}\left\{\frac{G_{Ep}^2(Q^2)+\tau G_{Mp}^2(Q^2)}{1+\tau} + 2\tau G_{Mp}^2(Q^2)\tan^2\frac{\theta}{2}\right\} \\ &= \left(\frac{\mathrm{d}\sigma}{\mathrm{d}\Omega}\right)_{\text{Mott}}\frac{\epsilon G_{Ep}^2(Q^2)+\tau G_{Mp}^2(Q^2)}{\epsilon(1+\tau)}.\end{aligned} \tag{1.24}$$

In Eq. 1.24 we have introduced the kinematic variables $\tau \equiv \frac{Q^2}{4M_p^2}$ and the virtual photon polarization $\epsilon \equiv (1+2(1+\tau)\tan^2\frac{\theta}{2})^{-1}$ to make the final result more organized. The Mott cross section describes the scattering of a point-like Dirac particle off a spin-1/2 point target:

$$\left(\frac{\mathrm{d}\sigma}{\mathrm{d}\Omega}\right)_{\text{Mott}} = \frac{\alpha^2 cos^2\frac{\theta}{2}}{4E^2\sin^4\frac{\theta}{2}}\frac{E'}{E}. \tag{1.25}$$

Eq. 1.24 is referred to as the Rosenbluth formula for e-p elastic cross section. It contains the contribution from two parts: the electric term G_{Ep} and the magnetic

term G_{Mp}. It is worth noting that the G_{Mp} term is weighted by the kinematic variable τ relative to the G_{Ep} term. At low Q^2 where $\tau \ll 1$, the cross section is dominated by the electric form factor. However, the contribution from the magnetic form factor is enhanced at large momentum transfer, making it difficult to extract G_{Ep} with high accuracy from the measured cross sections.

The Rosenbluth separation technique takes advantage of the linear dependence on ϵ of the following reduced cross section:

$$\sigma_{\mathrm{R}} \equiv \epsilon(1+\tau)\Big(\frac{\mathrm{d}\sigma}{\mathrm{d}\Omega}\Big)/\Big(\frac{\mathrm{d}\sigma}{\mathrm{d}\Omega}\Big)_{\mathrm{Mott}} = \epsilon G_{Ep}^2(Q^2) + \tau G_{Mp}^2(Q^2). \tag{1.26}$$

The cross sections are measured at a fixed Q^2 but distinct values of ϵ by varying the incident electron beam energy and the scattering momentum simultaneously. The two form factors can then be extracted by performing a linear fit to the cross section with respect to ϵ, whose slope gives G_{Ep}^2 and the intercept is equal to τG_{Mp}^2.

1.3.2 Double Polarization Measurements

Eq. 1.24 reveals that the unpolarized cross section is a combination of the squared electric and magnetic form factor. Due to the magnetic moment of proton, the contribution from the electric term is suppressed by a factor of 10 even at intermediate Q^2 ($\sim 4\,\mathrm{GeV}^2$). In order to overcome this difficulty, it was proposed to perform measurements of the polarization variables in e-p elastic scattering, which, as can be seen here soon, are related to the interference term $G_{Ep}G_{Mp}$. Two types of experimental techniques have been applied successfully to perform such measurements. The first method uses a longitudinally polarized electron beam and an unpolarized target, where the polarization of the incoming electron is transferred to the target via exchange of a single virtual photon as shown in Fig. 1-3. In the second method, a longitudinally polarized electron beam scatters off a polarized nucleon target and the difference in the cross sections when flipping the beam helicity is measured (Fig. 1-4).

We take the recoil polarization method as an example here. In the single pho-

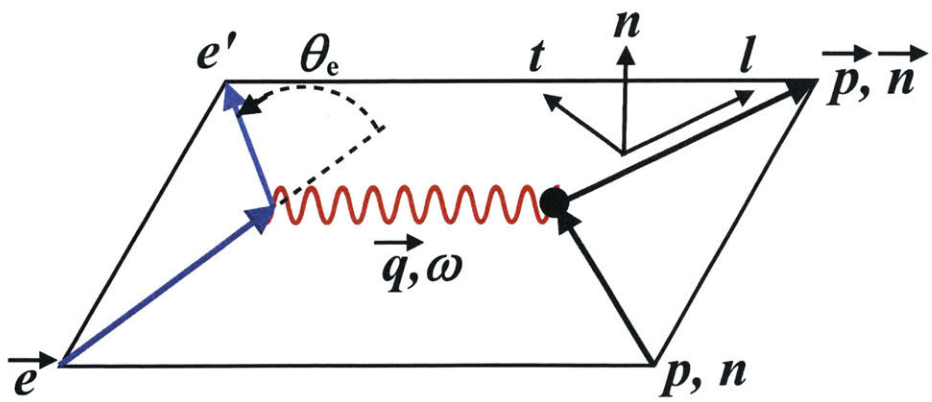

Figure 1-3: Illustration of the kinematics of recoiling polarization measurements of nucleon form factors. Reproduced from [18].

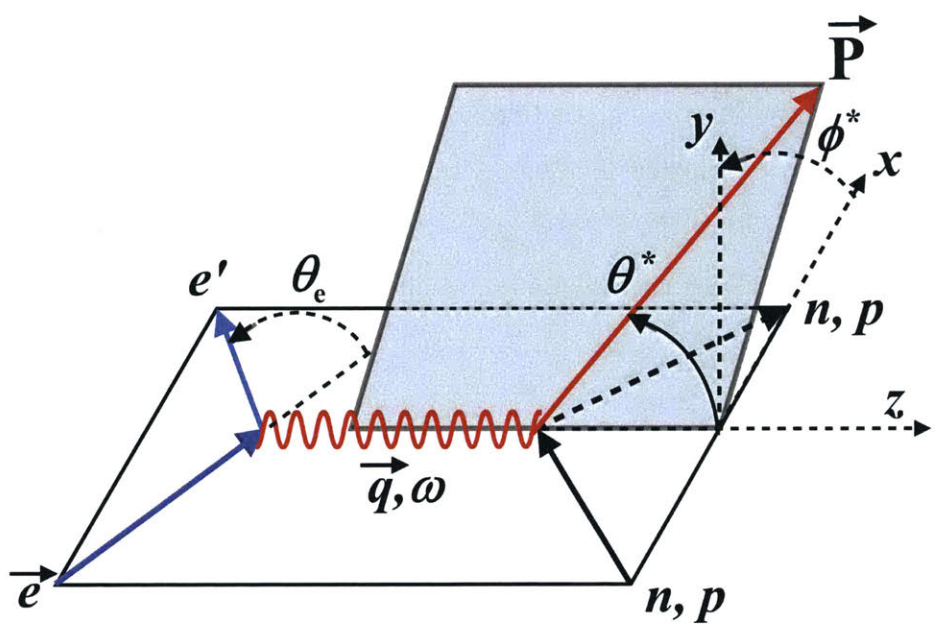

Figure 1-4: Illustration of the kinematics of polarized target asymmetry measurements of nucleon form factors. Reproduced from [18].

ton exchange approximation, the normal (P_n), longitudinal (P_l), and transverse (P_t) transferred polarization components can be expressed as a function of the Sachs form factors:

$$I_o P_n = 0, \tag{1.27}$$

$$I_o P_l = h P_e \frac{E+E'}{M_p} \sqrt{\tau(1+\tau)} \tan^2 \frac{\theta}{2} G_{Mp}^2, \tag{1.28}$$

$$I_o P_t = -h P_e 2 \sqrt{\tau(1+\tau)} \tan \frac{\theta}{2} G_{Ep} G_{Mp}, \tag{1.29}$$

where I_o is proportional to the unpolarized reduced cross section

$$I_o = G_{Ep}^2 + \frac{\tau}{\epsilon} G_{Mp}^2 \tag{1.30}$$

and $h = \pm 1$ are the beam helicity states. P_e is the magnitude of polarization, and θ is the electron scattering angle. The ratio of electric to magnetic form factor can be obtained by

$$\frac{G_{Ep}}{G_{Mp}} = -\frac{P_t}{P_l} \frac{E+E'}{2M_p} \tan \frac{\theta}{2}. \tag{1.31}$$

In a recoil polarization experiment, a Focal Plane Polarimeter (FPP) is used to simultaneously measure the transverse and longitudinal polarization components P_t and P_l by a single measurement of the azimuthal angular distribution of the proton scattered in a second target (also called an analyzer) [19]. The result thus does not depend on the knowledge of the beam polarization and the analyzing power of the polarimeter, greatly reducing the systematic uncertainties. However, only the ratio of the form factors can be extracted using the polarization measurements. A combined analysis with unpolarized cross section results is necessary for one to obtain the absolute values of G_{Ep} and G_{Mp}.

1.4 Existing Measurements of Proton Form Factors

Extractions of proton electromagnetic form factors have been performed over the last sixty years in numerous experiments. The early experiments in the twentieth

century conducted measurements of electron-proton elastic cross sections at electron accelerator facilities around the world and used the Rosenbluth technique to extract the electric and magnetic form factors. The measurements can be done with great precision at low Q^2 due to the relatively large cross section. It was then observed that even at a moderate resolution of the virtual photon ($Q^2 \lesssim 2\,\mathrm{GeV}^2$), the form factors already exhibit pronounced Q^2-dependence—a clear evidence for extended charge and current distributions in the proton. Quiet interestingly, it was found that the evolutions of G_{Ep} and G_{Mp} with Q^2 were in approximate agreement with the dipole form:

$$G_{Ep} \approx \frac{G_{Mp}}{\mu_p} \approx G_D(Q^2), \tag{1.32}$$

where

$$G_D(Q^2) = \left(1 + \frac{Q^2}{0.71\,\mathrm{GeV}^2}\right)^{-2}. \tag{1.33}$$

Following these measurements at low Q^2, elastic electron-proton scattering experiments were performed at large momentum transfer squared when accelerators able to provide stable high energy electron beams became available. In this Q^2 regime, the overall cross section is significantly reduced due to its E^2/Q^{12} dependence[1], making it difficult to achieve respectable statistical accuracy. In addition, the suppression of electric term limits the precision of extracted G_{Ep}. The highest Q^2 so far was achieved by Sill's experiment [11] at SLAC which measured the e-p cross section at forward angles for Q^2 from 3 to $30\,\mathrm{GeV}^2$. The magnetic form factor G_{Mp} was extracted under the assumption that $\mu_p G_{Ep}/G_{Mp} = 1$. At about the same time, two other experiments at SLAC extended the precision and upper range of Q^2 for performing the Rosenbluth separation technique. Ref. [12] measured the unpolarized cross section at Q^2 between 1.0 and $3.0\,\mathrm{GeV}^2$. Ref. [6] achieved a Q^2 up to $9\,\mathrm{GeV}^2$, which is still the maximum Q^2 where a measurement of G_{Ep} has been performed at this time. The G_{Mp} and G_{Ep} data extracted from some Rosenbluth separation measurements are

[1]The e-p elastic cross section is a product of the Mott cross section and the reduced cross section (Eq. 1.24). The Mott cross section (Eq. 1.25) varies with the beam energy and four momentum transfer squared as E^2/Q^4. The reduced cross section is proportional to the square of the two form factors and has an approximate Q^{-8} dependence (see Eq. 1.33). Their product thus gives the Born cross section the E^2/Q^{12} behavior.

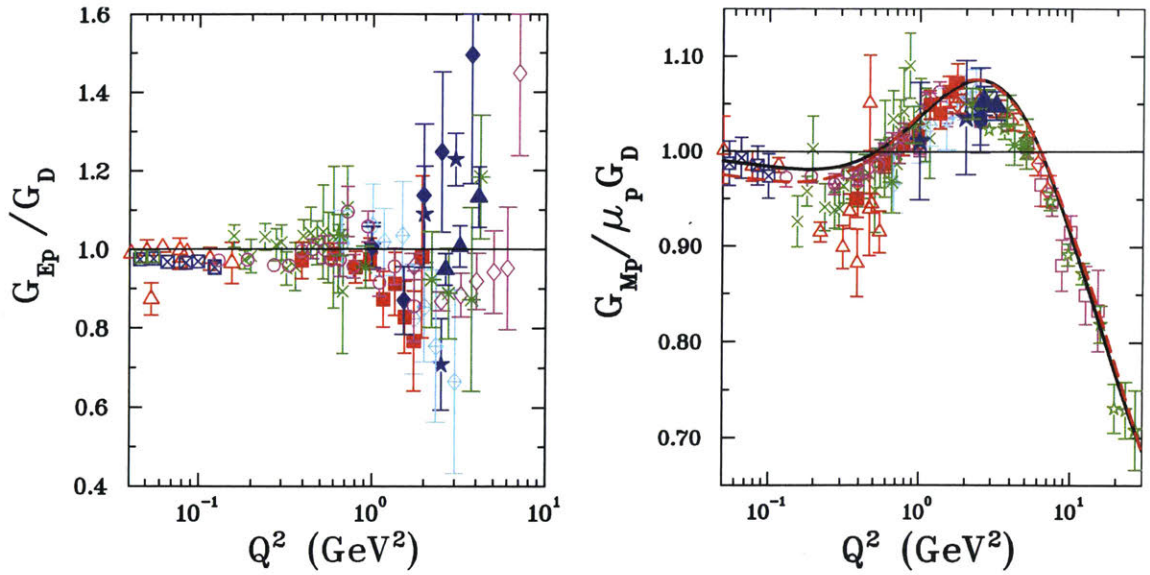

(a) G_{Ep}/G_D extracted from cross section measurements.

(b) G_{Mp}/G_D extracted from cross section measurements.

Figure 1-5: World data of G_{Ep} (left) and G_{Mp} (right) extracted by Rosenbluth separation method and normalized by the dipole form factor. The data from before 1980 are: open triangle (red) [20], multiplication sign (green) [9], open circle (magenta) [21], filled diamond (blue) [10], filled square (red) [8], crossed diamond (cyan) [7], crossed square (blue) [22] and open square (green) [23]. The SLAC data from the 1990's are filled star (blue) [12], and open diamond (magenta) [6]. The Jefferson Lab data are asterisk (green) [24] and filled triangle (blue) [25]. Additional data points at the highest Q^2 in (b), open square (magenta) [26], and open star (green) [11], were extracted from cross sections assuming $\mu_p G_{Ep}/G_{Mp} = 1$. The Solid (dashed) line is a fit by Ref. [27] (Ref. [28]). Reproduced from Ref. [18].

compiled in Fig. 1-5.

It is clear that the data for G_{Mp} have shown good consistency between different experiments up to $30\,\mathrm{GeV}^2$. They follow the dipole form reasonably well, with the deviation amounting to less than 10% at $Q^2 \lesssim 7\,\mathrm{GeV}^2$. On the other hand, the G_{Ep} results are consistent with each other only at Q^2 below $1\,\mathrm{GeV}^2$. At higher momentum transfer, almost all data sets suffer from large error bars and they scatter without a clear trend. The resulting form factor ratio $\mu_p G_{Ep}/G_{Mp}$ from unpolarized cross section measurements is presented in Fig. 1-6. These measurements indicate that the electric and magnetic form factors scale with increasing Q^2, even though the uncertainties become significant at large Q^2 due to the reduced sensitivity to G_{Ep}.

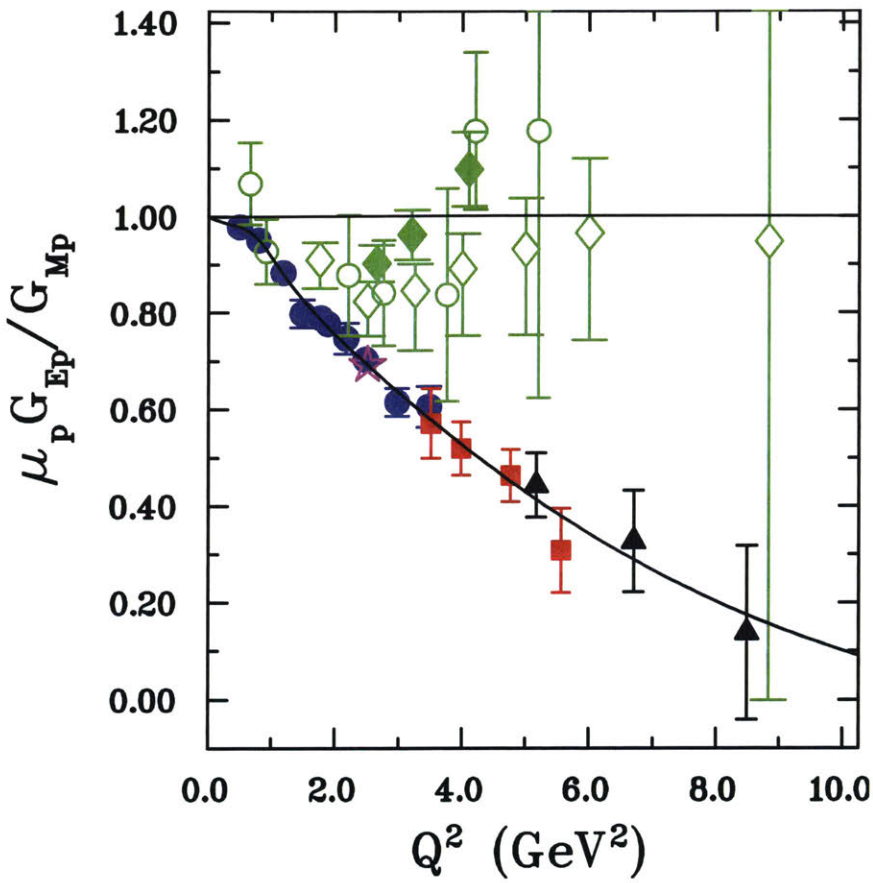

Figure 1-6: The form factor ratio $\mu_p G_{Ep}/G_{Mp}$ extracted from the three large Q^2 recoil polarization experiments at Jefferson Lab (blue filled circle [19], magenta filled star [29], red filled square [30] and black filled triangle [31]) compared to Rosenbluth separation data (green), open diamond [6], open circle [24], filled diamond [32]. The solid curve is a parameter fit to the recoil polarization results. Reproduced from Ref. [18].

The recoil polarization method was used for the first time in an experiment at the MIT-Bates Laboratory to measure the proton form factor ratio at Q^2 values of 0.38 and 0.5 GeV^2 [33]. A following experiment at MAMI using the same technique determined the ratio at Q^2 values of 0.373, 0.401 and 0.441 GeV^2 [34]. The results of both experiments were found to be in agreement with the Rosenbluth measurements. A significant discrepancy from the scaling behavior of the form factor ratio at Q^2 larger than 1 GeV^2 was observed by two Jefferson Lab Hall A [19, 30, 35, 36] and one Hall C experiments [31, 37]. These data exhibited a clear decrease of the ratio from unity to a value of about 0.35 at $Q^2 = 5.6\,\mathrm{GeV}^2$ (Fig. 1-6), indicating the electric form factor falls faster with increasing Q^2 than the magnetic form factor.

1.5 Two-Photon Exchange in Electron Scattering

The disagreement in the extracted form factor ratios using Rosenbluth method and polarization measurements is one of the most conspicuous puzzles in our knowledge of the *e-p* elastic scattering process. As pointed out in Ref. [38]:

> This discrepancy is a serious problem as it generates confusion and doubt about the whole methodology of lepton scattering experiments.

Recent investigations of this problem reveal that it could be attributed to the two-photon exchange (TPE) process [38]. In such a process, the nucleon undergoes a first virtual photon exchange which can lead to an intermediate excited state, and a second virtual photon exchange follows which brings the excited nucleon back to its ground state (Fig. 1-7). It was argued that the traditional treatment of radiative corrections in electron scattering experiment neglected the effect of the exchange of two hard photons between the electron and struck nucleon. This effect, deemed extremely small and well below one percent of the Born cross section by early estimates, cannot be reliably calculated in a model-independent manner, especially at large Q^2 values [39]. Hadronic-level calculations of the TPE contribution at low to moderate Q^2 values [40–42] showed that it can give rise to a strong angular-dependent corrections to the elastic

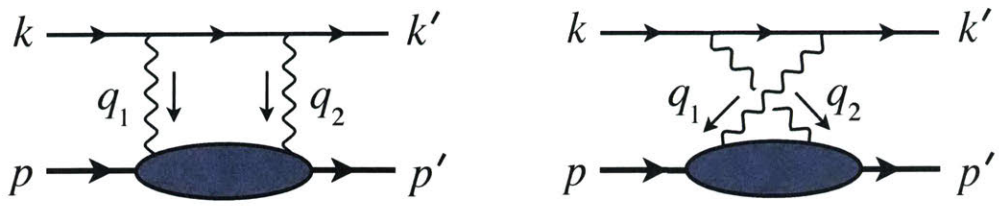

Figure 1-7: Box diagrams for the two-photon-exchange process in e-p elastic scattering. Reproduced from [39]

cross section, leading to large corrections to the slope (G_{Ep}^2) in Rosenbluth separation method. Calculations of the TPE amplitude in other theoretical frameworks also exist. Some groups used the dispersion relations to avoid the model dependence in the calculation arising from the off-shell intermediate state in the box diagrams [43]. The results are in good agreement with the hadronic evaluations with on-shell from factors at low Q^2 [44, 45]. TPE contributions at intermediate to high Q^2 are also calculated. They were carried out either in a partonic approach [46, 47] or in the framework of perturbative QCD [48, 49].

In parallel progress with the theoretical efforts to evaluate the TPE contribution, several experimental activities were launched to look for direct evidence of the TPE effect in e-p scattering process. These experiments measured the ratios of e^+p to e^-p cross sections at various kinematics; the connection to the TPE process is described below. The TPE contribution, $\delta_{2\gamma}$, arises from the interference between one- and two-photon exchange amplitudes.

$$\delta_{2\gamma} \equiv \frac{2\,\mathrm{Re}\left(\mathcal{M}_{1\gamma}^{\dagger}\mathcal{M}_{2\gamma}^{\mathrm{hard}}\right)}{|\mathcal{M}_{1\gamma}|^2}. \tag{1.34}$$

Here $\mathcal{M}_{1\gamma}$ is the Born scattering amplitude as defined in Eq. 1.21, and $\mathcal{M}_{2\gamma}^{\mathrm{hard}}$ is the contribution from the TPE processes in the box diagrams (Fig. 1-7) where both of the two photons have a sizable four-momentum. The $\delta_{2\gamma}$ term has opposite signs for electron and position scattering, while most of the other radiative corrections cancel to first order in the ratio. If we denote the charge-odd radiative corrections by δ_{odd}

and the charge-even terms by δ_{even}, we have

$$R^{\pm}_{\text{meas}} \equiv \frac{\sigma(e^+p)}{\sigma(e^-p)} \approx \frac{1+\delta_{\text{even}}-\delta_{\text{odd}}}{1+\delta_{\text{even}}+\delta_{\text{odd}}} \approx 1 - \frac{2\delta_{\text{odd}}}{1+\delta_{\text{even}}}. \tag{1.35}$$

The δ_{odd} term also includes the interference term between lepton and proton bremsstrahlung radiation, which is of comparable size to $\delta_{2\gamma}$. The deviation of the experimental ratio $R^{\pm}_{\text{meas}}$ from unity, after correcting for the contribution from the bremsstrahlung interference term, gives a measure of the TPE effect:

$$R_{2\gamma} = \frac{1-\delta_{2\gamma}}{1+\delta_{2\gamma}} \approx 1 - 2\delta_{2\gamma}. \tag{1.36}$$

Attempts to measure the e^-p/e^+p cross section ratio date back to 1960's and 1970's and no direct evidence for the significance of TPE process was found. Recent experimental efforts, aimed at understanding the role of TPE effects in e-p elastic scattering in view of the discrepancy of the Rosenbluth polarization-transfer discrepancy, were made at three different facilities. The VEPP-3 experiment took data with beam energies of 1.6 and 1.0 GeV using the storage ring at Novosibirsk, Russia and measured the ratios at both forward angles and backward angles [50]. The CLAS TPE experiment utilized an effective beam energy between 0.8 and 3.5 GeV and a nearly 4π acceptance spectrometer to cover Q^2 values from 0.85 to 1.45 GeV^2 and a wide ϵ range from 0.2 to 0.9 [51]. The OLYMPUS experiment ran on the DORIS positron/electron storage ring at the DESY laboratory, Hamburg, Germany with a nominal beam energy of 2.01 GeV and measured the ratio over a broad angular range between 25° and 75° [52]. The results of these experiments have much better precision than older data and, while they are generally consistent with a non-zero hard TPE contribution, the size of the measured effects appears smaller than theoretical predictions.

Direct measurements of electron/positron scattering cross section ratios are only currently practical at low Q^2 values due to the significant decline of elastic cross sections at large momentum transfer. In order to understand the TPE process at intermediate to high Q^2, one needs to combine precision cross section measurements

with theoretical TPE calculations. Such an attempt was made in Ref. [53], where the electromagnetic form factors were extracted from a combined analysis of the Rosenbluth cross section results and the polarization transfer data while incorporating the TPE contributions obtained by a hadronic model with nucleon elastic intermediate states [44]. The hadronic calculations were expected to be reliable for all ϵ values when the momentum transfer is small, which is the kinematic region of many high precision experiments. At higher Q^2 values, an empirical TPE correction which has a logarithmic dependence on Q^2 was applied. This global analysis brought the form factor ratio from unpolarized cross section measurements into decent agreement with the polarization transfer data (Fig. 1-8).

The role of the TPE process in electron scattering is still under active investigations. A generally accepted view today is that the TPE effect can at least partially explain the discrepancy between the form factor ratios extracted from the Rosenbluth and polarization measurements.

1.6 Theoretical Interpretations of Nucleon Form Factors

The accumulation of precise form factor data, along with the recent breakthrough in the polarization transfer measurements of form factor ratio, has generated plenty of theoretical studies of the electromagnetic structure of the nucleon. Most of the experimental data exist in the non-perturbative regime where a direct calculation from the underlying theory of QCD is almost impossible. In practice, various approximations have to be made to develop models for the form factor at low to intermediate Q^2. These models are either inspired by QCD with some simplifications, or are purely phenomenological and have free parameters to be tuned to describe the observed behavior of the form factors. At sufficiently large Q^2, the framework of perturbative QCD applies and can be used to make predictions about the form factors. However, it is still not conclusive at what Q^2 one starts to reach the pQCD domain as the onset

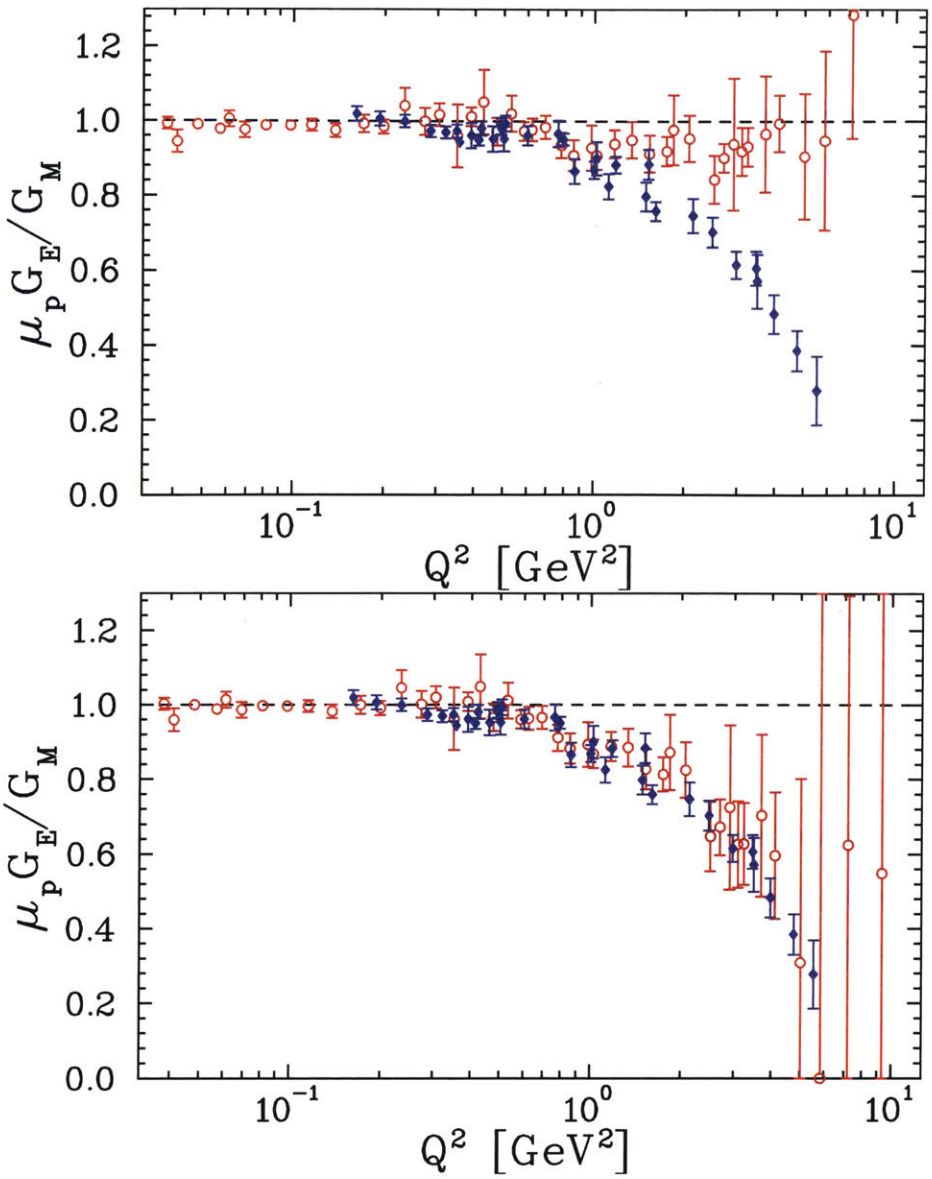

Figure 1-8: Ratio $\mu_p G_{Ep}/G_{Mp}$ extracted from polarization transfer (filled diamonds) and Rosenbluth measurements (open circles). The top (bottom) figure shows the Rosenbluth separation results without (with) TPE corrections applied to the cross sections. The TPE effects on the polarization transfer ratio are very small and well within the experimental uncertainties at large ϵ, where those measurements were typically performed [39, 53]. Reproduced from Ref. [53].

can only be predicted by a non-perturbative approach. Recently developed generalized parton distributions (GPDs) provide new insight into the structure of nucleons and potentially a unified view of the nucleon wave function in various nuclear reaction processes. In this section, a selection of the theoretical views of the nucleon form factors will be presented.

1.6.1 Vector Meson Dominance (VMD)

In the VMD model, the virtual photon couples to the nucleon via intermediate light vector mesons, such as $\rho(770)$, $\omega(782)$, and $\phi(1020)$ (Fig. 1-9). This is inspired by the fact that these vector mesons show up as prominent resonances at the corresponding center-of-mass energy values in $e^+e^- \rightarrow$ hadrons reactions. In such a model, the form factor for photon-nucleon coupling through a vector meson can be written as the meson propagator term times the meson-nucleon vertex form factors $F_{jV}(Q^2)$:

$$F_j^{is,iv}(Q^2) \sim \frac{1}{Q^2 + m_V^2} F_{jV}(Q^2), \tag{1.37}$$

where $j = 1,\ 2$ and the superscript is and iv denote the iso-scalar and iso-vector meson components respectively. The Dirac and Pauli form factors are linear combinations of F_{jV}^{is} and F_{jV}^{iv}:

$$F_{jp} = F_j^{is} + F_j^{iv}, \tag{1.38}$$

$$F_{jn} = F_j^{is} - F_j^{iv}, \tag{1.39}$$

$$\tag{1.40}$$

where the subscript p and n are for protons and neutrons respectively. The coupling strengths of the $\gamma - V$ vertex and the VNN vertex are either constrained by other data or fitted to the nucleon form factor measurement results.

The vector meson dominance has proven a reliable model for the nucleon form factors at relatively low momentum transfers [54], and can help understand the electromagnetic structure in this regime. For example, the approximate dipole behavior

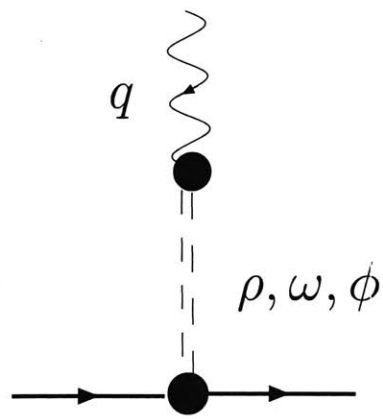

Figure 1-9: The vector meson dominance picture of the coupling of a photon to a proton.

can be understood as a consequence of the contributions of two nearby vector meson poles which have opposite residua [55]. In addition, an early VMD fit to existing data inferred a decreasing form factor ratio with Q^2 [54]. Different VMD models incorporate distinct mesons in the calculation. More recent VMD fits typically embody more heavier mesons, use analytical formulae to describe their finite widths, and impose the large-Q^2 behavior predicted by perturbative QCD [56]. Although the predictive power of such models is limited due to the tunable parameters, they have been quite successful in providing relatively good parameterizations of all nucleon electromagnetic form factors.

1.6.2 Perturbative QCD

One of the unique features of QCD is so-called asymptotic freedom, meaning that the strong force becomes relatively weak at short distances. This property licenses the use of Feynman calculus and perturbation method to solve QCD problems at very large Q^2. In the picture of pQCD, a photon of sufficiently high virtuality sees a nucleon as three massless collinear quarks. In order for the final state to contain an intact nucleon in the hard scattering process, the momentum transfer has to be divided among the three quarks through two hard gluon exchange, each carrying a fraction of the total four-momentum transfer. This is illustrated in Fig. 1-10. In this

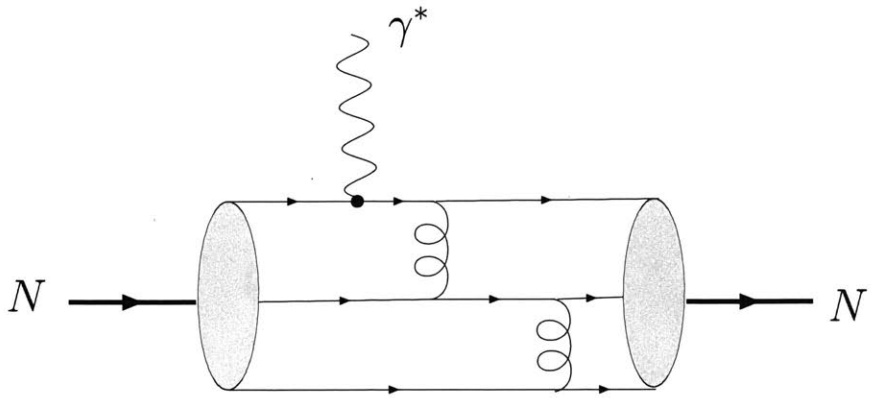

Figure 1-10: Perturbative QCD picture for the nucleon electromagnetic form factors.

scheme, the short distance, i.e., large Q^2, behavior of the Dirac form factor $F_1(Q^2)$ is dictated by the quark-gluon coupling and the gluon propagators. The quark-gluon couplings have a logarithmic dependence on Q^2, while each of the gluon propagator is inversely proportional to Q^2. Hence the following leading asymptotic behavior is expected [57]:

$$F_1(Q^2) \propto Q^{-4}. \tag{1.41}$$

On the other hand, the Pauli form factor $F_2(Q^2)$ involves a helicity flip at the quark level, which is suppressed in QCD at large momentum transfers. Contributions from F_2 can therefore only come at the next-to-leading order [57]:

$$F_2(Q^2) \propto F_1(Q^2)/Q^2. \tag{1.42}$$

In terms of the Sachs form factors G_{Ep} and G_{Mp}, the scaling prediction means the electromagnetic form factor ratio tends to be constant at sufficiently high Q^2.

The test for pQCD scaling predictions for the proton form factors is shown in Fig. 1-11. It appears that the F_{1p} data start to reach a plateau near $10\,\mathrm{GeV}^2$, and that is supported by the measurements up to $31\,\mathrm{GeV}^2$ [11]. However, the existing data for F_{2p} show no sign of the expected Q^{-6} behavior. Ref. [58] investigated the underlying assumption of collinearly moving quarks inside the proton, and showed that by including components in the nucleon light-cone wave functions with nonzero

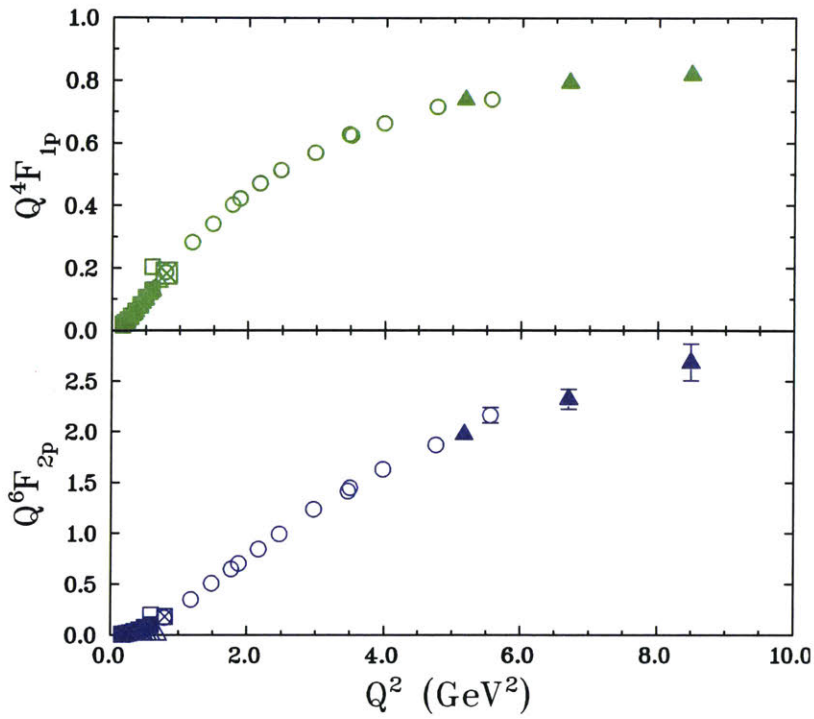

Figure 1-11: Test of the pQCD scaling behavior of proton form factors. The upper panel shows the proton Dirac form factor multiplied by Q^4, and the lower panel shows the Pauli form factor multiplied by Q^6. Data came from the Jefferson Lab $\mu_p G_{Ep}/G_{Mp}$ experiments using the Kelly parameterization for G_{Mp} [27]. Reproduced from Ref. [18].

quark orbital angular momentum projection, one can derive the following asymptotic scaling of the form factor ratio at the logarithmic accuracy:

$$\frac{F_2(Q^2)}{F_1(Q^2)} \sim \ln^2(Q^2/\Lambda^2)/Q^2, \tag{1.43}$$

where Λ denotes a non-perturbative mass scale. Such double-logarithmic enhancement has been proven to qualitatively agree with the polarization data of F_{2p}/F_{1p} [37]. Higher Q^2 data will continue to test this prediction in the future.

1.6.3 Connections to Generalized Parton Distributions (GPD)

The generalized parton distributions are introduced in Refs. [13, 14] to provide a framework to describe the amplitude for replacing a quark of one flavor and spin in the initial state of an nucleon by another quark to form the final state in hard exclusive reactions. They represent the non-perturbative matrix elements involved in the QCD factorization of hard exclusive processes such as deeply virtual Compton scattering (DVCS). The GPDs are functions of three variables: the quark longitudinal momentum fraction x, the momentum fraction asymmetry ξ, and the squared momentum transfer to the nucleon Q^2. It can be shown that they can be related to the quark flavor form factor $F_1^q(Q^2)$ and $F_2^q(Q^2)$ by the following sum rules:

$$\int_{-1}^{1} \mathrm{d}x\, H^q(x,\xi,Q^2) = F_1^q(Q^2), \tag{1.44}$$

$$\int_{-1}^{1} \mathrm{d}x\, E^q(x,\xi,Q^2) = F_2^q(Q^2), \tag{1.45}$$

where H^q and E^q are the vector and tensor GPDs respectively. Eqs. 1.44 and 1.45 hold for any ξ. These quark form factors can be related to the proton and neutron elastic form factors based on the $SU(2)$ isospin symmetry:

$$F_{ip} = \frac{2}{3}F_i^u - \frac{1}{3}F_i^d - \frac{1}{3}F_i^s, \tag{1.46}$$

$$F_{in} = -\frac{1}{3}F_i^u + \frac{2}{3}F_i^d - \frac{1}{3}F_i^s, \tag{1.47}$$

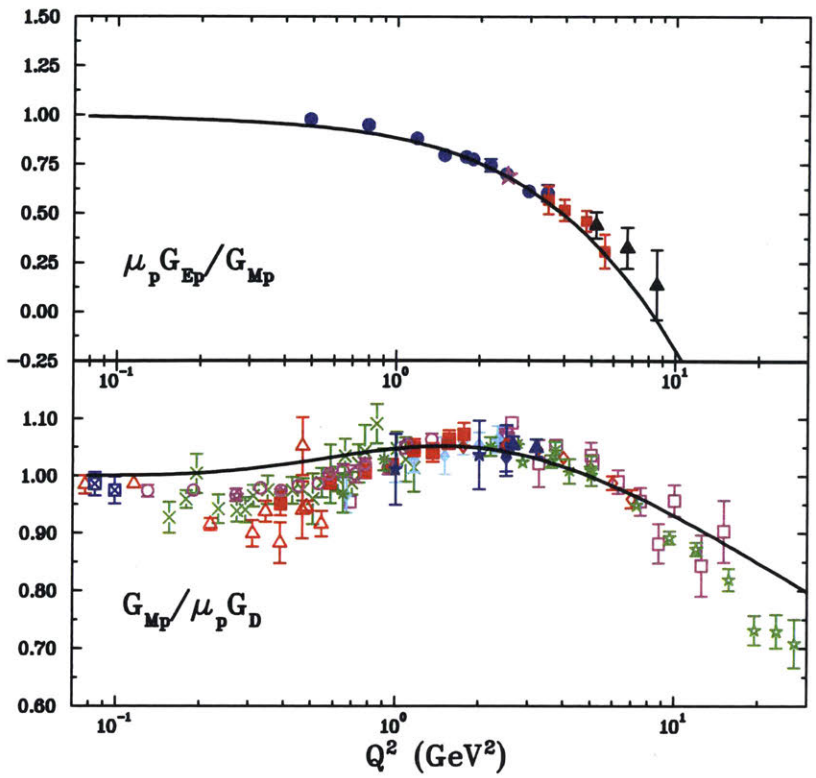

Figure 1-12: GPD calculation of the proton form factors. The upper panel shows $\mu_p G_{Ep}/G_{Mp}$ and G_{Mp} relative to the dipole form factor G_D. Reproduced from Ref. [18].

where $i = 1$, 2 and F_i^s is the strangeness form factor of the nucleon.

The relations described in Eqs. 1.44, 1.45, 1.46 and 1.47 allow one to predict the electromagnetic form factors with complete measurements or good models for the GPDs. Alternatively, the measured form factors at high Q^2, with the forward parton distributions accessible from deep inelastic scattering, provide stringent constraints on the behavior of the GPDs. Fig. 1-12 shows the proton and neutron Sachs form factors and a fit based on a modified Regge parameterization for the GPDs [59].

1.7 Summary

Elastic scattering of electrons off a nucleon is an effective experimental approach for studying various aspects of QCD. However, the non-perturbative nature of the strong interactions in the current accessible kinematic regime makes it impossible to develop

a universally applicable framework for this process. The nucleon form factors are introduced to describe the electron-proton scattering and to provide insight into the electromagnetic structure of the nucleon. Various models are proposed to explain or are fitted against existing experimental data of form factors, which are derived from either unpolarized scattering cross section measurements or experiments that measure polarization variables in the reaction.

While studies on the nucleon form factors have been very fruitful, there are still a few open issues and challenges in this field. Significant efforts have been made to understand the Rosenbluth/polarization discrepancy and to quantify the two-photon-exchange processes in electron scattering. This discrepancy has become increasingly striking at intermediate to high Q^2, where a direct measurement of TPE amplitude through e^-p/e^+p cross sections comparison becomes practically improbable. With more theoretical activities in this regime expected in the near future, precise experimental data in both unpolarized and polarized experiments are crucial for constraining and testing the various models.

High precision e-p scattering data are also necessary for answering other questions regarding the form factors at large Q^2. For example, it still remains unclear what Q^2 value marks the onset of the form factor scaling behavior. It is also intriguing to test the consistency of pQCD predictions with the observed data. In addition, the form factor data at high Q^2 will constrain the parameterizations of GPDs and yield information on the spatial distribution of partons which carry a large fraction of the nucleon momentum.

For the existing world data of proton form factors (Fig. 1-1), the majority of experiments were conducted at relatively low Q^2 values. The number of high Q^2 data is very limited and they have large statistical and systematic uncertainties. The recently upgraded electron accelerator facility at Jefferson Lab offered a great opportunity to perform a precise measurement of e-p elastic scattering cross sections up to a Q^2 of about $16\,\mathrm{GeV}^2$. These data not only serve as an independent check of the previous data in this Q^2 range, but they also greatly enrich the world cross section data with the first set of high Q^2 measurements at relatively small ϵ (large

scattering angles). The details of such an experiment are provided in the following chapters.

Chapter 2

Experimental Setup

2.1 Overview of the Experiment

Experiment E12-07-108 [60] performed high precision measurements of the elastic e-p scattering cross sections at $0.66 \leq Q^2 \leq 16.5\,\mathrm{GeV}^2$. It started taking data at Experimental Hall A of Thomas Jefferson National Accelerator Facility (TJNAF, also known as Jefferson Lab, or JLab) in the spring of 2015, and continued through the spring and fall of 2016. In the experiment, a high-energy electron beam was incident on a 15-cm-long unpolarized liquid hydrogen target. Scattered electrons were detected by a pair of the high resolution spectrometers (HRS). Each spectrometer consisted of an indexed dipole and three quadrupoles and could bend charged particles with a momentum up to $4\,\mathrm{GeV}/c$ by 45° in the vertical direction. Electrons were selected by a gas Cherenkov detector and a lead glass calorimeter in the detector hut.

Being one of the first two experiments performed at Lab after upgrading the continuous electron beam accelerator facility (CEBAF) to provide a beam with a maximum energy of 12 GeV, some of the important properties of Experiment E12-07-108 are summarized as follows:

- Long running period: The whole data collection process of E12-07-108 lasted for about two years. Several configuration changes were made to the system during this period. One of the most significant changes was the replacement of

the superconducting Q1 with a water-cooled iron magnet. These changes made the systematics of the final results vary from one running period to another.

- Parallel setup: Experiment E12-07-108 was scheduled to run parallel to E12-06-114, which measured the cross sections for the deeply virtual Compton scattering (DVCS) process with the left HRS detecting scattered electrons in coincidence with a high energy photon in a PbF_2 calorimeter [61]. When E12-06-114 took data, E12-07-108 could only utilize the right HRS. Due to potential radiation damage to the PbF_2 blocks, E12-06-114 limited the beam current to be less than 15 µA, which greatly limited the accumulated luminosity on target and increased the systematic uncertainty in the beam current measurement for kinematics taken with the parallel setup. In addition, the DVCS calorimeter was located between the beam line and the right HRS, making it impossible for the right HRS to sit at scattering angles less than 48°.

- Wide kinematic coverage: Experiment E12-07-108 performed measurements over a wide range of Q^2 and ϵ with beam energies ranging from 2.2 GeV up to 11 GeV, and spectrometer angles from 24.2° to about 53°. The dramatic changes in the electron energies and scattering angles translated into 6 orders of magnitude variation in the event rate.

A complete list of E12-07-108 kinematics can be found in Table 2.1.

2.2 Accelerator

The Jefferson Lab's state-of-the-art superconducting radio-frequency (RF) linear accelerators provide high energy continuous-wave electron beams for the study of nuclear structure and nuclear interactions in the QCD regime. In its 6-GeV configuration, a broad program of research was conducted to probe the structure of nucleons, study parity violation in electron scattering, test the standard model's completeness, explore the interactions of nucleons in the atomic nucleus, and search for excitation

Table 2.1: E12-07-108 kinematics

Kinematics	Q^2	E_{beam} (GeV)	θ_e (°)	ϵ	HRS	Run Period
K1-a†	1.66	2.1	48.8	0.62	R	Spring 2015
K1-b†	1.51	2.1	45.0	0.67	L	Spring 2015
K1-c†	1.10	2.1	35.0	0.79	L	Spring 2015
K1-d†	0.66	2.1	25.0	0.90	L	Spring 2015
K2-5	5.5	4.5	52.9	0.44	R	Spring 2016
K4-13(I)‡	12.7	8.8	48.8	0.35	R	Spring 2016
K5-17‡	16.5	11.0	48.8	0.30	R	Spring 2016
K4-12(I)	11.9	8.8	43.0	0.43	L	Spring 2016
K4-11	11.2	8.5	42.0	0.45	L	Fall 2016
K4-10	9.8	8.5	34.4	0.58	L	Fall 2016
K4-9*	9.0	8.5	30.9	0.65	L	Fall 2016
K3-6*	5.9	6.4	30.9	0.71	L	Fall 2016
K3-8	8.0	6.4	44.5	0.48	L	Fall 2016
K3-4	4.5	6.4	24.3	0.83	L	Fall 2016
K3-7*	7.0	6.4	37.0	0.60	L	Fall 2016
K4-12(II)	12.1	8.5	48.8	0.36	R	Fall 2016
K3-9*	9.0	6.4	55.9	0.33	R	Fall 2016
K4-13(II)$^{\ddagger *}$	12.6	8.5	53.5	0.30	R	Fall 2016
K5-16$^{\ddagger *}$	15.8	10.6	48.8	0.31	R	Fall 2016
K1-1	1.6	2.2	42.0	0.70	L	Fall 2016
K1-2*	1.86	2.2	48.8	0.62	R	Fall 2016

† The analysis details on these kinematics can be found in Ref. [62].

‡ Data for these kinematics were collected parallel to Experiment E12-06-114, where a low beam current was used to prevent radiation damage of their PbF_2 calorimeter. See text for details.

* This thesis will focus on the analysis of these kinematics.

states of nucleons. A general review of the scientific programs carried out at Jefferson Lab in the 6 GeV era can be found in Ref. [63].

An energy upgrade to the CEBAF was completed in 2017 [64]. The schematic for the upgraded CEBAF accelerator is shown in Fig. 2-1. Electrons are emitted through a thermionic cathode or a polarized laser cathode and accelerated by two anti-parallel superconducting linacs. The linacs are connected by a total number of 9 magnetic transport arcs which steer the electrons through the "racetrack" up to five times to reach the final energy of 6 GeV. In its 6 GeV configuration, each linac consisted of 20 cryomodules and could boost the electron energy by 600 MeV per pass. During the 12 GeV upgrade, 5 accelerating cryomodules with four times higher gradients per unit length were added to each linac to reach a maximum energy of nearly 11 GeV at the three experimental halls A, B and C. In addition, an added arc and beam line to the accelerator allows electrons to recirculate an extra pass through the north linac and be sent to the newly constructed Hall D, which utilizes a 12 GeV electron beam to generate a 9 GeV tagged photon beam for the study of meson spectroscopy.

The linacs can generate a 1497 MHz continuous wave electron beam, which is composed of four 249.5 or 499 MHz interleaved beams. The RF deflecting cavities operate at 499 MHz near the end of the south linac and are used to extract electrons from the machine with different combinations of current and energy and direct them toward the experimental halls A, B and C. An additional 750 MHz RF separator splits the 5th pass beam for Hall D [65]. The upgraded CEBAF is also capable of providing beams with large dynamic range in the currents. A 100 μA beam can be delivered to one or both of the Halls A and C while Hall B and D receive extremely low currents, on the order of nano amperes.

2.3 Hall A

The Experimental Hall A is the largest one among the four end stations at TJNAF with a diameter of 53 m. The core of the Hall A equipment is a pair of 4 GeV/c high resolution spectrometers (HRSs) which bend incoming charged particles by 45°

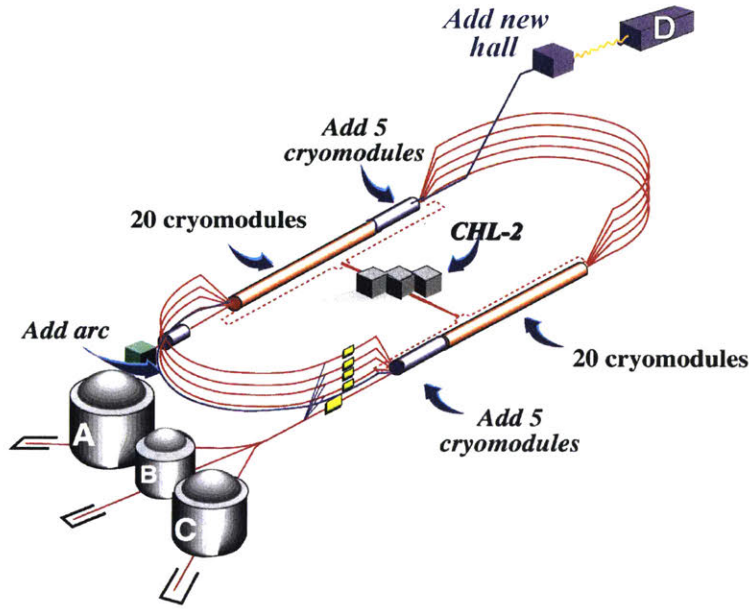

Figure 2-1: The CEBAF accelerator at Jefferson Lab, with the modifications to the facility to realize the 12 GeV upgrade illustrated.

in the vertical direction. The configuration of Hall A during E12-07-108 is illustrated in Fig. 2-2. Other key elements, including the beam line and the cryogenic target in the scattering chamber, are also shown.

2.4 Beam Line

The instrumentation along the beam line consists of various elements necessary to transport the electron beam onto the target and into the dump, and to measure simultaneously the relevant properties of the beam. In the data taking process of E12-07-108, special attention was paid to the control and determination of the beam energy, current, and the position and size of the beam at the target location.

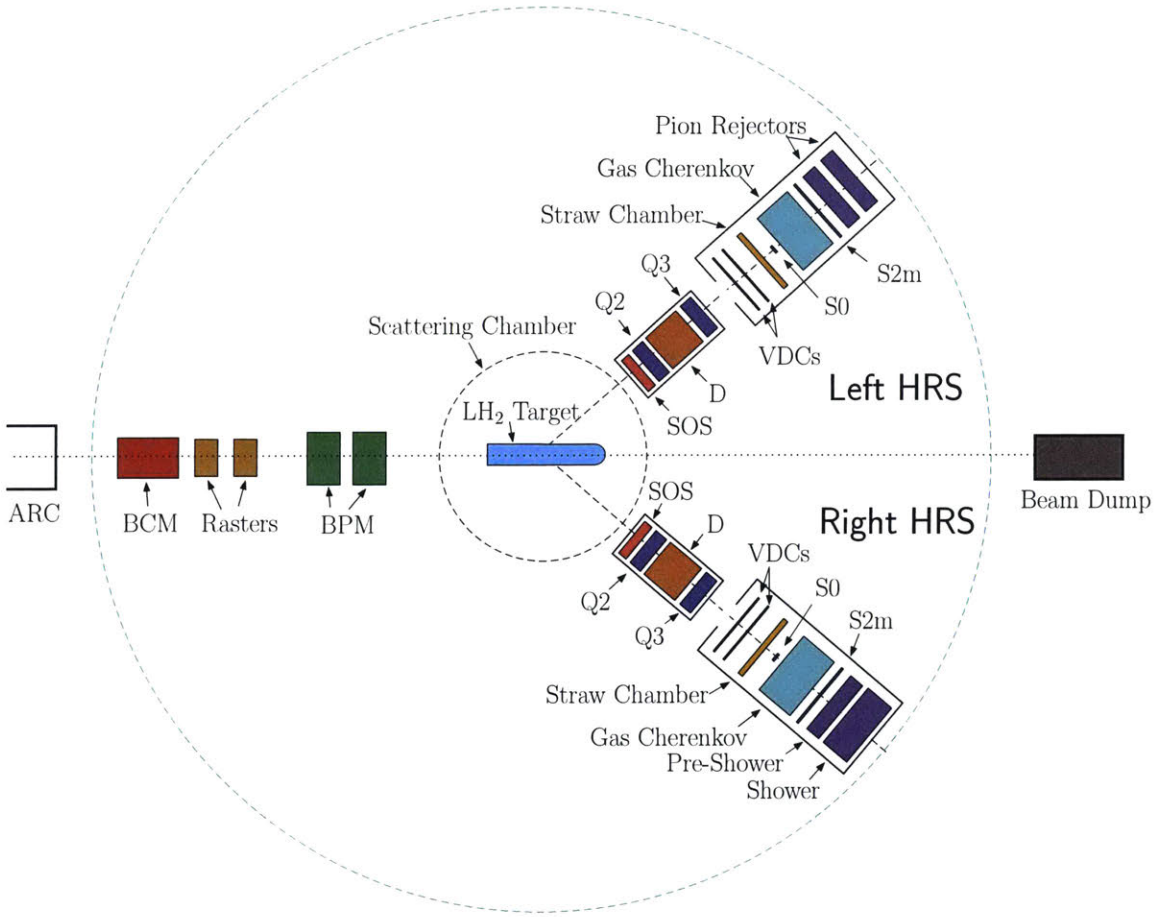

Figure 2-2: Hall A configuration during E12-07-108.

2.4.1 Beam Energy Measurement

Precise measurements of the beam energy are required in order to extract physics information from the measured e-p elastic cross section. Three methods were used to determine the absolute energy of incident beam during experiment E12-07-108.

- The Arc method determines the energy by measuring the deflection of the beam in the arc section of the beam line. The nominal bend angle of the beam in the arc section is $\theta = \pi - \phi = 37.5°$, where ϕ is indicated in Fig. 2-3. In leading order, the magnitude of the momentum of incident electrons can be calculated by

$$p = k\frac{\int \mathbf{B} \cdot \mathrm{d}\boldsymbol{l}}{\theta}, \tag{2.1}$$

  where $k = 0.299792$ GeV rad Tesla^{-1} m$^{-1}/c$, and $\int \mathbf{B} \cdot \mathrm{d}\boldsymbol{l}$ represents the integral of transverse magnetic field along the trajectory of the beam and is usually referred to as the $\mathrm{B} \cdot \mathrm{d}l$ value of the arc section. The Arc method consists of two simultaneous measurements, one for the magnetic field integral of the bending elements (eight dipoles in the arc), based on a reference magnet (9th dipole) measurement, and the actual bend angle of the arc, based on a set of wire scanners or harps. A detailed description of the instrumentation for the arc energy measurement can be found in Ref. [66].

  The measurement can be made when beam is tuned in either dispersive or achromatic mode in the arc section. The dispersive mode was preferred by E12-07-108 since it minimizes orbit corrections and provides a precision that is about two times better than the achromatic mode does. However, to establish dispersive optics requires all steering magnets except dipoles be turned off and hence can not be performed during production data taking. During E12-07-108, at least one dispersive measurement was carried out at each available pass, and the results are given in Table 2.2.

- The energy of the incident electrons was also monitored by the "Tiefenbach" measurements during data collection. This approach used the current values of

Table 2.2: Summary of beam energy settings during E12-07-108 in the fall of 2016 measured by the Tiefenbach value and the Arc method (with the beam in dispersive tuning). The numbers in the parentheses are the uncertainties in the last significant digit.

Number of passes	Tiefenbach value (GeV)	Arc measurement (GeV)
1	2.218(2)	2.222(1)
3	6.407(6)	6.427(3)
4	8.497(8)	8.520(4)
5	10.589(10)	10.587(5)

$\int \mathbf{B} \cdot d\boldsymbol{l}$ of Hall A arc and incorporated a correction factor based on the reading of the beam position monitors in the Hall A arc. This number was continuously recorded in the data stream for each run. As a non-invasive approach to beam energy measurement, it had been used in the analysis of many 6 GeV experiments carried out at Hall A and its uncertainty had been found to be $\delta E/E \approx 5 \times 10^{-4}$ for beam energies lower than 6 GeV. However, the correction factor has not been well tested at higher incident energies. Thus it is not the primary value for beam energy used in E12-07-108 analysis. Instead, the Arc measurement results at dispersive beam tune were used to extract reduced cross sections.

2.4.2 Beam Current Monitor

A beam Current Monitor (BCM) is located along the beam line of Hall A near the arc section, which provides a stable, low-noise, non-interfering measurement of the beam current [67]. It consists of an Unser monitor, two RF cavities, associated electronics, and a data-acquisition system. The cavities and the Unser monitor are located 25 m upstream of the target and enclosed in a temperature-stabilized box to improve magnetic shielding. The schematic diagram of the BCM system is illustrated in Fig. 2-4.

The Unser monitor is a parametric current transformer designed for non-destructive

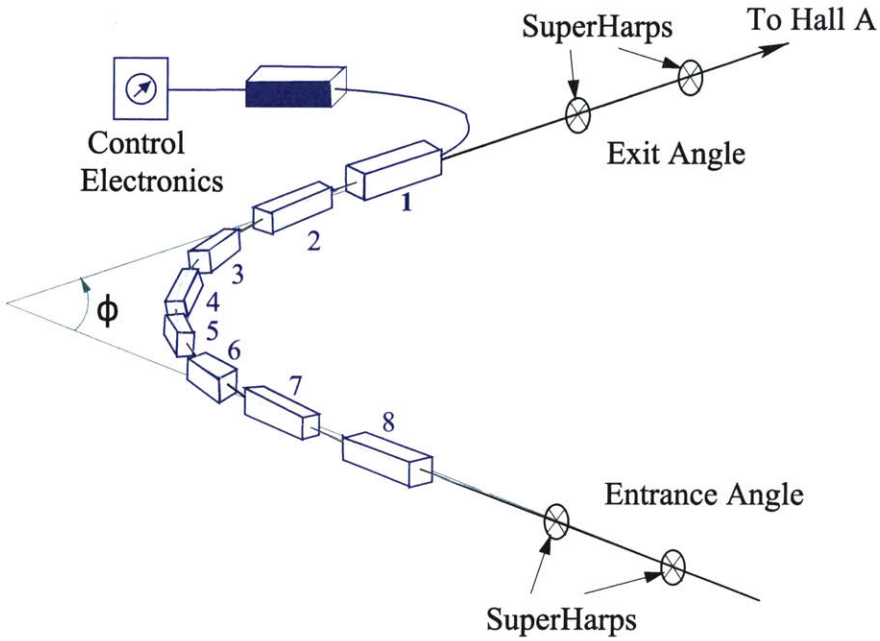

Figure 2-3: Schematic of the Arc energy measurement.

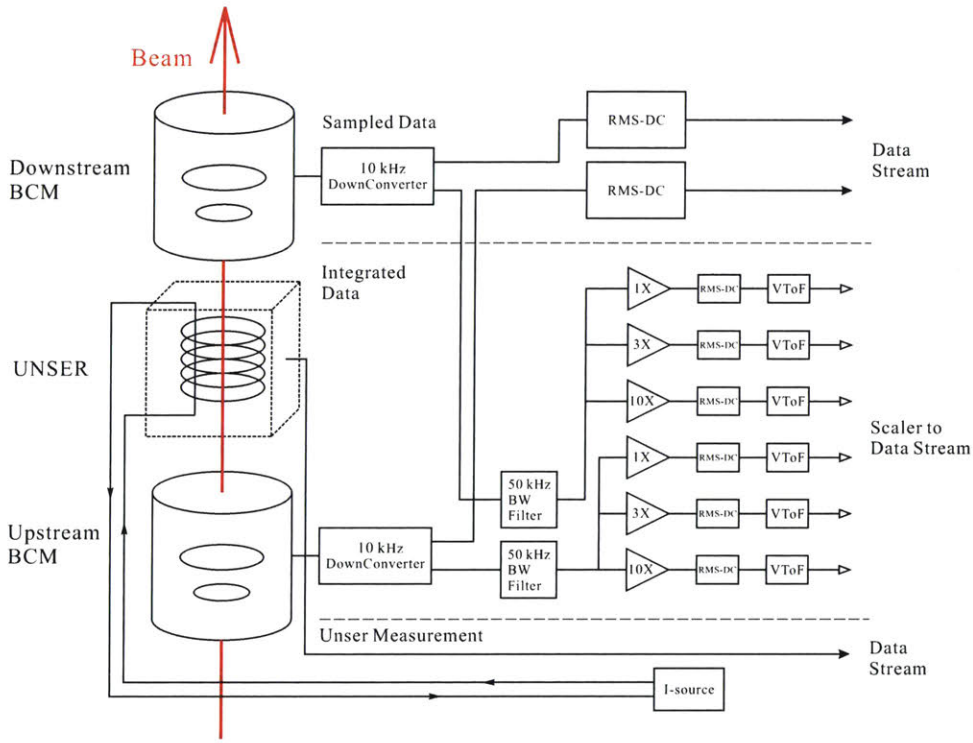

Figure 2-4: Schematic of the Hall A beam current measurement system.

beam current measurement and provides an absolute reference [68]. The monitor is calibrated by passing a known current through a wire inside the beam pipe and has a nominal output of 4 mV/µA. As the Unser monitor's output signal drifts significantly on a time scale of several minutes, it cannot be used to continuously monitor the beam current. However, this drift is measured during calibration runs by taking a zero current reading and the net measured value is used to calibrate the two RF cavities. The more stable cavities are then used to determine the beam current and integrated charge for the production runs in E12-07-108.

The two resonant RF cavity monitors on either side of the Unser monitor are stainless steel cylindrical high-Q ($\sim$ 3000) waveguides which are tuned to the frequency of the beam (1.497 GHz), resulting in voltage levels at their outputs which are proportional to the beam current. Each of the RF output signals from the two cavities is split into two parts (to be sampled or integrated).

The sampled data are processed by a high-precision digital AC voltmeter (HP3458A), which provides a digital output once every second representing the RMS (root-mean-square) average of the input signal during that second. The resulting number is proportional to the beam charge accumulated in the corresponding second. The signals to be integrated are sent to an RMS-to-DC converter, which produces an analog DC voltage level. This level drives a Voltage-To-Frequency (VTOF) converter whose output frequency is proportional to the input DC voltage level. These signals are then fed to Fastbus scalers and are finally injected into the data stream along with the other scaler information. These scalers simply accumulate during the run, resulting in a number which is proportional to the time-integrated voltage level, and therefore more accurately represents the total integrated beam charge. The regular RMS to DC output is linear for currents from about 5 µA to somewhere well above 200 µA. A set of amplifiers with gains of $\times 3$ and $\times 10$ has been introduced to allow the non-linear region to be extended to lower currents at the expense of saturation at high currents. Hence, there is a set of three signals coming from each BCM (u1, u3, u10, d1, d3, d10). These 6 signals are fed to scaler inputs of each spectrometer, providing redundant information for determining the charge during a run. During E12-07-108,

the amplifiers for the upstream BCM did not work, so only four BCM scalers (u1, d1, d3, and d10) in each spectrometer were used for beam current measurement. The precision in the determined incident charge is discussed in Sec. 3.9.

2.4.3 Raster and Beam Position Monitor

The position and direction of the beam at the target location is determined by two Beam Position Monitors (BPMs) located at 7.345 m and 2.214 m upstream of the target. They determine the relative position of the beam to within 100 µm for currents above 1 µA [69, 70]. The absolute position of the beam is determined from the BPMs by calibrating them with respect to wire scanners (superharps) which are located adjacent to each of the BPMs. The position information from the BPMs is recorded in the raw data stream event-by-event. The beam position and direction at the target are linearly extrapolated using the beam positions at the two BPMs calculated from the 8 BPM antennas (2×4).

The E12-07-108 experiment used a 15 cm liquid hydrogen target. The narrow CEBAF beam could overheat the cell of the cryogenic target and cause local damage and significant boiling. To minimize the local boiling effect, the beam was rastered by two pairs of horizontal and vertical steering dipoles which were located 23 m upstream of the target and deflected the beam at 25 kHz. The two horizontal dipoles were synchronized, as was the vertical pair. The average size of the rastered beam was proportional to the current in the raster magnets, which was recorded by analog-to-digital converters for each event. During the E12-07-108 experiment, the rastered beam homogeneously covered a square shape with a typical size of around 2 mm × 2 mm. More technical details about the raster in Hall A can be found in Ref. [71] and the references therein.

2.5 Target

The cryogenic target system was mounted on a target ladder inside the scattering vacuum chamber along with sub-systems for cooling, gas handling, temperature and

Table 2.3: Target configuration of the E12-07-108 experiment.

Target name	Target material
Loop 1	4 cm helium
Loop 2	15 cm hydrogen
Loop 3	15 cm hydrogen
4 cm dummy	Aluminum 3003
15 cm dummy	Aluminum 7075
Optics	Carbon graphite
Empty 1	N.A.
Empty 2	N.A.
Thick aluminum	Aluminum 7075
Carbon hole	Carbon graphite
BeO	BeO
Carbon	Carbon graphite
Raster target	Aluminum 7075/hole

pressure monitoring, and target control and motion. Also mounted on the ladder was a set of solid targets, such as a 15 cm empty dummy target for background measurement, and a multi-foil carbon target for calibration of spectrometer optics. The desired target could be selected from the counting house by moving the ladder vertically up and down until the target was aligned with the beam. A complete list of the targets used in Experiment E12-07-108 can be found in Table 2.3.

The basic cryogenic target had three independent target loops, each of which had an aluminum cylindrical cell with a hemispherical tip. They differed in the geometrical size and all could be used for the liquid hydrogen (LH_2) target. Loop 1 had a length of 4 cm and was not used in the experiment. Loops 2 and 3 were both 15 cm in length. Loop 2 had a diameter of 1.5 inches while loop 3 was a bit smaller, with a diameter of 1.315 inches. Loop 3 also featured an improved flow design which reduced the density fluctuation at high beam current and was the preferred production target. It was used for production data taking in spring 2016. However, there was a leak in this loop in the fall of 2016 and loop 2 was used in this period instead. More details about the configuration of the target ladder during the E12-07-108 experiment can be found in Ref. [72].

The cryotarget was cooled with liquid helium at 15 K supplied by the End Station Refrigerator (ESR). During the E12-07-108 experiment, the LH_2 target was operated at 19 K with a pressure of 0.172 MPa (Pa is short for Pascal, the unit of pressure specified by the International System of Units (SI)), and the nominal density was 0.0723 g/cm^3. The temperatures were stabilized by automatically controlling Joule-Thompson (JT) valves (one for each loop) to adjust the supply of coolant with a proportional, integral, derivative (PID) feedback loop. Three thermometers were used to measure the target temperature, two of which were located near the entrance and the exit of the loop, respectively. The fluctuation in the measured temperature was found to be 0.05 K, which amounted to less than 0.1% variation in the average density of liquid hydrogen [73].

2.6 Hall A Spectrometers

2.6.1 Overview

The core of the Hall A equipment is a pair of identical 4 GeV/c High Resolution Spectrometers (HRS), which are designed for detailed investigations of the structure of nuclei. The HRSs provide a momentum resolution of better than 2×10^{-4} and a horizontal angular resolution of better than 2 mrad at a designed maximum central momentum of 4 GeV/c. The HRS bends an incoming charged particle by 45° in the vertical direction and its original design included a pair of superconducting $\cos(2\theta)$ quadrupoles (Q1 and Q2) followed by a 6.6 m long dipole magnet with focussing entrance and exit polefaces. Following the dipole is a third superconducting $\cos(2\theta)$ quadrupole (Q3). The first quadrupole Q1 is convergent in the dispersive (vertical) plane. Q2 and Q3 are identical and both provide transverse focussing. Both spectrometers can provide a momentum resolution better than 2×10^{-4} in a momentum range of 9% acceptance. The main design characteristics of the Hall A HRS can be found in Table 2.4.

Table 2.4: The main characteristics of the Hall A high resolution spectrometers. The resolution values are for the FWHM. The central solid angle corresponds to the target center and for charged particles with the central HRS momentum p_0. The transverse length and position are along the horizontal line perpendicular to the central ray of the HRS and passing the target center.

Configuration	QQD_nQ vertical bend
Bending angle	45°
Optical length	24.2 m
Momentum range	0.3–4.0 GeV/c
Momentum acceptance	$-4.5\% < \delta p/p < +4.5\%$
Momentum resolution	2×10^{-4}
Angular acceptance (horizontal)	±30 mrad
Angular acceptance (vertical)	±60 mrad
Angular resolution (horizontal)	0.5 mrad
Angular resolution (vertical)	1.0 mrad
Central solid angle	6 msr
Transverse length acceptance	±5 cm
Transverse position resolution	1.0 mm

2.6.2 Magnet Configurations in Experiment E12-07-108

In the preparation of the E12-07-108 experiment in 2015, a rapid, non-linear voltage increase across the two leads of the superconducting Q1 on the right HRS was observed with an increase in current, which rendered the magnet unstable for future experiments. This Q1 was then replaced by a quad from the Short Orbit Spectrometer (SOS) [74] (referred to as SOS-red below) in Hall C of Jefferson Lab. The SOS quad had a radius of 12.5 cm, which was a bit smaller than the 15 cm radius of the original Q1. The electric current in the SOS quad was fine-tuned such that the forward transport matrix of the new HRS was as close as possible to the design in the 6 GeV era.

The Q1 magnet on the left HRS was later found to exhibit a symptom similar to that of the right Q1 and was removed in the summer of 2016. A brand new iron quadrupole (referred to as SOS-blue below), which had a design identical to that of the red SOS quad, was delivered to JLab to be used for data taking in the fall of 2016. This new quad was mounted on the right HRS (Fig. 2-5), and the SOS-red

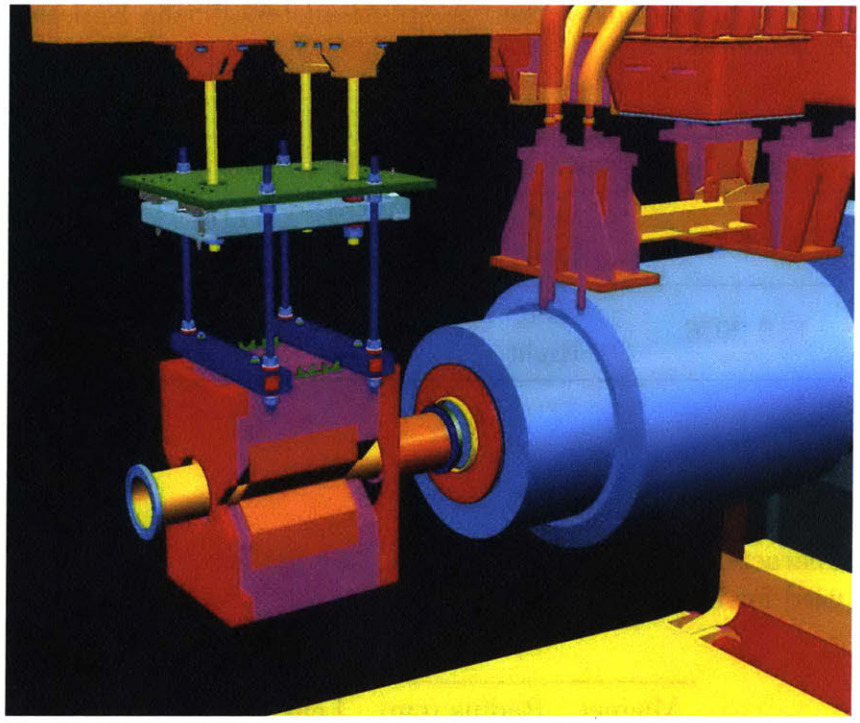

Figure 2-5: Schematic for mounting the SOS quad on HRS

was moved to the left HRS. The configurations of the magnets in the two HRSs during Experiment E12-07-108 are summarized in Table 2.5. Both the SOS quads and the original Q1 have a barrel shape, with the SOS quads having smaller radii and lengths. The comparison between the geometries of the two SOS quads and the superconducting Q1 can be found in Table 2.6. The relationship between the magnetic field in the SOS quad and its driving current was carefully studied during the commissioning process [75]. The calibration of HRS optics reconstruction after the replacement of superconducting Q1 is discussed in Sec. 3.4.

2.6.3 The Detector Package

The detectors and all of the data-acquisition (DAQ) electronics are located inside a detector hut to shield them from radiation background. The detector packages were designed to perform various functions in the characterization of charged particles passing through the spectrometer. These included: providing a trigger to activate the data-acquisition electronics, collecting tracking information (position and direction),

Table 2.5: The configurations of the two spectrometers during Experiment E12-07-108.

Run period	Spectrometer	The first quadrupole in HRS
Spring 2016	Left Right	Q1 SOS-red
Fall 2016	Left Right	SOS-red SOS-blue

Table 2.6: Characteristics of the superconducting Q1 (used in 6 GeV era) and the SOS quad (used for Experiments E12-07-108 and E12-06-114).

Magnet	Radius (cm)	Length (cm)
Q1	15	94
SOS	12.7	70

precise timing for time-of-flight measurements and coincidence determination, and identification of the scattered particles.

The configurations of the detectors on the left and right spectrometer for Experiment E12-07-108 are shown in Fig. 2-6. Two scintillator planes S0 and S2m were used to provide trigger signals and timing information. The particle identification was obtained from the gas-Cherenkov detector and two layers of lead-glass shower counters. A pair of vertical drift chambers (VDC) provided tracking information. A straw chamber was installed between the VDC and other detectors to study the reconstruction efficiency of the VDCs with the standard tracking algorithm. The main parts of the detector package in the two spectrometers (trigger scintillators and VDCs) were identical. The arrangements of particle-identification detectors differed slightly.

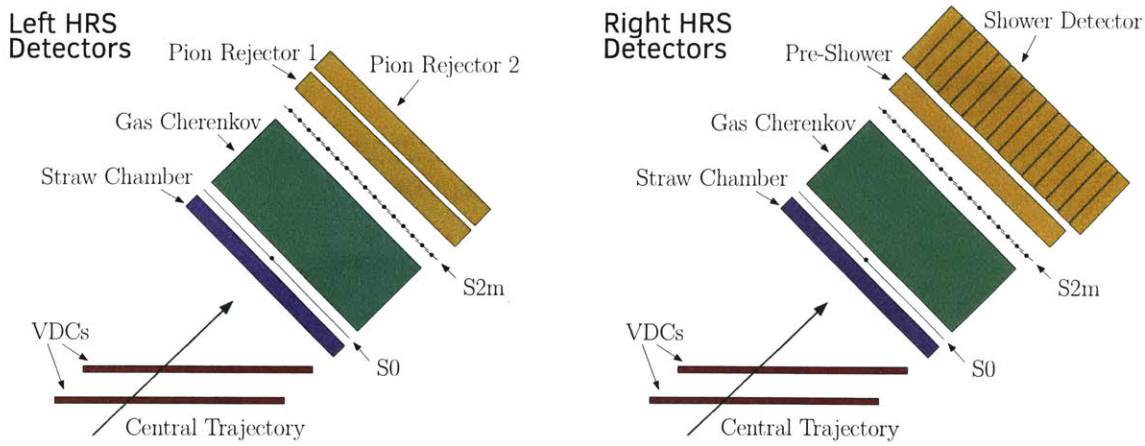

Figure 2-6: Configuration of left and right HRS detectors during E12-07-108 (side view).

Vertical Drift Chambers

Each spectrometer had a pair of identical VDCs [76] to provide a precise measurement of the incident positions and angles of charged particles at the spectrometer focal planes. The tracking information from the VDC measurement was combined with the knowledge of the spectrometer optics to reconstruct the position, angle, and momentum of the particles at the scattering vertex.

The top VDC was placed 33.5 cm above the bottom VDC and shifted by another 33.5 cm in the dispersive direction to fit the 45° central particle trajectory (Fig. 2-7). Each VDC contained two planes of wires in a standard UV configuration—the wires of each successive plane were oriented at 90° to one another, and lay in the laboratory horizontal plane. There were 368 sense wires in total in each plane, spaced 4.24 mm apart.

The electronics of the VDC read-out system was upgraded in the fall of 2014 [62], including the replacement of preamp/discriminator cards [76] by the new MAD cards developed by JLab's Electronics Group and installation of the level translators and their power supplies. The new MAD cards reduced the operational voltage of the VDC's cathode plane from -4 kV to -3.5 kV, which not only made the long term operation more stable and slowed down the aging of the sense wires, but also minimized the influence of the space charge effect [77, 78]. The VDCs were supplied

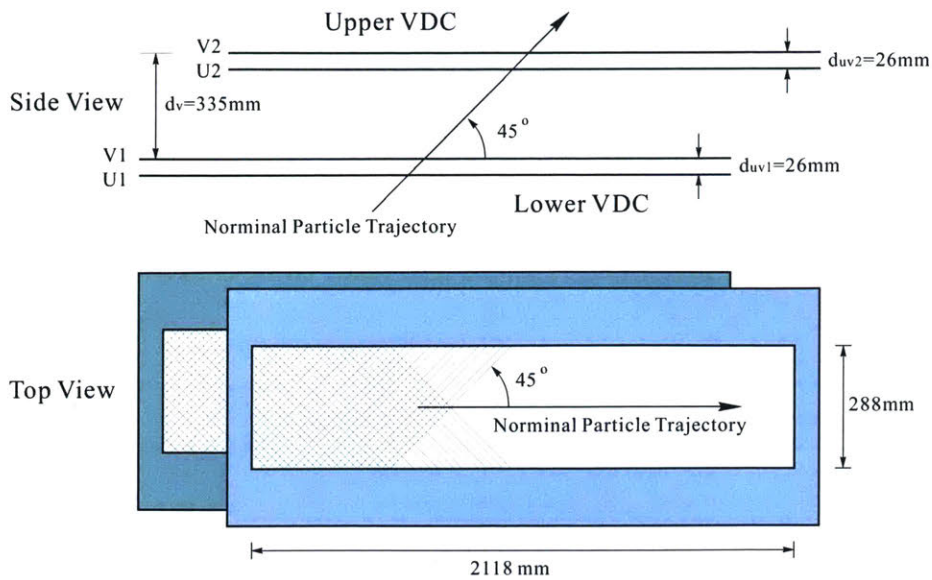

Figure 2-7: Schematic layout of a pair of VDCs in the HRS (not to scale). The U and V sense wires are orthogonal to each other and lie in the horizontal plane of the laboratory. They are inclined at an angle of 45° with respect to both the dispersive and non-dispersive directions. The lower VDC coincides (essentially) with the spectrometer focal plane.

with a 62%/38% argon-ethane (C_2H_6) mixture, with a flow rate of 10 L/hour [67]. The nominal trajectory angle for the HRS in the spectrometer mid-plane was 45°, which corresponded to an angle of 55° in the plane perpendicular to the sense wires. When a charged particle traveled through the chamber, it ionized the gas inside the chamber and left behind a track of electrons and ions along its trajectory. The ionization electrons accelerated towards the wires at a velocity of about 50 µm/ns and fired an average of five sense wires as shown in Fig. 2-8. The fired wires were read out with Time-to-Digital converters (TDC) operating in common stop mode. In this configuration, a smaller TDC signal corresponded to a larger drift time. The drift time information was then used to reconstruct the distances of the track to each fired wires. The cross-over point where the track passed through the sense wire plane was determined by a linear fit to the drift distances. The per-plane FWHM position resolution for the VDCs was about 225 µm [76]. The typical wire efficiency during Experiment E12-07-108 was higher than 99.9%.

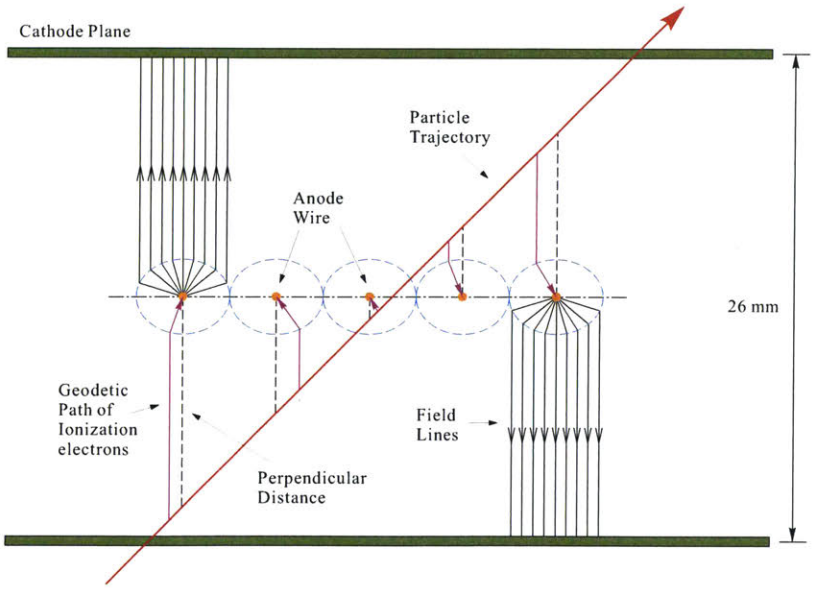

Figure 2-8: A typical track passing through one VDC. The field lines in the VDC, anode wires, cathode plane and the drift paths of the ionization electrons are also shown.

Straw Chamber

A straw chamber (SC) was installed between the VDC and the S0 scintillator (see below) to provide tracking information for multi-cluster events in the VDCs. It had been originally the front chamber of the Focal Plane Polarimeter (FPP) [79] that was used to measure the polarization of protons in polarization transfer experiments [80]. The SC was oriented perpendicular to the nominal central ray of HRS and located about 1.5 m away from the center of the bottom VDC. The active area of the SC was about 209 cm (dispersive) $\times$ 60 cm (non-dispersive) and contained 6 planes of straw tubes of radius 0.5 cm, where they were oriented along the U and V directions at 45° and 135° relative to the spectrometer dispersive direction (Fig. 2-10). The three U planes were located about 7 cm farther from the VDCs than the three V planes. A thin wire ran along the central axis of each tube as shown in Fig. 2-9, and was held at positive high voltage ($\sim$ 1.8 kV) relative to the straw. Each tube was supplied with a gas mixture of argon (62%) and ethane (38%). When a charged particle passed through the straw, it ionized the argon gas atoms, and the produced electrons drifted towards the anode wire, at a constant velocity of about 50 µm/s. When the electrons

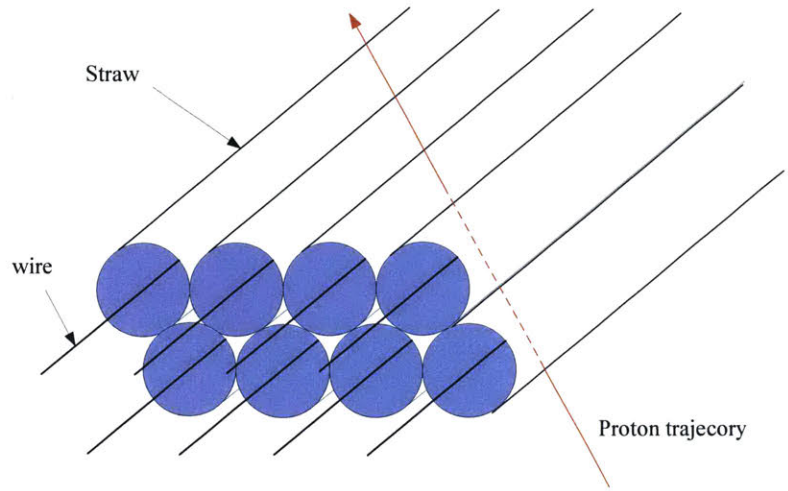

Figure 2-9: Structure of a straw chamber (only two out of three straw planes are shown here).

got within about 100 µm of the wire, the increase in electric field strength was large enough so that additional atoms ionized, leading to an avalanche effect and producing a gain of about 10^5 per primary ionization. The movement of the positive ions and negative electrons induced a voltage drop on the wire and produced a negative analog signal. This signal was then sent to a read-out board, where it was pre-amplified and discriminated to form a logic pulse.

More details of the configurations of the FPP front chambers can be found in Ref. [81]. Modifications to the high voltage and gas distribution systems of straw chamber to fit the need of Experiment E12-07-108 is discussed in Ref. [62].

Scintillator Planes

There were two planes of scintillators (S0 and S2m) in each HRS, separated by a distance of about 1.6 m, providing trigger and timing information. The S0 scintillator was a single-long scintillator paddle attached to the frame of the Gas-Cherenkov detector and viewed by two 3" photo-multiplier tubes (PMTs), one at each end to collect the photons produced by particles passing through the scintillator. The active area of S0 was about 0.25 m along the non-dispersive direction and 1.7 m along the dispersive direction. The S2m plane consisted of 16 fast-scintillator paddles,

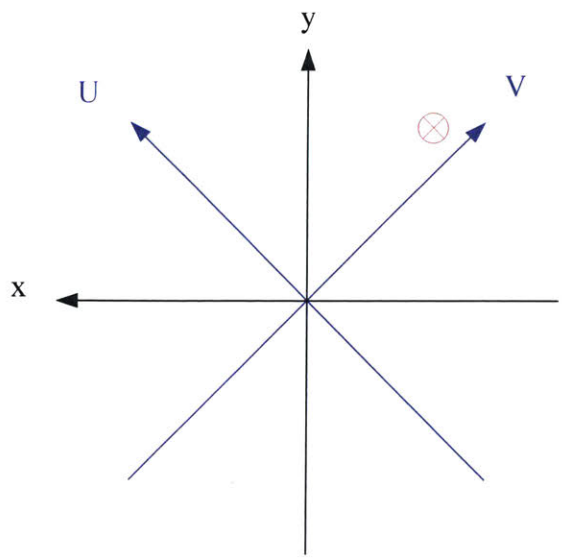

Figure 2-10: The orientation of straw chamber coordinate system in the HRS transport coordinate system.

each with a dimension of 43.2 cm (length) × 14 cm (width) × 5.08 cm (thickness) (Fig. 2-11), and to either end of each paddle was attached a 1" PMT to convert the generated photons to electric pulse. The analog signals generated in the PMTs were discriminated and sent to a LeCroy 1877 [82] multi-hit TDC module with a timing resolution of 0.5 ns/channel. Both S0 and S2m were perpendicular to the nominal central ray at the focal plane.

The coincidence signal between the two scintillator detectors was used as the main trigger for Experiment E12-07-108. In addition, the hodoscope setup could be used to measure the time-of-flight between the two scintillators. The distance between S0 and S2m was too short to make the timing information useful for identifying electrons from hadrons. However, it was an effective approach to separating the scattering events from the cosmic background (see Sec. 3.3.3).

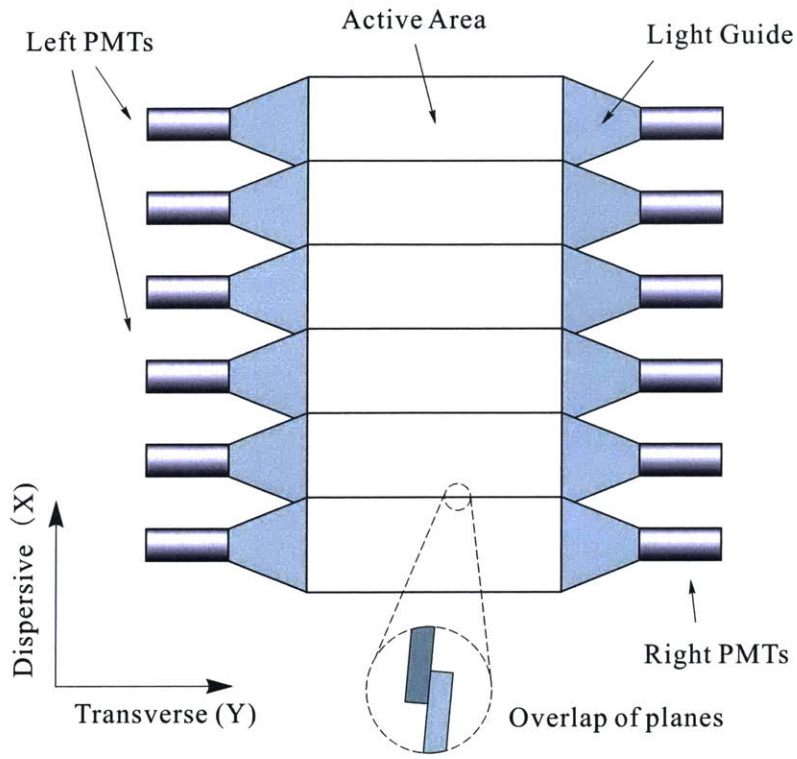

Figure 2-11: Layout of the S2m counter. Only 6 out of the 16 paddles are shown here.

Gas Cherenkov Detector

The Gas Cherenkov (GC) counter [83] was a threshold Cherenkov detector based on the Cherenkov effect [84, 85] and was one of the main particle identification detectors in Experiment E12-07-108. It was filled with CO_2 at atmospheric pressure and was mounted between the trigger scintillator planes S0 and S2m. The index of refraction is 1.00041 at sodium D line, which corresponded to a threshold for producing Cherenkov radiation at momenta of 0.017 GeV/c for electrons and 4.8 GeV/c for pions. Given that the momentum range of HRS is from 0.3 to 4.0 GeV/c, detection of Cherenkov radiation could thus be used either as a tag for electrons, or as a veto for the identification of the heavier hadron component. The fast information could also be used for online trigger purposes.

The length of the particle path in the gas radiator was 130 cm in the right HRS, and 120 cm in the left HRS. The detector had ten spherical mirrors with 80 cm focal length positioned in a 2 (horizontal) $\times$ 5 (vertical) array to collect Cherenkov light. The mirrors were specially built to be light weight, resulting in a very small total thickness (0.23 g/cm^2) [86] traversed by the particles. Each mirror had a radius of curvature $R = 90$ cm, reflecting the light towards a 5" PMT (ET 9390KB for the left HRS, and Photonis 4578B for the right) placed at a distance close to $R/2 = 45$ cm from the mirrors. The actual positions and angles of each individual PMT were optimized according to the expected spectrometer emittance, in order to keep the reflected Cherenkov photons in a small spot at the center of the photocathode and perpendicular to it. The adjacent mirrors partially overlapped to avoid "dark zones".

The number of photons with wavelength λ emitted per unit path length is given by [85]:

$$\frac{\partial^2 N}{\partial x \partial \lambda} \propto \frac{z^2}{\lambda^2}\Big(1 - \frac{1}{\beta^2(n(\lambda))^2}\Big), \tag{2.2}$$

where z is the electric charge of the particle producing Cherenkov radiation. It can be seen that majority of photons were emitted in the ultraviolet (UV) range. However, the PMTs used in the Gas Cherenkov counter didn't have UV transparent windows and hence had low quantum efficiency [77, 87] in this wavelength range (Fig. 2-12).

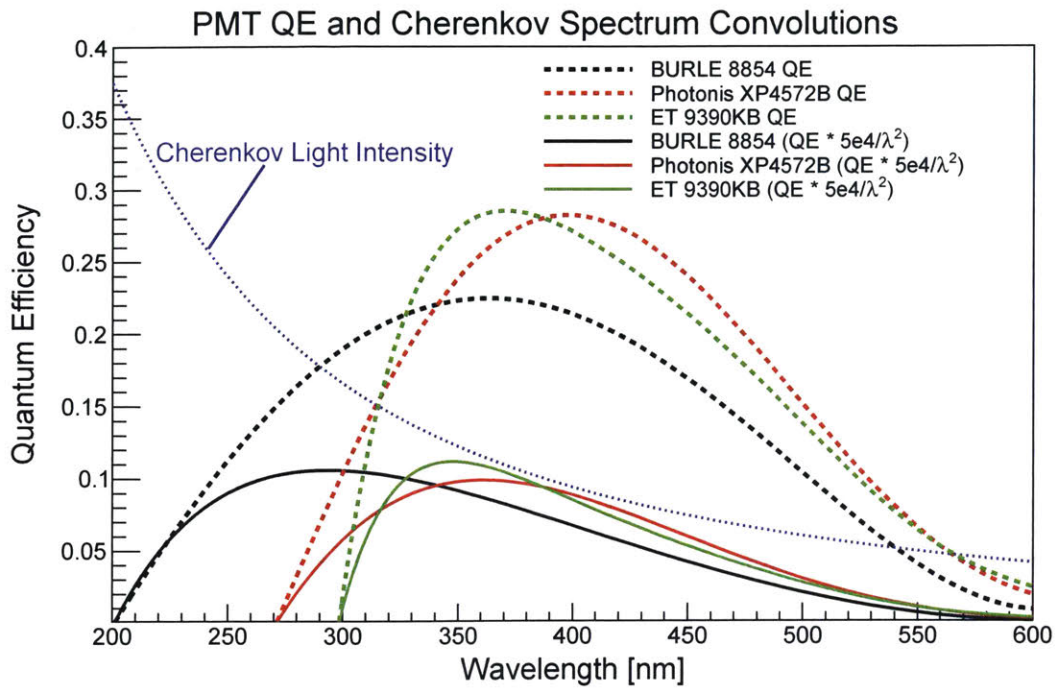

Figure 2-12: The spectrum of Cherenkov radiation, PMT quantum efficiency and the convolution for three types of PMTs. Reproduced from Ref. [88].

To boost their detection efficiency to the Cherenkov radiation, a wavelength shifting (WLS) paint was applied to the windows of the PMTs [88]. In a electron beam test performed in the fall of 2015, a 65% increase in the number of photoelectrons produced by the PMTs were demonstrated. The WLS paint's effect on the time resolution of the detector was found to be less than 2 ns. No degradation in the paint's performance was observed over the data-taking period of Experiment E12-07-108.

Lead Glass Shower Detector

Two layers of the lead glass shower detectors were installed in each HRS to provide additional information for particle identification. When a high energy electron traversed a dense material such as a lead glass, it lost its energy by the bremsstrahlung process. The emitted photon was then converted to an electron and a positron by pair production, which then led to a shower development. The Cherenkov light produced by the cascade of photons and electron-positron pairs was proportional to the energy

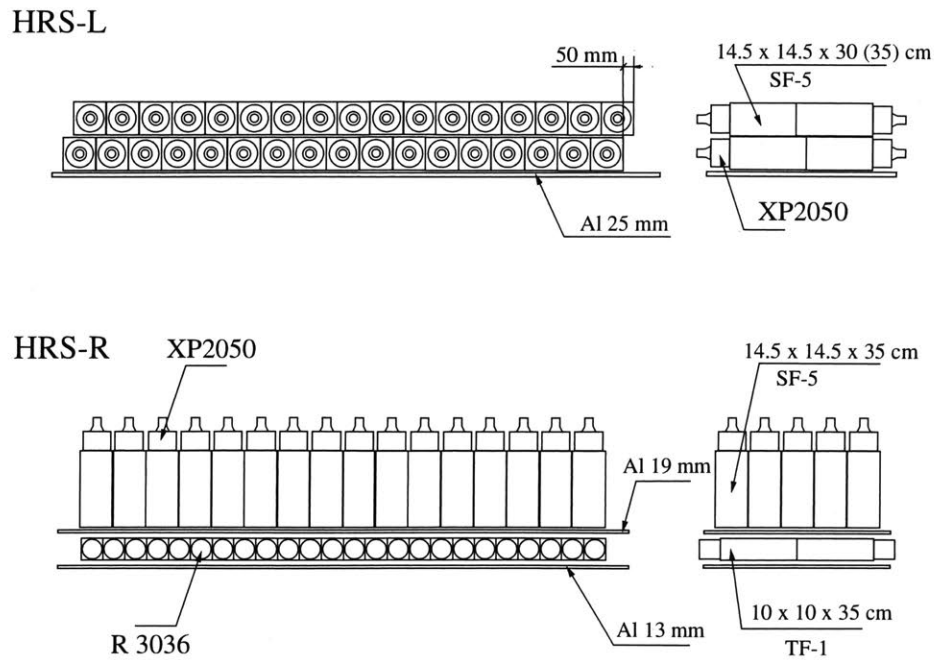

Figure 2-13: Schematic layout of the shower detectors in left (top) and right (bottom) HRSs.

deposited in the material and was detected by PMTs. Electrons deposited all of their energy in the shower detector, while hadrons, mainly pions, did not develop a shower due to the much larger nuclear interaction length [85] and could be rejected by the small amount of energy deposition in the shower detector.

The structure of the shower detectors in each arm is shown in Fig. 2-13. Both layers in the left HRS were composed of 17 (dispersive) $\times$ 2 (transverse) SF-5 [89] lead glass blocks perpendicular to the particle tracks. The second layer was shifted by about 5 cm towards the VDC so that the gap between blocks of the first layer was covered by a block of the second layer, and vice versa. The first layer in the right HRS was composed of 48 TF-1 [89] lead glass blocks, each of a dimension 10 cm $\times$ 10 cm $\times$ 35 cm. The second layer consisted of 75 SF-5 blocks parallel to the tracks, arranged in a 5 $\times$ 15 array. For the HRS-L calorimeter, the total thickness encountered by electrons was 11.8 radiation lengths. On HRS-R, the total thickness was 17.4 radiation lengths, which resulted in a full containment of the shower cascade induced by electrons in the momentum range of the spectrometers.

2.7 Hall A Data Acquisition System

The data-acquisition (DAQ) system in Hall A [90] used CODA (CEBAF On-line Data Acquisition System) [91] developed by the JLab data-acquisition group. CODA is a software and hardware framework for acquisition, monitoring, and storage of data of nuclear physics experiments at Jefferson Lab. Supported commercial hardware elements include front-end Fastbus and VME digitization devices (ADCs, TDCs, scalers), the VME interface to Fastbus, single-board VME computers running VxWorks operating system, Ethernet networks, Unix or Linux workstations, and a mass storage tape silo (MSS) for long-term data storage.

The custom software components of CODA are:

- Readout controllers (ROCs) which runs on the front-end crates to buffer collected data in memory and send them via the network to the event builder.
- An event builder (EB) which caches incoming buffers of events from the different controllers and merges the data streams coming from the same event.
- An event recorder (ER) which writes the data built by EB to the disk.
- An event transfer (ET) system that allows distributed access to the data on-line or insertion of data from user processes.
- The RunControl process that can set experimental configurations, start and stop runs, as well as reset and monitor CODA components.

The data acquisition activity is coordinated by the trigger supervisor (TS) [92] which synchronizes the read-out of the front-end crates and handles the dead-time logic of the system. For each accepted trigger by the TS, data collected at the front-end Fastbus and VME digitization devices are gathered and written to the hard disk according to the instructions of the aforementioned software components.

The Experimental Physics and Industrial Control System (EPICS) [93] is another important piece of software that monitors and controls various elements of the CEBAF and Hall A instrumentation. The information recorded by EPICS, such as beam

position, beam current, beam energy, and magnet status, are combined and written to the CODA data stream every few seconds during the data taking of Experiment E12-07-108.

2.8 Trigger Electronics

The trigger system was built from commercial CAMAC and NIM discriminators, delay units, logic units, and memory lookup units. There were two main types of triggers in Experiment E12-07-108: those formed from detectors and those from pulsers.

2.8.1 Triggers Formed from Detectors

The various detectors in the Hall A spectrometers can be used to form logic signals to trigger the DAQ. Such triggers are referred to as single detector triggers [94] and prove very useful in the process of detector checkout. From these base triggers, coincidence triggers can be created among the detectors and were used as the main triggers for production data taking in Experiment E12-07-108.

Scintillator Triggers

The S2m signals traveled through a mixer circuit with one-sixth of the signal amplitude going to an ADC and the remaining signal into a discriminator. The thresholds on the discriminators were set to -10 mV (Table 2.7). The logical OR of the discriminator outputs from each side of the detector were formed and their logical AND produced the S2m trigger. Copies of the individual discriminated signals were also sent into a Fastbus TDC and a VME scaler. The process is illustrated in Fig. 2-14.

The S0 trigger was formed in a similar way, but the two PMT signals were first sent into an amplifier module (10× amplification) prior to discrimination and formation of the S0 trigger (Fig. 2-15).

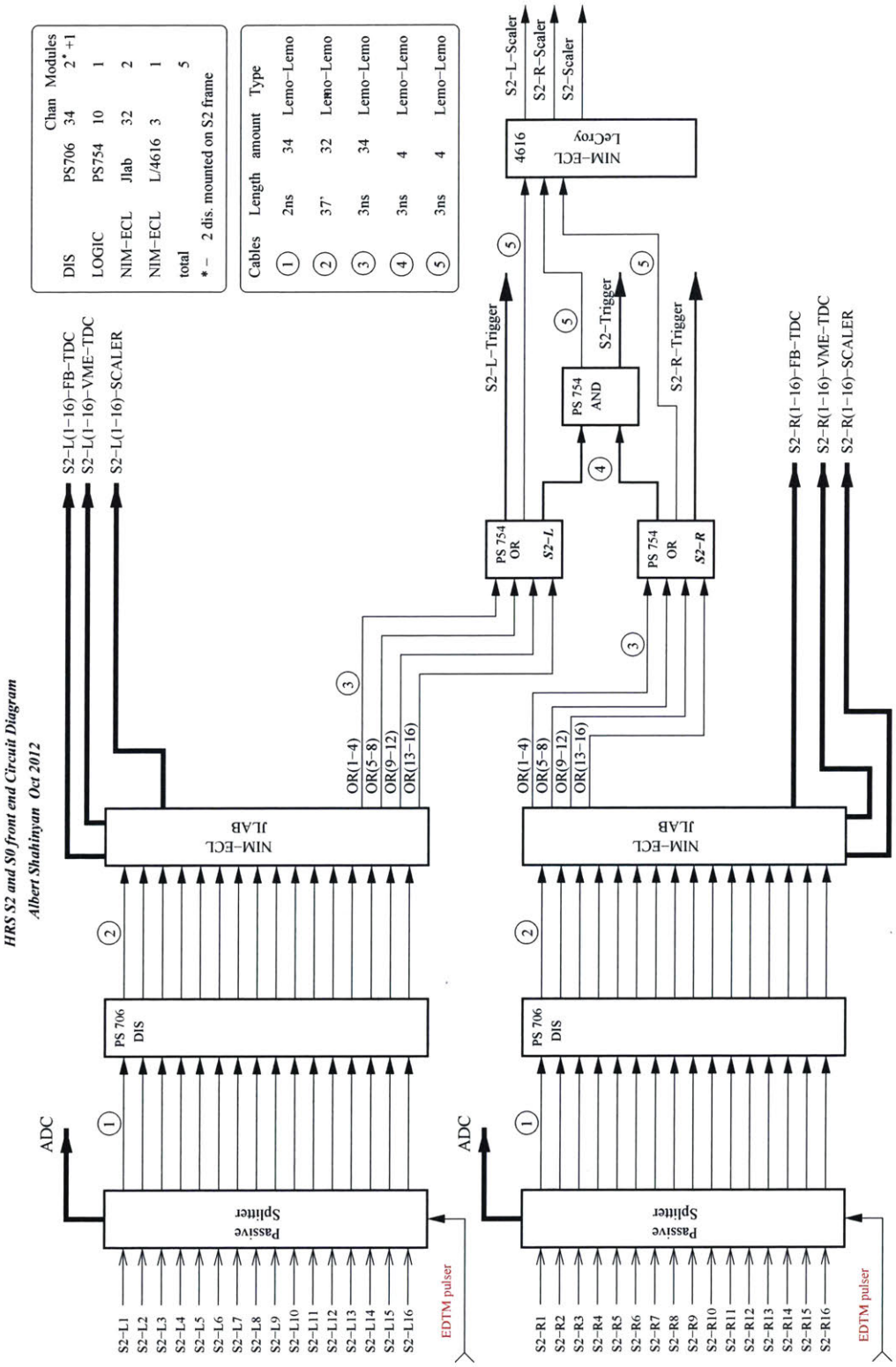

Figure 2-14: Schematics for the S2m trigger formation. Reproduced from Ref. [95]

Table 2.7: The discriminator thresholds for HRS detectors. Reproduced from Ref. [95]

Detector	Threshold
VDCs	3.0 V
Straw chambers	3.0 V
S0	-15 mV
S2m	-10 mV
GC (individual channels)	-15 mV
GC sum	-10 mV
Calorimeter sums	-20 mV

Gas Cherenkov Trigger

The ten PMT signals of the Gas Cherenkov detector were amplified and then sent into a linear fan-in/fan-out module to output an analog sum pulse. The sum was discriminated to form the GC trigger (Fig. 2-15).

Calorimeter Trigger

The calorimeter triggers for the L-HRS and R-HRS are illustrated in Figs. 2-16 and 2-17, respectively. The analog output of each calorimeter block is first sent to a linear fan-in/fan-out module to form the detector sum for each layer, and then the two sums are added to produce a total sum which, after discrimination, constitutes the trigger signal for the entire calorimeter.

2.8.2 Pulser Triggers

The pulser triggers are used as clocks for verification of synchronization between the DAQ crates and calculation of scaler rates. There are two primary clocks: the 1024 Hz and 103.7 kHz (fast clock). The 1024 Hz clock originates from a NIM module on the R-HRS, whereas the fast clock is produced from a VME module on the L-HRS.

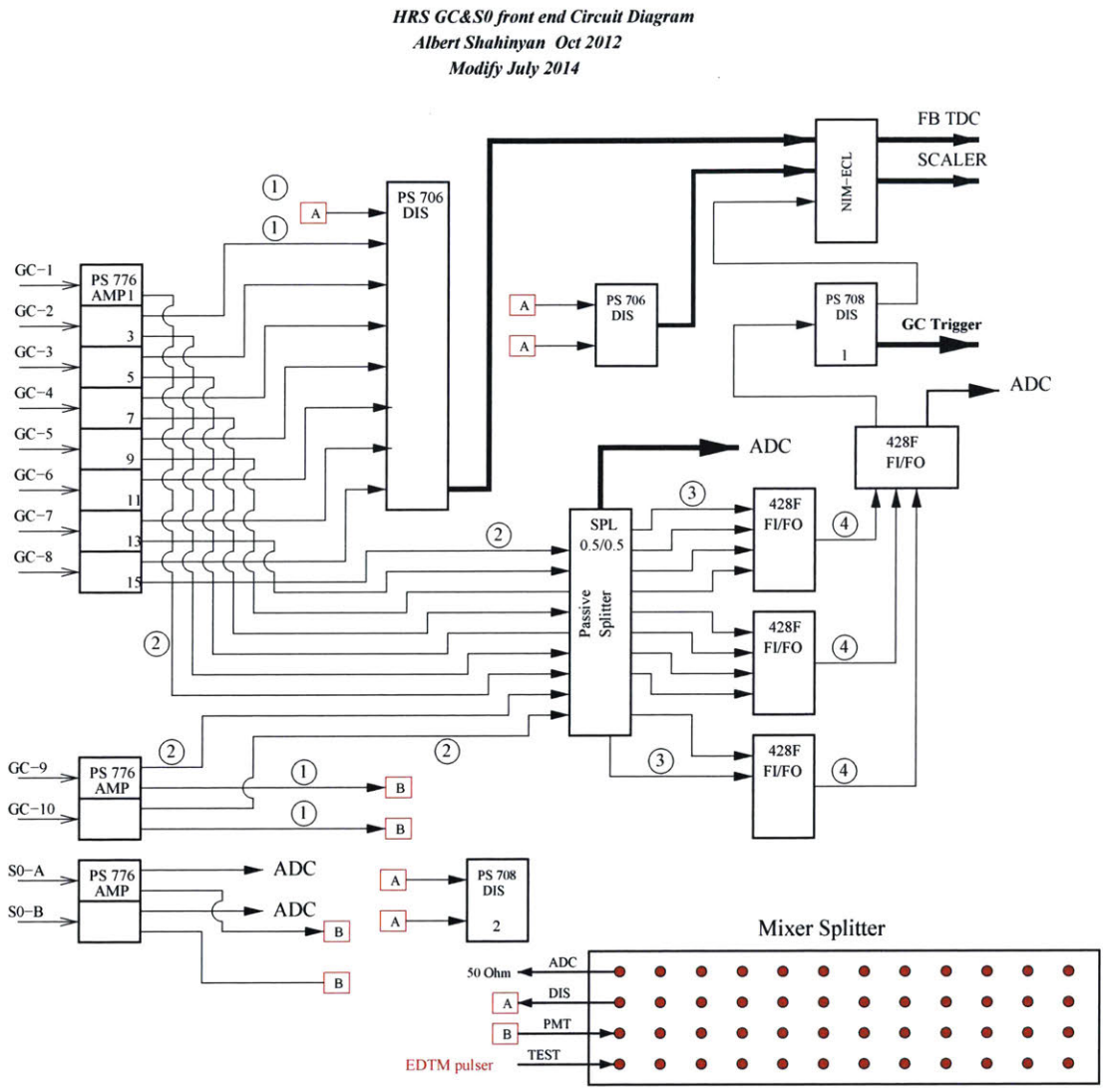

Figure 2-15: Schematics for the formation of the Gas Cherenkov and S0 triggers. Reproduced from Ref. [95]

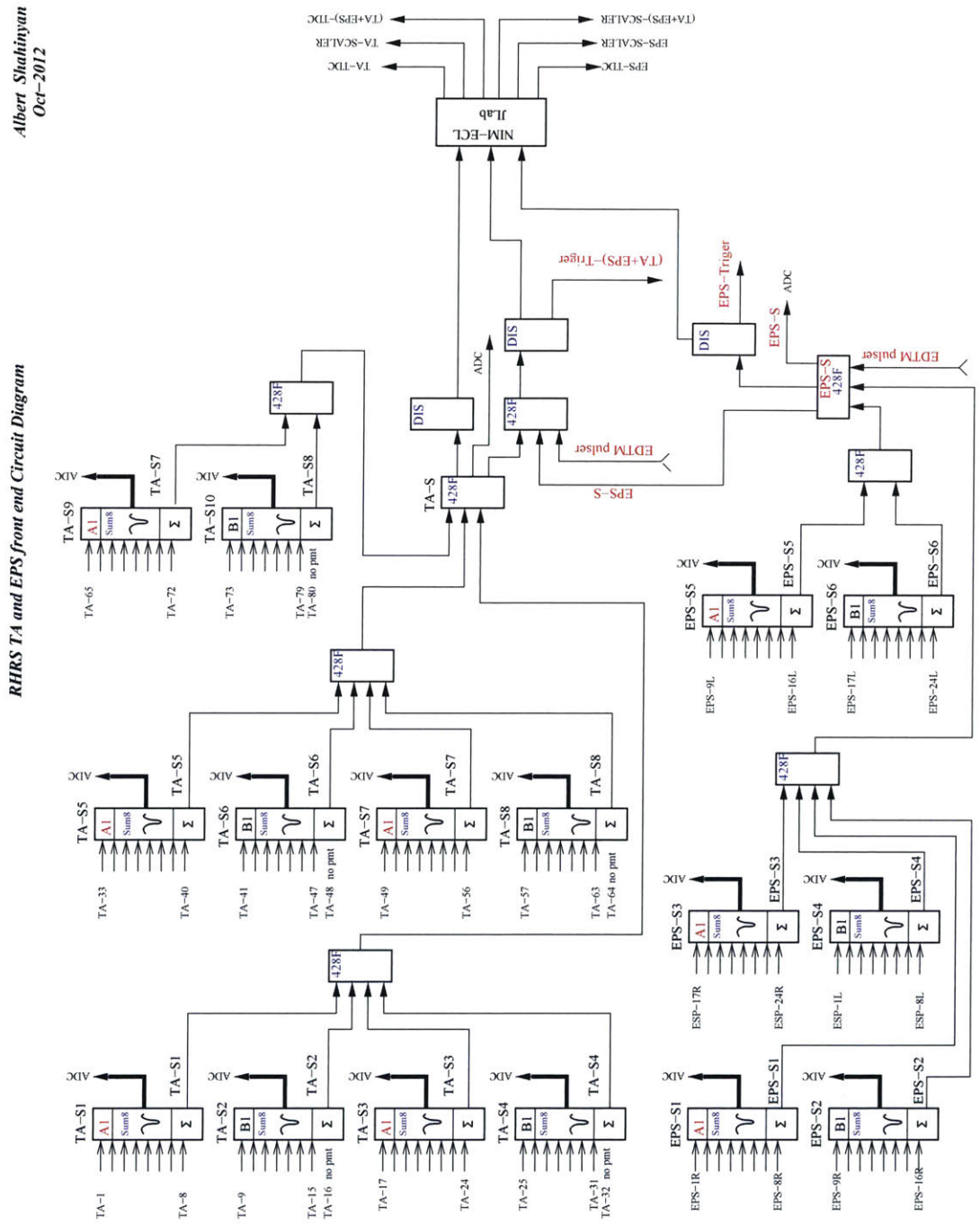

Figure 2-16: Schematics for the left HRS calorimeter trigger. Reproduced from Ref. [95].

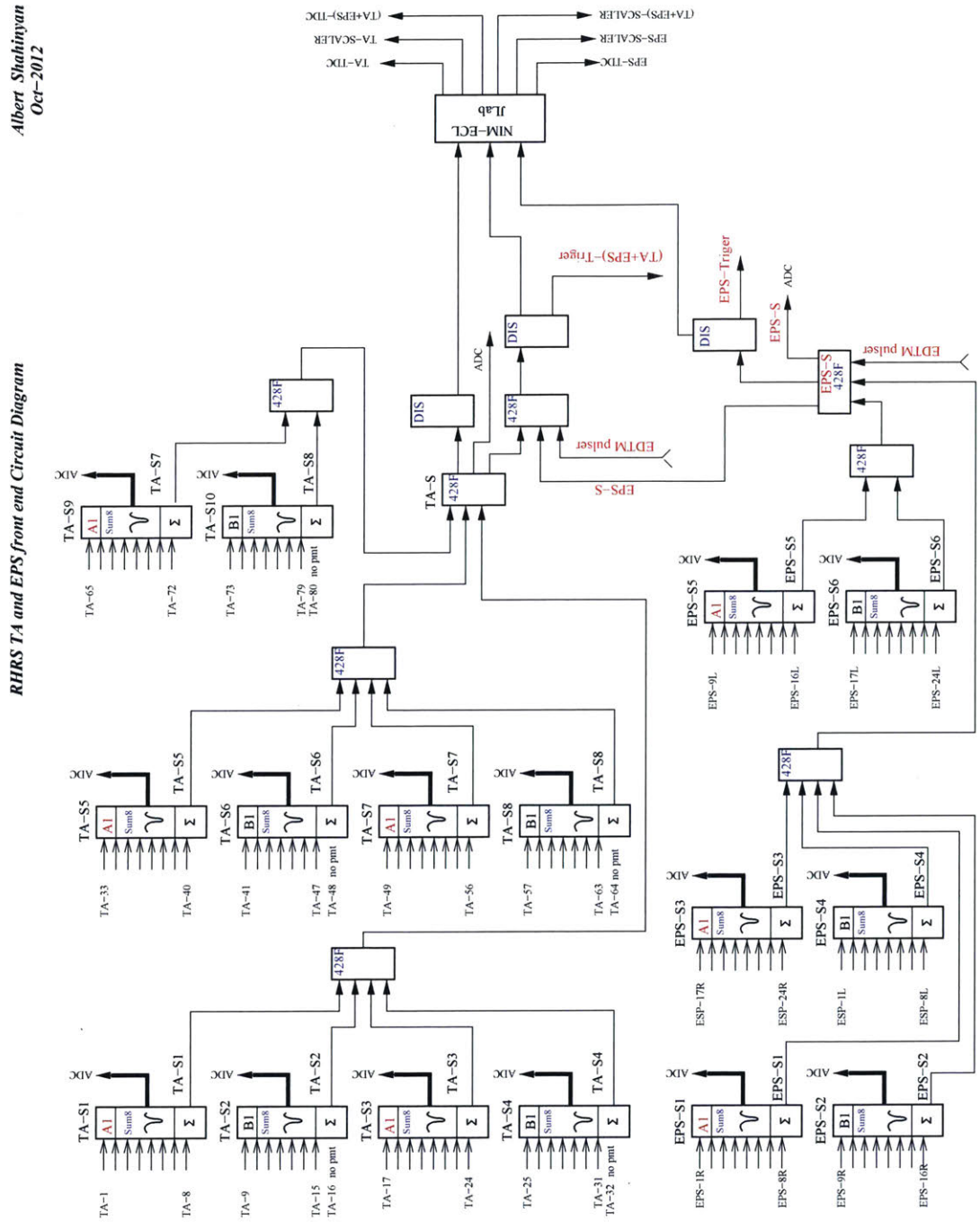

Figure 2-17: Schematics for the right HRS calorimeter trigger. Reproduced from Ref. [95].

Table 2.8: Inputs to the MLU in Experiment E12-07-108.

Input channel	Input signal
1	S0 trigger
2	S2m trigger
3	Gas Cherenkov trigger
4	Calorimeter trigger
5	Electronic dead-time monitor (EDTM) [95] signal
6	Clock
7	N.A.
8	N.A.

Table 2.9: MLU output configuration for single detector triggers and coincidence triggers.

Output channel	Output modes	
	Single detector	Coincidence
1	S0 trigger	S0 & S2
2	S2 trigger	S0 & GC
3	GC trigger	S2 & GC
4	Calorimeter trigger	S0 & Calorimeter
5	S0 || S2	S2 & Calorimeter
6	(S0 & S2) || (S0 & GC) || (S2 & GC)	GC & Calorimeter
7	EDTM	EDTM
8	Clock	Clock

2.8.3 E12-07-108 Standard Triggers

More sophisticated triggers between the detectors are created from the single detector triggers. This is accomplished using a CAEN 1495 VME board as a Majority Logic Unit (MLU) [94]. The MLU can take up to 8 NIM logic pulses as inputs and has two different modes. In each mode, it produces a total of 8 NIM outputs that can be programmed to be arbitrary logic functions of the inputs. The setup of MLU in Experiment E12-07-108 is summarized in Table 2.8.

The MLU is always programmed to be in the coincidence trigger mode during the data collection of Experiment E12-07-108. The 8 outputs from the MLU are sent

to a NIM-ECL converter and finally fed into the first 8 input channels of the TS (which can accept up to twelve separate level-1[1] trigger [95] inputs simultaneously). The TS unit has a prescale function. If the prescale factor for a specific trigger type is N, then only 1 out of N triggers of that type is recorded in the data stream. This function is very useful for reducing the computer dead time caused by frequent data record while keeping all events with useful physics information. For Experiment E12-07-108, the first three triggers were enabled by setting their prescale factors to be 1, and the clock trigger was prescaled to about 10 Hz. The other triggers were turned off with a prescale factor of zero. An input trigger to the enabled channels can generate a pattern of level-1 accept (L1A) signals, which are used by external electronics (transition module (TM), re-timing module, etc., see Ref. [95] for details) to generate ADC gates and TDC common stops.

[1]High energy particle and nuclear physics experiments often use a multi-level trigger system. The level-1 trigger usually retains those events that satisfy the physics selection criteria or fall in the regions of interest. It typically initiates the transfer to the next trigger level or to permanent storage. Higher level triggers enable more sophisticated decisions. In Experiment E12-07-108, only level-1 triggers were used due to the very low event rate and the inclusive setting.

Chapter 3

Data Analysis

3.1 Analysis Overview

The primary goal for this analysis was to precisely determine the elastic e-p scattering cross section for all kinematics listed in Table 2.1. The flow chart of the data analysis is shown in Fig. 3-1. The analysis utilized the Hall A C++ Analyzer [96] software package to convert the raw data to ROOT files [97], which store the detector information and the reconstructed physics variables in a machine-independent data structure that was optimized for quick access of the enormous amount of data produced by high-energy physics experiments. A calibrated database was used in this process to translate the detector readouts into quantities of physics interest. For each kinematic setting, electron events were then selected and the spectrum of invariant mass, after corrections for efficiency factors and background subtraction, was used to extract the elastic yield. In addition, a Monte Carlo (MC) simulation package was developed to simulate the elastic scattering process in the HRS. This package used transport matrices generated by COSY [98] to simulate the spectrometer optics and incorporated all relevant physics processes, including energy straggling, bremsstrahlung, multiple scattering, etc. The simulated yield was then weighted by the cross sections provided by an empirical fit to the world data. The cross sections were finally extracted by evaluating the data-to-MC yield ratio.

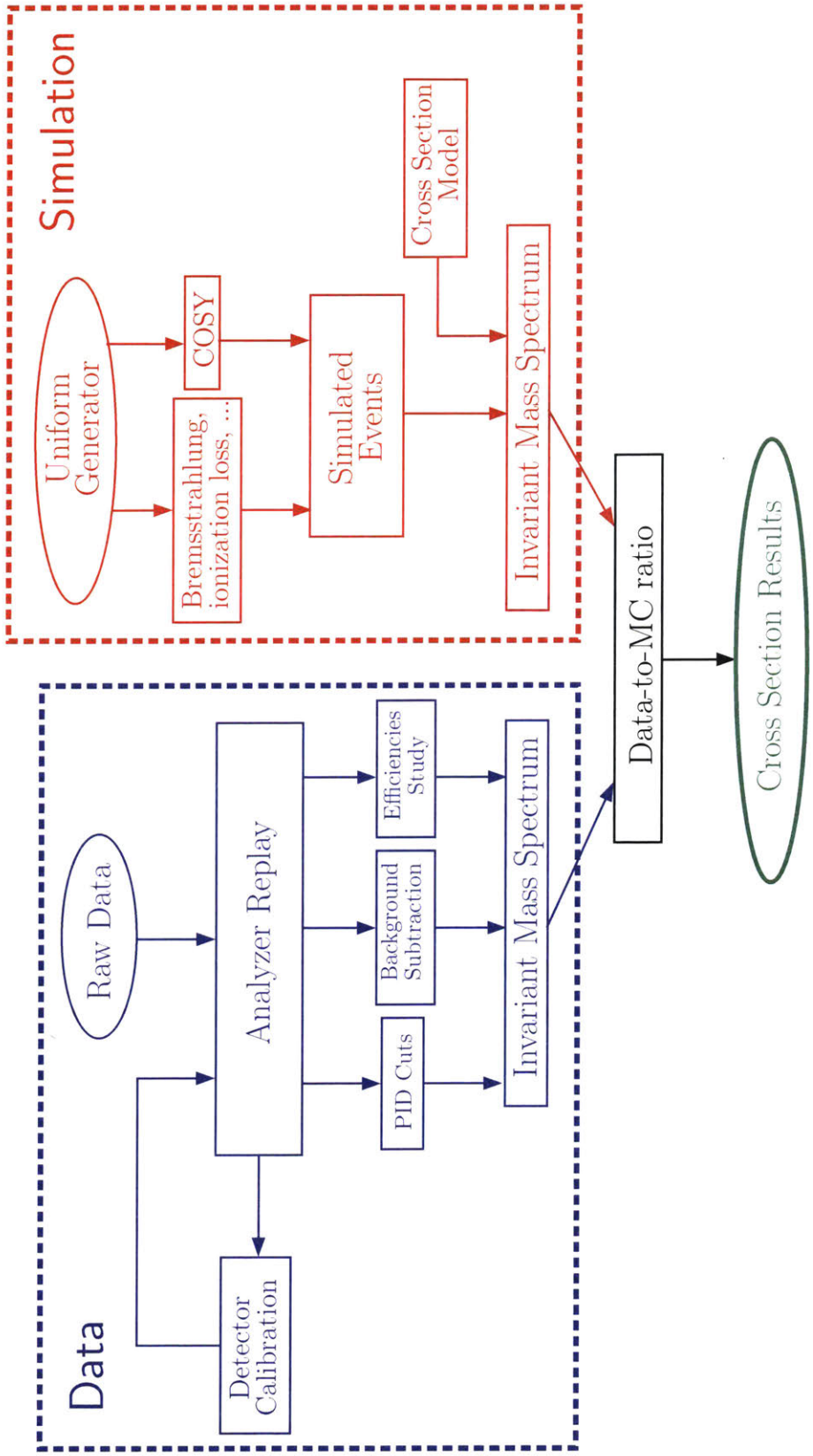

Figure 3-1: Analysis procedure for extracting the elastic e-p cross sections in Experiment E12-07-108.

3.2 Stability Check

The key parameters of the apparatuses during the experiment were monitored and recorded by the EPICS (Sec. 2.7) control system. These data were inserted to the raw data stream as a special event type [95, 99] and used to identify any glitches in the instruments and to check the quality of the detector data. In this section, the stability of the cryotarget temperature and HRS magnetic settings are discussed.

3.2.1 Temperature of the LH_2 Target

The liquid hydrogen used to scatter electrons in Experiment E12-07-108 was kept at a temperature of 19 K and a pressure of 1.7 atm and continuously flowed through the 15 cm long cylindrical target cell. Heat deposited by the beam was removed by circulating through a heat exchanger in contact with liquid helium coolant [100]. The average density of LH_2 was determined by the temperature as it entered and exited the target cell.

A total of three thermometers were used to monitor the operation temperature of the cryogenic target system. Thermometer 1 was located at the entrance of the cell and thermometer 2 at the exit. A third thermal sensor was installed after the LH_2 left the heat exchanger, and a heater existed between it and thermometer 1 to keep the temperature controllable at the cell entrance.

The recorded temperatures at the three sensors during data collection are shown in Fig. 3-2. The temperature at sensor 1 was the most stable since it was used in the proportion, integral, derivative (PID) feedback loop for automatic control of the valve of the coolant [76]. The average reading of sensors 1 and 2 was used to evaluate the relative fluctuation of the target temperature over the period of data taking [101]. This average was calculated for the recorded readings of the two sensors in the data streams of both left and right HRSs. The results were found to be consistent and the root-mean-squared spread was about 0.05 K [102], which translates into a 0.07% fluctuation in the density of LH_2 [73].

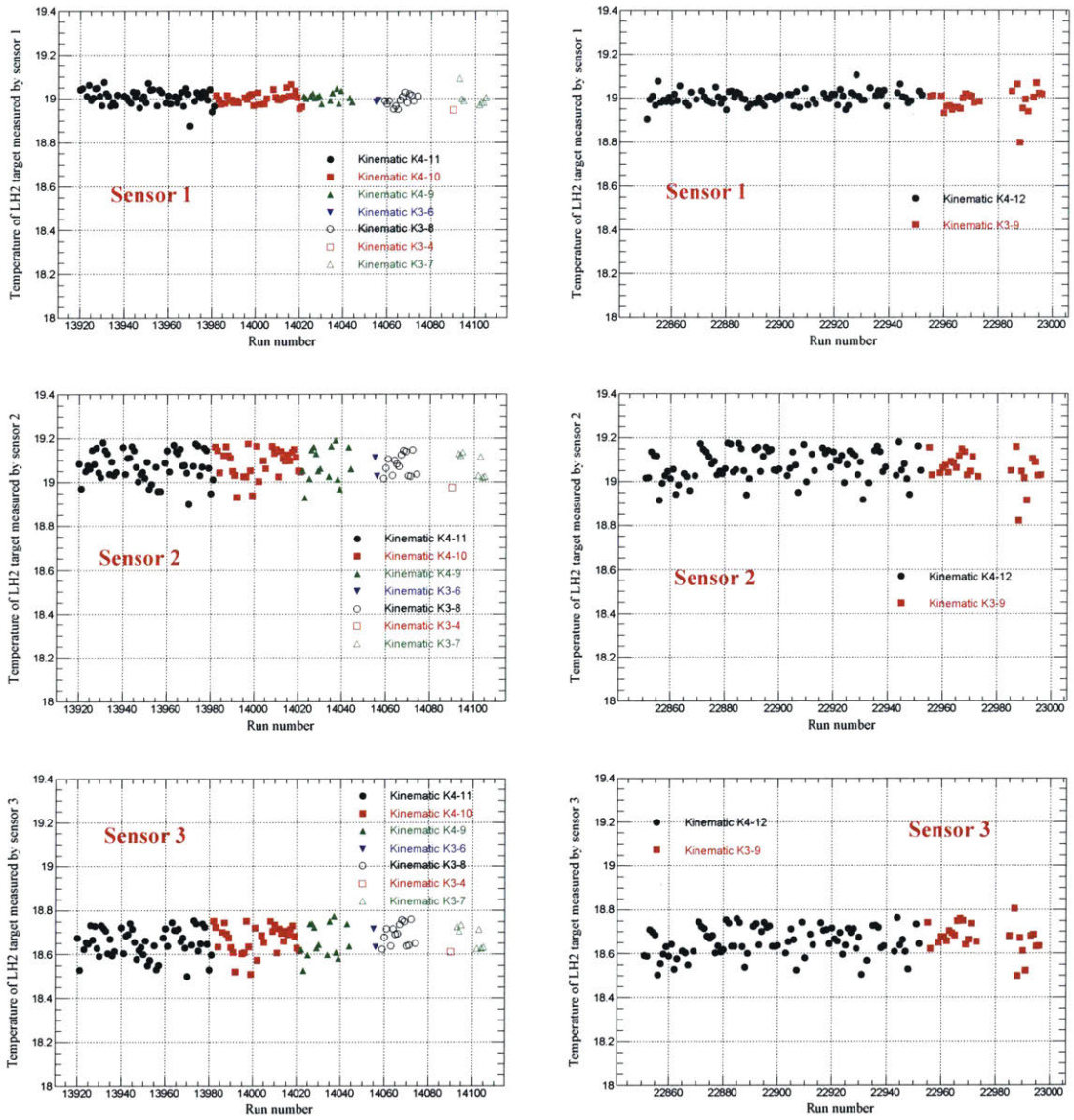

Figure 3-2: The readings of three thermometers at the cryotarget as recorded in the left (left column) and right (right column) HRS data streams.

3.2.2 Magnetic Field Settings

A set of magnetic probes was mounted in the HRS dipole and quadrupole magnets to monitor their field strengths during the experiment. The central momentum of the spectrometer was determined by the magnetic field measured in the dipole and the bending radius. A computer program was developed to automatically adjust the driving current in the three superconducting magnets according to the set values of the central momentum. A function was determined to set the currents in the SOS quad based on the set momentum. This function was based on a measurement of the fields as a function of the driving currents during the commissioning of the experiment. The SOS quad field was found to be linear in the driving current up to about 600 A, which corresponded to a field strength of about 1 Tesla at the pole tip [75].

Several values of the central momentum of the HRS were used during the collection of calibration and elastic scattering data in Experiment E12-07-108, ranging from 1 to 4 GeV/c on the left HRS and from 1 to 2.2 GeV/c for the right HRS. It turned out that the maximum driving current of 600 A in the linear range only corresponded to a set momentum of about 2.9 GeV/c. At kinematic settings with a set momentum higher than that, the increase of magnetic field with the driving current slowed down. This problem was discovered during an examination of the quality of the collected data after the experiment and rendered the standard optics matrices not directly applicable to reconstruct the target variables for these settings. None of the right HRS kinematics was affected by the saturation due to the large scattering angles and relatively low scattering momenta. The driving currents and measured magnetic field in the SOS quad is summarized in Table 3.1 for all left HRS kinematics.

The SOS magnetic fields shown in Fig. 3-3 and Table 3.1 were measured by a Hall probe. A later investigation revealed that the probe was mounted not so far from a high current cable connecting the coils and that an additional contribution from this cable was also picked up by the probe, resulting in its readout not fully reflecting the actual reduction in the field strength in SOS [103]. Using another probe, it was revealed that the actual saturation correction is larger than that suggested by Fig. 3-3

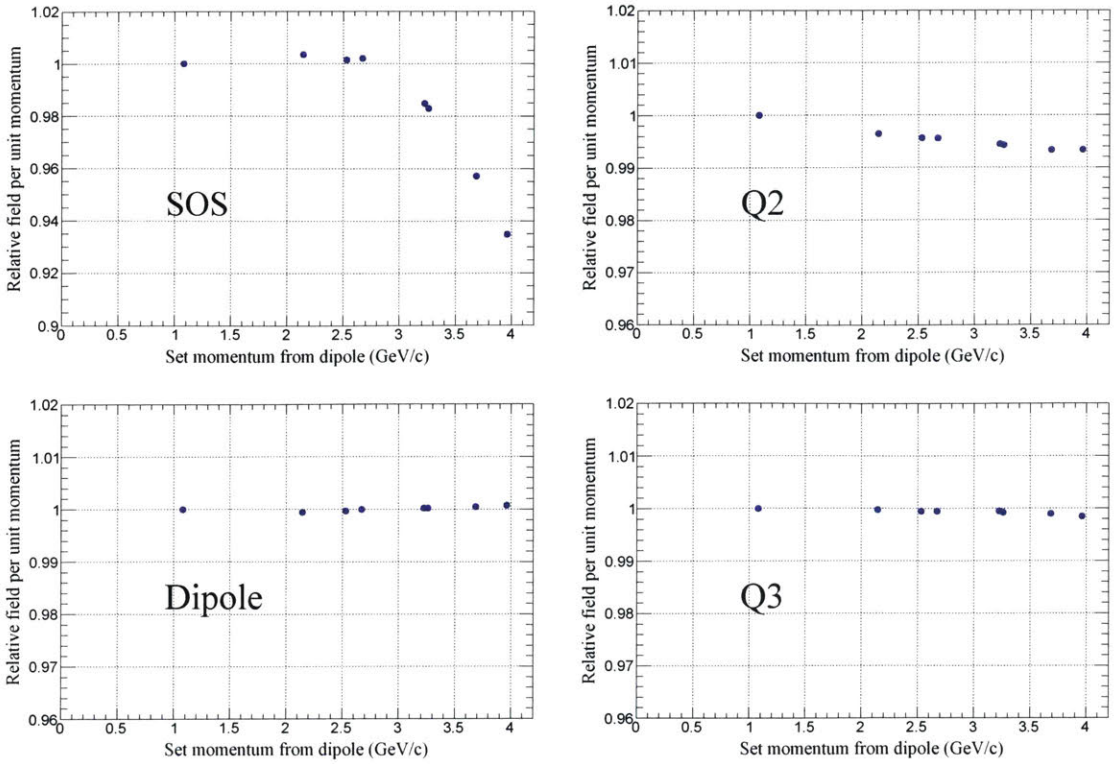

Figure 3-3: Examination of the field settings of the four magnets on the left HRS.

and Table 3.1. For example, at the highest set momentum (K3-4), a true reduction in the SOS field was found to be about 8%, while the E12-07-108 in situ data suggested 6.5%. A special procedure was used to find the impacts of the saturation effect on the optics reconstruction matrices, which is discussed in Sec. 3.6.4 and Ref. [104].

3.3 HRS Detector Calibration

In this section, the procedures for calibration of the various detectors on both HRSs are discussed. The configurations of the detector packages during E12-07-108 were described in Sec. 2.6.3. Most detectors were calibrated using standard techniques that were employed in numerous previous Hall A experiments. The calibration process is briefly discussed with references to more detailed descriptions in this case. A straw chamber for the study of VDC reconstruction efficiency constitutes the only non-standard item on both spectrometers and its calibration is described in detail in

Table 3.1: The left HRS SOS settings during Experiment E12-07-108 (Fall 2016). The first row shows the settings when taking deep inelastic data on multi-foil carbon target for angular and vertical optics calibrations (Sec. 3.4.2). The last column represents the relative variation in the magnetic field per unit momentum. The three settings K4-11, K3-8 and K3-7 do not suffer from the nonlinear relations between the currents and the resulting fields, while special treatments are required in the analysis of K4-10, K4-9, K3-6 and K3-4.

Kinematics	Set Momentum (GeV/c)	Current (A)	Magnetic field (T)	Relative B/p
Optics	1.08	225.25	0.3753	1
K4-11	2.531	527.88	0.8808	1.001
K4-10	3.259	679.72	1.1133	0.983
K4-9	3.685	768.57	1.2258	0.957
K3-6	3.224	672.41	1.1035	0.985
K3-8	2.145	447.38	0.7480	1.003
K3-4	3.962	826.35	1.2873	0.935
K3-7	2.672	557.29	0.9304	1.002

Sec. 3.3.2. A new technique for scintillator timing calibration was also developed and is described in Sec. 3.3.3. It improves the particle velocity reconstruction and will likely benefit timing analysis of future Hall A experiments.

3.3.1 VDC

The VDCs were used to reconstruct particle trajectories at the focal plane. It measured the drift time of ionized electrons from the trajectory to the sense wires and converted it into a perpendicular distance. A linear fit was then performed on these drift distances to determine the cross-over point. The straight line connecting the cross-points in the bottom and top VDCs defined the particle track.

The goal of VDC calibration was to determine a reference time t_0 for the TDC spectrum for each wire which accounted for the timing offsets due to variations in cable lengths and signal processing times. The rising edge of the drift time spectrum was first identified and the derivatives in this region were numerically evaluated. The maximum slope was then found and extrapolated to the drift-time axis. The intercept

defined t_0.

3.3.2 Straw Chamber

The straw chamber was used as an auxiliary tracking plane and helped to find the particle track parameters in the presence of multiple clusters in the VDCs. The positions of the six straw planes had to be well determined relative to the VDCs. This was achieved by a software alignment. This procedure makes use of the "golden" tracks which have a single cluster in all of the four VDC readout planes. VDCs could precisely measure the positions and slopes of these tracks at the focal plane. They were then projected to the six wire planes of the straw chamber. The alignment determined a set of translational and rotational offsets of each straw plane to minimize the sum of squared differences between the projected intercepts and the positions of the fired straw.

For the i-th (i = 1, 2, 3 for V planes and 4, 5, 6 for U planes) plane in the straw chamber, if we denote the projected intercept by y_i, the position of the fired wire by x_i, and the drift distance by s_i, the sum of squared difference can be expressed as follows:

$$\chi^2 = \sum_{i=1}^{6} \chi_i^2 = \sum_{i=1}^{6} (\frac{|y_i - x_i|}{\sqrt{1+f_i^2}} - s_i)^2, \tag{3.1}$$

where f_i is the projected slope of the track in the plane perpendicular to the straws and can be calculated as follows:

$$f_i = \frac{x'_{tra} + \tan\alpha}{1 - x'_{tra}\tan\alpha}\cos\theta_i + \frac{y'_{tra}}{-x'_{tra}\sin\alpha + \cos\alpha}\sin\theta_i. \tag{3.2}$$

Here x'_{tra} and y'_{tra} are the track slopes in the TRANSPORT coordinate system [1], and θ_i is the angle between the wires in the i-th plane and the TRANSPORT y axis: $\theta_{1,2,3} = 135°$ and $\theta_{4,5,6} = 45°$. α denotes the angle between the straw planes and the TRANSPORT x-y plane and has the value of zero in the nominal configuration.

[1] A coordinate system whose origin is located at the center of the bottom VDC and z axis is along the nominal track. Its x axis points in the dispersive direction and tracks with higher momentum usually has a larger x coordinate. See Ref. [105] for more details.

Dividing $|y_i - x_i|$ by the factor under the square root in Eq. 3.1 yields the closest distance between the track and the fired straw.

The position of the fired straw x_i is related to that of the first straw in the i-th plane f_{i0}, the number of the fired straw N_i, and the spacing Δ between straws:

$$x_i = (N_i - 1) \cdot \Delta + f_{i0}. \tag{3.3}$$

The drift distance is parameterized as a function of the measured drift time T using the Padé approximant [106]:

$$s_i = \frac{p_{i0} + p_{i1}T + p_{i2}T^2}{1 + p_{i3}T + p_{i4}T^2}. \tag{3.4}$$

A Minuit2 [107] based routine is used to minimize the χ^2 in Eq. 3.1. The spacing of straws, Δ, and the position of the first straw in the i-th plane in the TRANSPORT coordinates, f_{i0}, are fixed to the nominal value during the optimization. The alignment is performed in two steps. In the first step, the χ^2 in Eq. 3.1 is minimized with respect to the global position and rotation of the chamber while the drift distance is ignored. After that, the parameters for drift time to drift distance conversion are optimized to achieve the smallest squared difference between the projection of the VDC track and the intercept calculated using the position of the fired straw and drift distance. The whole process is iterated until the global offsets of the straw chamber do not change appreciably on subsequent iterations of the fit.

The residuals in the VDC track projection and the straw chamber reconstructed intercept are then plotted for each straw plane. As shown in Fig. 3-4, the average of the residuals is below 0.1 mm and the standard deviation is about 1.0 mm. It should be noted that this value does not reflect the intrinsic resolution of the straw chambers. The spread in the residuals is dominated by the multiple scattering in the materials between the VDCs and the straw chamber. The per-plane FWHM position resolution of 225 µm for the VDCs also contributes significantly due to the relatively long distance between the VDCs and the straw chamber.

The result of this procedure is examined by checking the correlations of the differ-

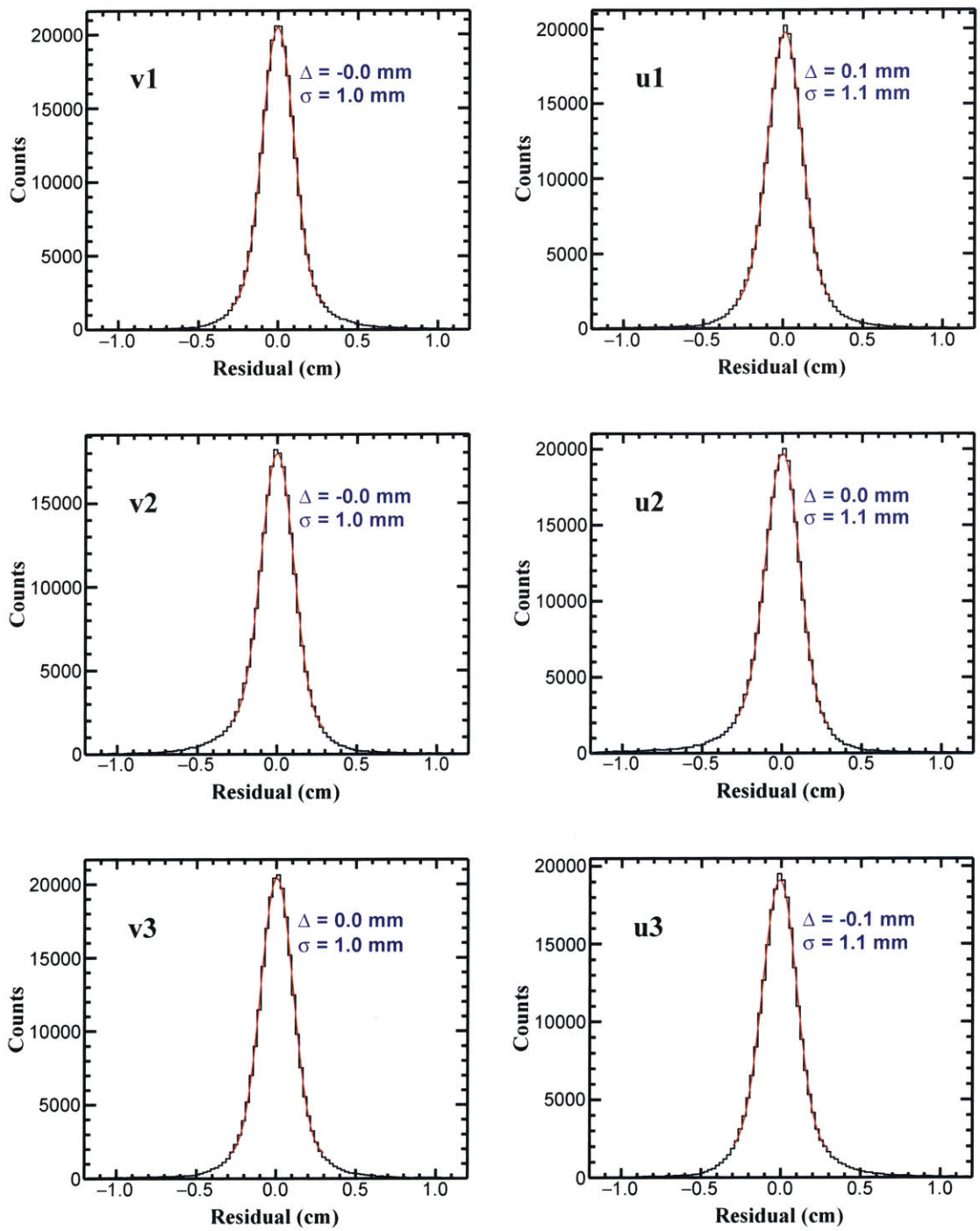

Figure 3-4: Difference between the projection of the HRS track to the straw chamber planes and the reconstructed hit by the position of the fired straw and its drift time. The left (right) column shows the residuals in the three V (U) planes.

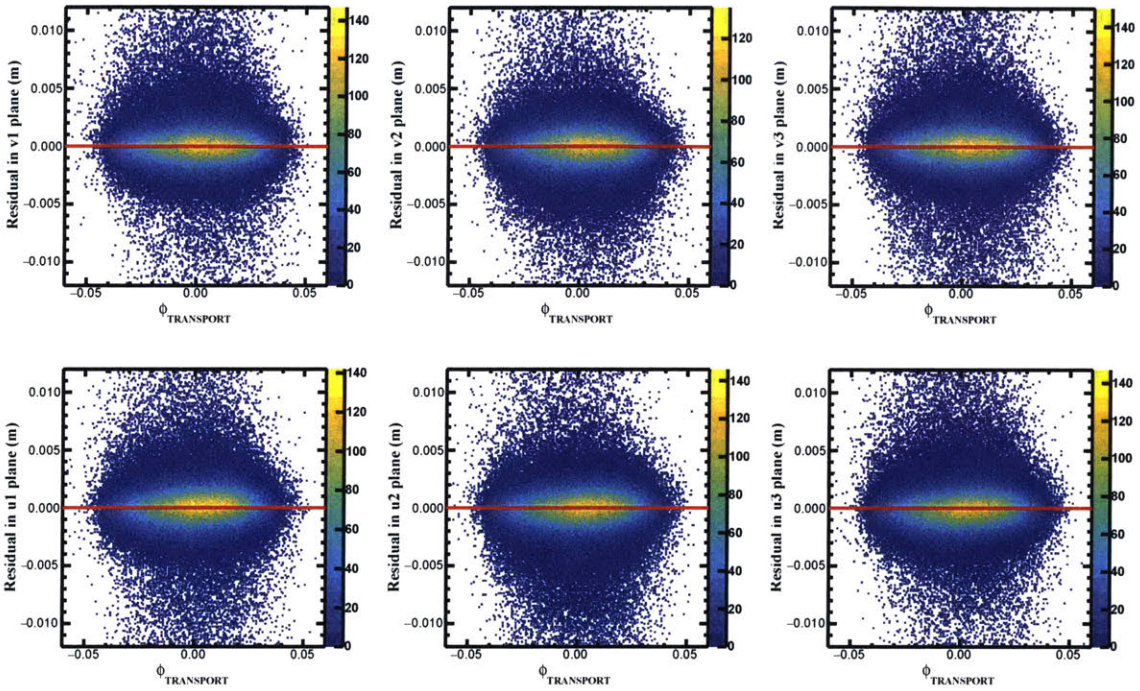

Figure 3-5: Difference between the projection of the HRS track to the straw chamber planes and the reconstructed hit by the position of the fired straw and its drift time, as a function of the HRS track slopes in the non-dispersive direction ($\phi_{\text{TRANSPORT}}$). The top (bottom) figures represent the correlations for the three V (U) planes.

ences in the VDC track projection and the intercept reconstructed by straw chamber with the VDC track parameters. As shown in Fig. 3-5, the difference shows no appreciable correlations with the slope of the track in the transverse direction after the alignment.

3.3.3 Scintillators

The analog signals from the PMTs attached to the scintillator paddles were sent to ADCs and, after discrimination, fed into TDCs to record the timing information of particles hitting the scintillator planes. Since the scintillators provided the main trigger for both HRSs (Sec. 2.8.3), it was important that the timing information encoded in the TDCs was correct. In addition, the combination of S0 and S2m comprised a hodoscope setup, which was suitable for measuring the time of flight (TOF) of the charged particles. This section discusses the procedure to determine the time offset for each scintillator channel. The ADC values of the scintillator detectors were not used in the analysis process.

Fig. 3-6 shows a basic diagram of a charged particle passing through an S2m paddle. The light emitted in the scintillator travels to each end and is detected by a PMT. The analog pulse generated by the PMT is then transmitted in the electric circuit, discriminated, and sent to a TDC. If we denote the moment that the particle hits the S2m by T_{S2m}, and the delays from the generation of the pulses to their detection in the TDCs by ΔT_L and ΔT_R for the left and right PMTs respectively, we can express the values measured by the TDCs as follows:

$$T_L = T_0 - (T_{\mathrm{S2m}} + \frac{L_0/2 - y}{c_n} + \Delta T_L), \tag{3.5}$$

$$T_R = T_0 - (T_{\mathrm{S2m}} + \frac{L_0/2 + y}{c_n} + \Delta T_R). \tag{3.6}$$

Here y is the distance from the hit position to the center of the paddle, c_n the speed of light in the scintillator material, and L_0 the full length of the paddle. T_0 denotes the moment when the common-stop signal arrives at the TDC. The calibration pro-

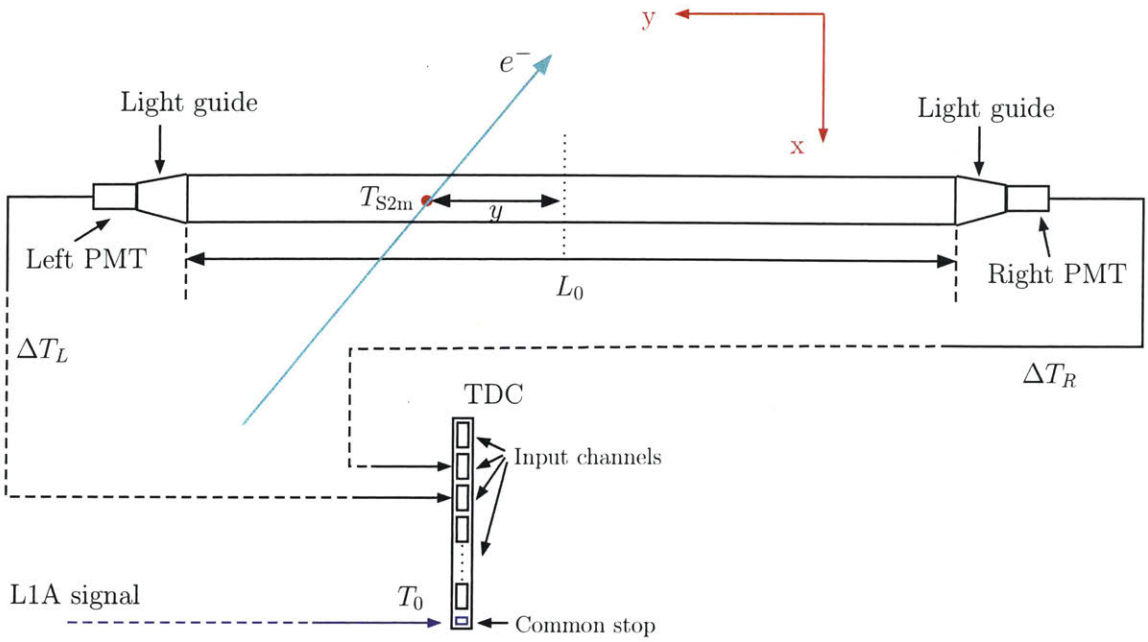

Figure 3-6: An electron passing through an S2m paddle and generating inputs to a TDC. The common stop generated from the L1A signal is also shown. The red axes indicate the positive x and y direction in the TRANSPORT coordinate system.

cedure involves the determination of the various timing offsets ΔT_L and ΔT_R. It is straightforward to adapt Eqs. 3.5 and 3.6 to the TDC values of S0 PMTs.

It is worth mentioning that the common stop signal was generated from the L1A signal of the trigger supervisor, so T_0 varied from event to event, depending on which detector carries the timing of the trigger signals sent to the trigger supervisor (Sec. 2.8.3). Even for events where S2m determined the trigger timing, T_0 could still be distinct if different scintillator bars were fired, since the offsets were not identical across all paddles. This caused difficulties in calibrating the scintillator timing. Previous efforts tried aligning the peaks of the corrected times for individual PMTs on the right of S2m, but that only resulted in a discontinuous spectrum of the reconstructed electron velocity when plotted as a function of the dispersive position of the track at the focal plane [108].

One should note that the absolute values of the TDC readings do not have any physical meaning themselves. It is the difference between these TDCs in the same event that delivers information about the detected particles. Being aware of this point,

we developed a procedure that can find the offsets ΔT_L and ΔT_R without knowledge about the timing of the trigger detector, and can bypass the difficulty brought by the variations in the cable lengths of PMTs attached to different scintillator paddles.

First, we take the difference between Eqs. 3.5 and 3.6 and get

$$T_L - T_R = \frac{2y}{c_n} + (\Delta T_R - \Delta T_L). \tag{3.7}$$

In the first step of the calibration, we performed a linear fit of $T_L - T_R$ to the projection of the track onto the scintillator plane along the direction of the bar for each paddle. According to Eq. 3.7, the intercept of the fit corresponds to $\Delta T_R - \Delta T_L$ and the slope is related to the speed of light in the material. The detailed results of the fits can be found in Ref. [109].

In the next step, we take the average of Eqs. 3.5 and 3.6 and get

$$\frac{T_L + T_R}{2} = T_0 - \left(T_{\mathrm{S2m}} + \frac{L_0}{2c_n} + \frac{\Delta T_L + \Delta T_R}{2}\right). \tag{3.8}$$

The factors $\frac{L_0}{2c_n}$ and $\frac{\Delta T_L + \Delta T_R}{2}$ in Eq. 3.8 are constants and have the same values for all events. Thus the average of the two TDC values carries direct information about T_{S2m}. The only missing part here is the T_0 which is related to the common stop signal of the TDC and can vary on an event basis.

The S0 correspondence of Eq. 3.8 is

$$\frac{T'_T + T'_B}{2} = T_0 - \left(T_{\mathrm{S0}} + \frac{L'_0}{2c'_n} + \frac{\Delta T'_T + \Delta T'_B}{2}\right), \tag{3.9}$$

where T'_T (the subscript T stands for top PMT, and B for bottom), T'_B, L'_0, c'_n, $\Delta T'_T$ and $\Delta T'_B$ have similar meanings to those in Eq. 3.8 but are associated with S0 now. The T_0 in Eq. 3.9 is the same as that in Eq. 3.8 since all TDCs share the common stop signal.

As can be seen, the T_0 term cancels out when we subtract Eq. 3.8 from Eq. 3.9:

$$\frac{T'_T + T'_B}{2} - \frac{T_L + T_R}{2} = (T_{\mathrm{S2m}} - T_{\mathrm{S0}}) + \left(\frac{L_0}{2c_n} - \frac{L'_0}{2c'_n}\right) + \left(\frac{\Delta T_L + \Delta T_R}{2} - \frac{\Delta T'_T + \Delta T'_B}{2}\right). \tag{3.10}$$

The term in the first parentheses on the right side of Eq. 3.10 is the time-of-flight of the charged particle from S0 to S2m, and can be determined as

$$\mathrm{TOF} = T_{\mathrm{S2m}} - T_{\mathrm{S0}} = \frac{L_{\mathrm{path}}}{c}, \tag{3.11}$$

where L_{path} is the pathlength of charged particle from S0 to S2m and can be calculated using the perpendicular distance between the two scintillator planes and the angle between the track and the z-axis in the TRANSPORT coordinate system.

Eq. 3.10 reveals that only the difference between $\Delta T_L + \Delta T_R$ and $\Delta T'_T + \Delta T'_B$ can be determined from the TDC values. This is also all we need to be able to calculate the TOF for the charged particles. There could be an arbitrary overall offset for these calibration coefficients. If we fix, say, ΔT_R to be zero, all the other coefficients, ΔT_L, $\Delta T'_T$ and $\Delta T'_B$ can be determined subsequently by utilizing the linear fits described in Eq. 3.7 and Eq. 3.10. The reconstructed β spectrum after the calibration (Fig. 3-7b) is now peaked at $\beta = 1$ and does not show any discontinuities as a function of the dispersive track position.

In Eqs. 3.5 and 3.6, it was assumed that the time offsets ΔT_L and ΔT_R are fixed for all particles firing the same scintillator bars. In practice, they are impacted by the variations in the amplitude and/or risetime of the signals generated in the PMT: signals with larger amplitudes cross the threshold of the discriminator at an earlier time. This is referred to as the time-walk effect [77]. In the Hall A analyzer, the time-walk effect is parameterized as

$$\Delta T_{\mathrm{tw}} = K \cdot \left(\frac{1}{\sqrt{\mathrm{ADC}}} - \frac{1}{\sqrt{\mathrm{ADC_{MIP}}}}\right), \tag{3.12}$$

where ADC is the recorded amplitude for a PMT attached to a particular paddle and $\mathrm{ADC_{MIP}}$ is an arbitrary timing offset declared for a minimum ionizing particle (MIP)

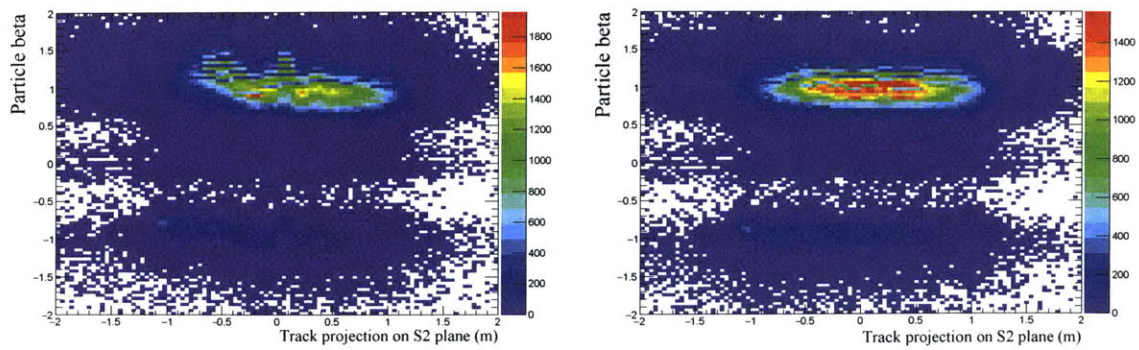

(a) Before calibration

(b) After calibration

Figure 3-7: Reconstructed particle velocity as a function of the projection onto the S2m plane in the dispersive direction before and after the timing offset calibration. The cluster at $\beta = 1$ is elastically scattered electrons collected at K3-9. The shadows at $\beta = -1$ are cosmic ray events. The stripey structures in both plots are caused by the limited resolution (0.5 ns/channel) of the TDCs.

for which the time-walk is zero.

In order to determine the coefficients K and $\mathrm{ADC_{MIP}}$ in Eq. 3.12 for S0 PMTs, it was assumed that the time-walk effect induced by the S2m PMTs can be ignored. This is justified by the fact that the S0 PMTs typically produce analog signals 10 times larger than the S2m PMTs do, thus time-walk correction is much more important for S0 PMTs. Hence the overall time-walk can be written as

$$\Delta T_{\mathrm{tw}}^{\mathrm{S0}} = K \cdot \left(\frac{1}{\sqrt{\mathrm{ADC}_T}} + \frac{1}{\sqrt{\mathrm{ADC}_B}} - \frac{2}{\sqrt{\mathrm{ADC_{MIP}}}}\right), \tag{3.13}$$

where ADC_T and ADC_B are the ADC values for the top and bottom PMTs attached to S0 respectively.

The correction factor $(\Delta T'_T + \Delta T'_B)/2$ from the right hand side of Eq. 3.10 was plotted as a function of $1/\sqrt{\mathrm{ADC}_T} + 1/\sqrt{\mathrm{ADC}_B}$ and a linear fit was performed. The result is shown in Fig. 3-8. The walk correction due to S0 was then pulled back into Eq. 3.10 and a similar procedure was carried out to find the correction due to S2m PMTs (we assumed that all S2m paddles share the K and $\mathrm{ADC_{MIP}}$ parameters). The result is presented in Fig. 3-9. The reconstructed electron velocities after applying

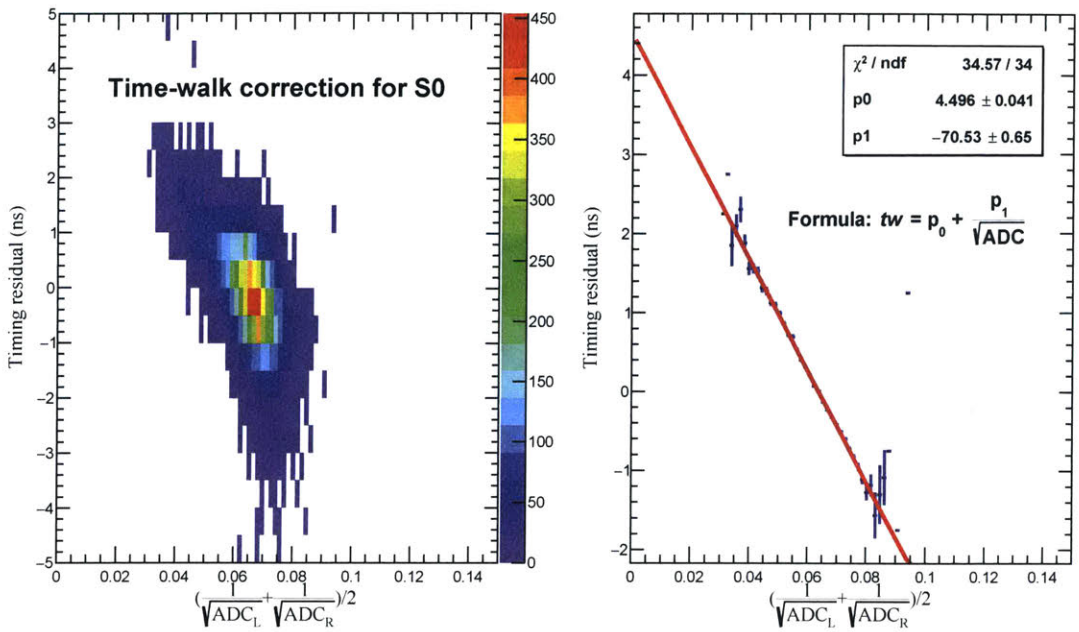

Figure 3-8: Time-walk correction for S0 PMTs.

the time-walk correction are shown in Fig. 3-10.

Due to the short distance (about 1.5 m [110]) between the two scintillator planes and limited TDC resolution (0.5 ns/channel), the measured TOF could not be used to separate electrons from hadrons. However, it proved useful in identifying cosmic ray backgrounds, which resulted in a peak at $\beta = -1$, since they came in the opposite direction to the beam events. The details about cosmic ray suppression will be discussed in Sec. 3.8.1.

3.3.4 Gas Cherenkov Counter

The outputs from the 10 PMTs attached to the Gas Cherenkov Counter were used as a measure of the Cherenkov light yield of the charged particle in the radiator. Since each PMT was supplied with a different high voltage and their overall amplification factors differed, their sensitivities to the photo-electrons were distinct. In order to sum the ADC values of the PMT outputs to extract the total light yield, it was necessary to align their responses to a single photo-electron.

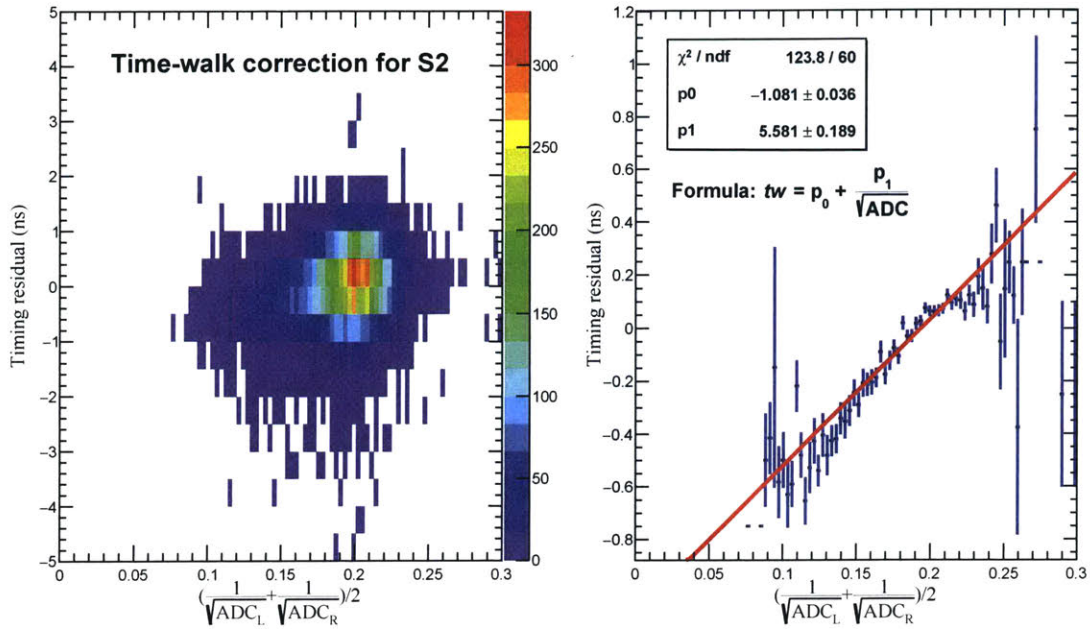

Figure 3-9: Time-walk correction for S2m PMTs

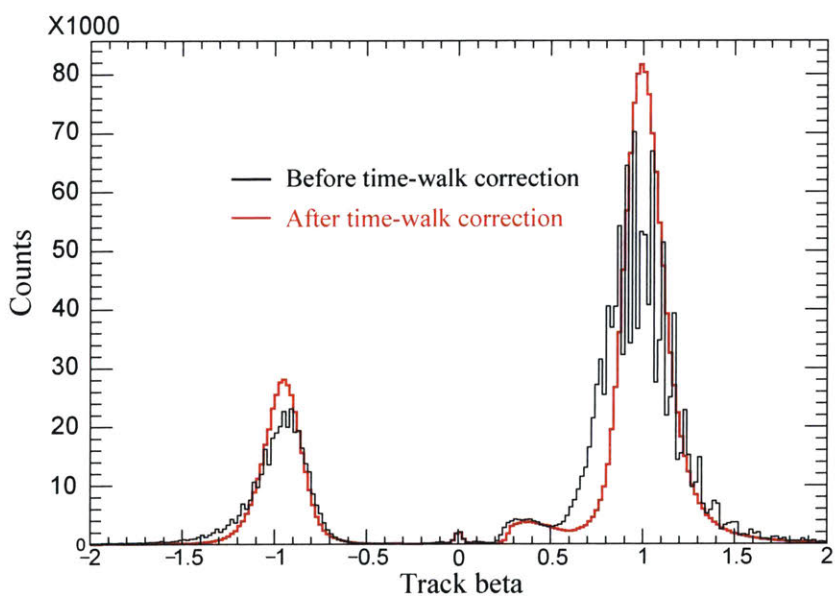

Figure 3-10: Reconstructed particle velocity before and after correction for the time-walk effect. The spiky structure in the β spectrum before the correction is due to the limited resolution (0.5 ns/channel) of the TDCs.

In the calibration process, a gain-matching coefficient was produced for each individual PMT. It was chosen so that the ADC spectrum, multiplied by the calibration coefficient, was peaked at the ADC channel 100. The aligned ADC spectra were then summed to produce the software Cherenkov sum and used for particle identification.

Fig. 3-11 shows a spectrum of the Cherenkov ADC software sum after calibration for a deep inelastic scattering setting. These data were collected for angle and vertex calibrations of HRS optics matrices (Sec. 3.4.2). The Cherenkov sum was divided by the peak of the single-photo-electron spectrum to give the number of photo-electrons detected by the PMT. The momenta of pions were below the threshold for Cherenkov light production in the radiator, so the blue curve in Fig. 3-11 is peaked at 0. In contrast, electron events typically resulted in a large Cherenkov sum and thus could be separated from hadrons. It is also worth noting that the number of photo-electrons detected in electron events averaged about 20, which is significantly higher than the value obtained in previous experiments [108]. This observation confirms the effects of the wavelength shifting paint on the efficiency of the GC counter (Sec. 2.6.3). A similar number of photo-electrons were detected by the Gas Cherenkov Counter on the left HRS since the thickness of the radiator was roughly the same.

3.3.5 Shower Detectors

The shower detectors used the energy deposition of particles to separate electrons from hadrons. A group of adjacent fired blocks was first identified as a cluster and the total energy E was given by the sum of all energies in the blocks of the cluster:

$$E = \sum_{i \in M} E_i = \sum_{i \in M} C_i \cdot A_i. \tag{3.14}$$

M here denotes the set of block numbers that are included into the cluster, A_i is the ADC readout of block i, and C_i is the conversion factor that relates the ADC value to the deposited energy. The calibration of shower detectors determines the value of C_i for each shower block.

The magnitudes of ADC output from all the shower detector blocks were matched

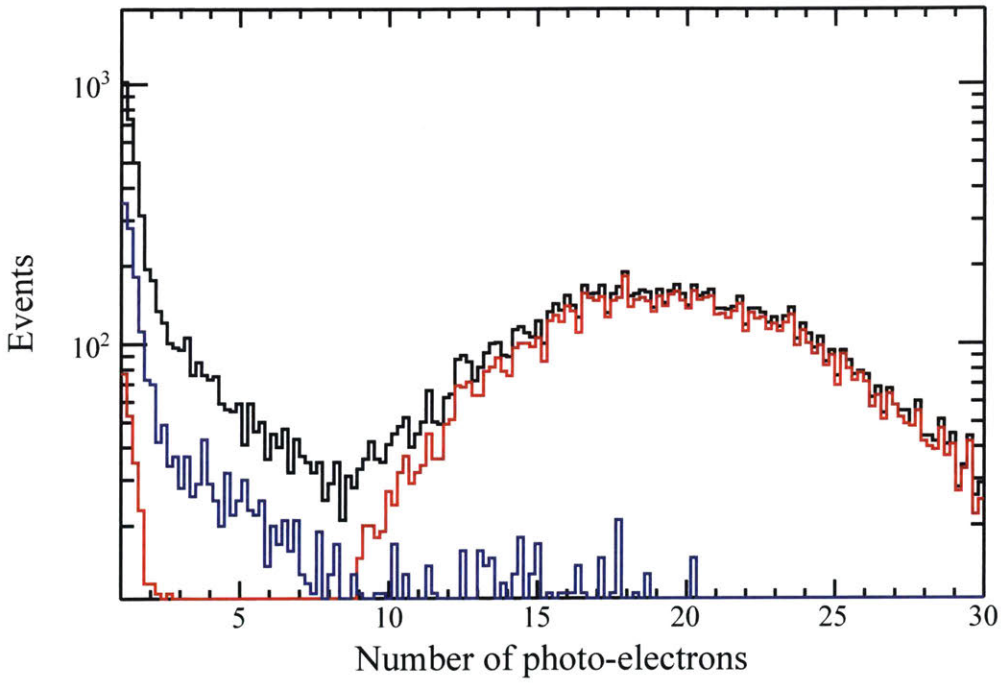

Figure 3-11: A scaled Gas Cherenkov ADC software sum on right HRS after calibration. Cuts on the shower detector signals (Sec. 3.3.5) were applied to reveal the distinct spectra for pions (blue) and electrons (red). Black curves are the overall distribution of the Cherenkov sum for all events.

preliminarily by adjusting the high voltage supplies to the PMTs using cosmic ray events. This process ensured that the calibration coefficients C_i have similar values and each block was about equally sensitive to incoming particles. This is important for achieving a uniform electron detection efficiency for the shower trigger (Sec. 2.8.3).

The calibration constants C_i were determined by minimizing the following function:

$$\chi^2 = \sum_{i=1}^{N} \Big(\sum_{j \in M^i_{\rm ps}} C_j \cdot A^i_j + \sum_{k \in M^i_{\rm sh}} C_k \cdot A^i_k - P^i \Big)^2. \tag{3.15}$$

Here P^i denotes the momentum of the charged particle defined by its track parameters (Sec. 3.4). N is the total number of events used for calibration. The weighted ADC signals were summed in both preshower and shower detectors (or the two layers of pion rejectors for left HRS) to get the total energy deposition. Since all the events in the calibration sample were electrons selected by requesting a large signal in the GC counter, the entire amount of their energies was lost in the lead glass calorimeters.

The results of the calibration are shown in Fig. 3-12. The shower detectors on the right HRS achieved an energy resolution of 5% at a momentum of 1.2 GeV/c, while a similar resolution was only reached at a higher incoming momentum of 2 GeV/c on the left HRS due to the limited radiation lengths of the pion rejectors.

As shown in Fig. 3-13, a clear separation between electrons and pions was achieved after the calibration procedure. The ratio of the total energy deposited in the shower detector to the particle momentum is peaked at one for electrons, while hadrons result in a much smaller fraction of energy deposition.

Due to the segmented structure of the calorimeter, the positions of the center of the clusters can be determined by an energy-weighting method:

$$X = \sum_{i \in M} X_i \cdot E_i / E, \tag{3.16}$$

$$Y = \sum_{i \in M} Y_i \cdot E_i / E, \tag{3.17}$$

where X_i and Y_i are the position of the center of the block i in the dispersive and non-dispersive directions, respectively. The position information could be used to

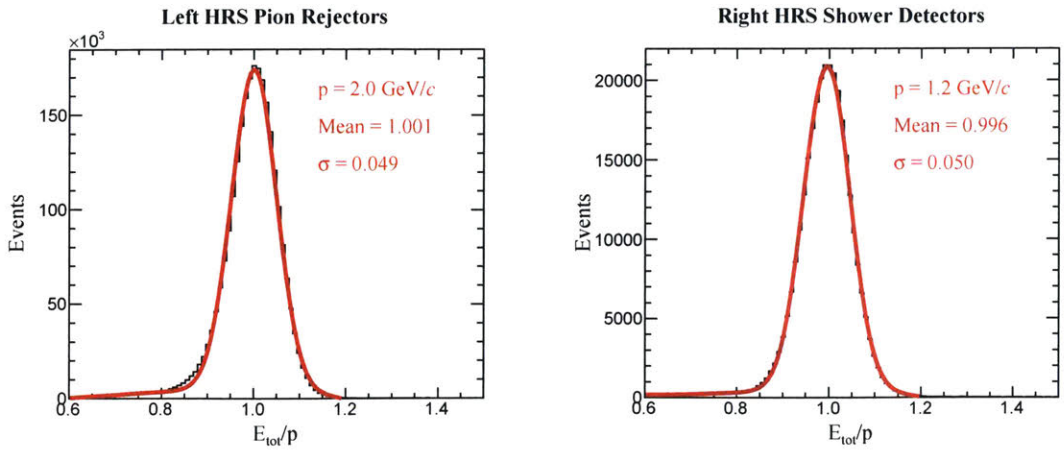

Figure 3-12: Results of calorimeter calibration for left and right HRSs.

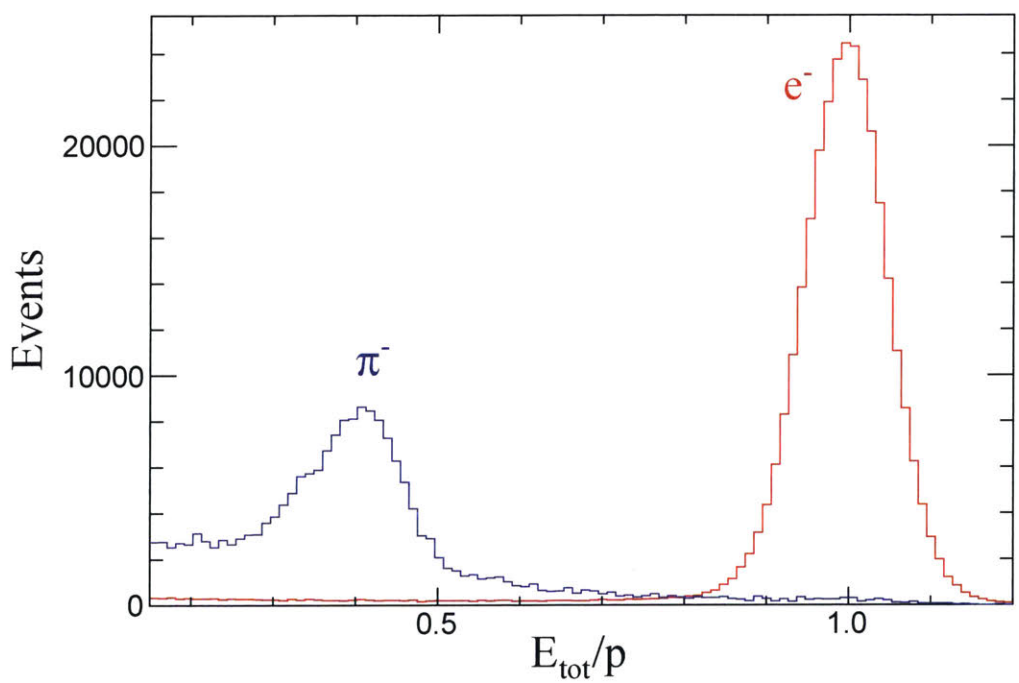

Figure 3-13: Separation of electrons from pions in the lead-glass shower detector on right HRS. The horizontal axis denotes the total deposited energy E_{tot} divided by the track momentum p. Data shown here was taken during one of the delta scan runs ($\delta = +4\%$, see Sec. 3.4.2 for more details). The pion curve is scaled up by a factor of 10 so that it can be viewed on the same scale as the electron (red) curve. Electrons (pions) are chosen by a Gas Cherenkov cut of greater (less) than 5 photo-electrons.

check against the projection of the VDC track onto the shower plane. More detailed information about the shower detector algorithm and calibration procedure can be found in Ref. [111].

3.4 HRS Optics Calibration

The two HRSs were used to determine the 3-D momentum and vertex of the scattered electrons at the target. The reconstruction of such quantities is based on the coordinates of the detected particles at the focal plane and a set of optics matrix elements. The calibration of the optics matrices for Experiment E12-07-108 will be discussed in this section.

3.4.1 HRS Coordinates and Optics Matrices

Each HRS was bundled with a target coordinate system (TCS) whose z axis was along the central ray of the spectrometer and the x axis pointed vertically down. The trajectory of the scattered particle at the target was characterized by a set of four quantities defined in the TCS (Fig. 3-14): the transverse position $y_{\rm tg}$, the horizontal (in-plane) and vertical (out-of-plane) angles relative to the spectrometer central ray — $\phi_{\rm tg}$ and $\theta_{\rm tg}$, and the relative momentum $\delta = \Delta p/p_0 = (p - p_0)/p_0$, where p_0 and p are the set momentum of the spectrometer and the magnitude of the particle's momentum respectively. The TCS variables are used to calculate the scattering angle, reaction vertex, and the physics variables of interest (e.g., the invariant mass of undetected system). For instance, the scattering angle and the reaction point are related to $\theta_{\rm tg}$, $\phi_{\rm tg}$, and $y_{\rm tg}$ by

$$\theta_{\rm scat} = \arccos\left(\frac{\cos(\theta_0) - \phi_{tg}\sin(\theta_0)}{\sqrt{1+\theta_{tg}^2+\phi_{tg}^2}}\right), \tag{3.18}$$

$$z_{\rm react} = \frac{-(y_{tg}+D_y) + x_{\rm beam}(\cos(\theta_0) - \sin(\theta_0))}{\cos(\theta_0)\phi_{tg} + \sin(\theta_0)}, \tag{3.19}$$

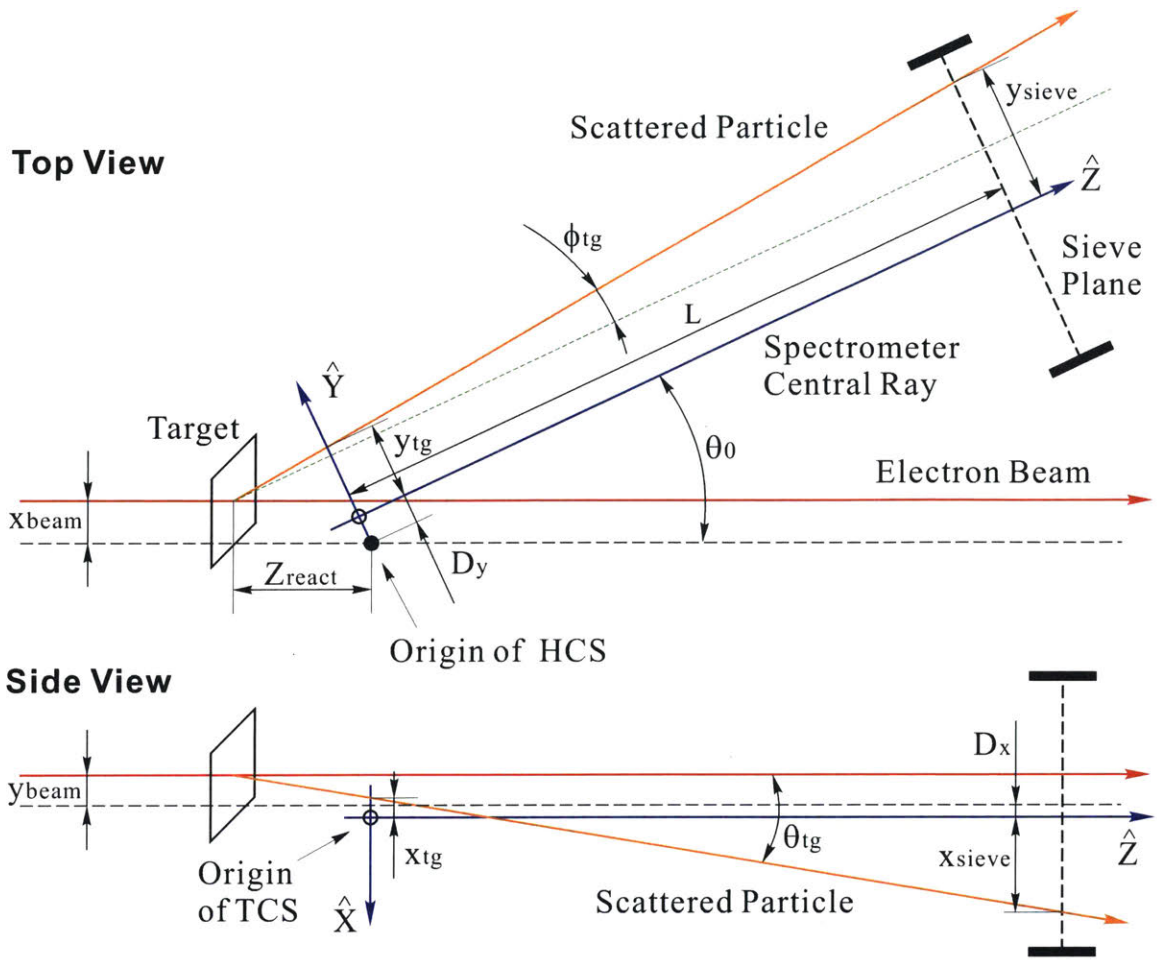

Figure 3-14: The definition of target coordinate system (top and side views). Also shown are the in-plane angle (ϕ_{tg}), out-of-plane angle (θ_{tg}), and transverse position (y_{tg}) associated with the trajectory of a scattered particle.

where θ_0 is the spectrometer central angle and x_{beam} denotes the position of the incoming electrons with respect to the center of the beam line.

The mapping between the target variables and the particle's track parameters at

the focal plane are parameterized as a set of polynomials:

$$\delta = \sum_{jkl} D_{jkl}\theta_{\rm fp}^{j} y_{\rm fp}^{k} \phi_{\rm fp}^{l}, \tag{3.20}$$

$$\theta_{\rm tg} = \sum_{jkl} T_{jkl}\theta_{\rm fp}^{j} y_{\rm fp}^{k} \phi_{\rm fp}^{l}, \tag{3.21}$$

$$y_{\rm tg} = \sum_{jkl} Y_{jkl}\theta_{\rm fp}^{j} y_{\rm fp}^{k} \phi_{\rm fp}^{l}, \tag{3.22}$$

$$\phi_{\rm tg} = \sum_{jkl} P_{jkl}\theta_{\rm fp}^{j} y_{\rm fp}^{k} \phi_{\rm fp}^{l}. \tag{3.23}$$

The $\theta_{\rm fp}$, $\phi_{\rm fp}$ and $y_{\rm fp}$ are the track parameters measured at the focal plane after correcting for any detector offsets from the ideal central ray of the spectrometer. To be more precise, they are defined with respect to a locally rotated coordinate system where the rotational angle depends on the intercept of the trajectory with the U plane of the bottom VDC. A detailed description of the Hall A optics coordinate systems is given in Refs. [86, 105]. The set of tensors D_{jkl}, T_{jkl}, Y_{jkl} and P_{jkl} links the focal plane coordinates to target coordinates and they are further parametrized as polynomials in the position of the particle in the dispersive direction at the focal plane. For example,

$$D_{jkl} = \sum_{i=0}^{m} C_{ijkl}^{D} x_{\rm fp}^{i}. \tag{3.24}$$

The four groups of coefficients C_{ijkl} are usually referred to as the optics matrix elements of HRS, and the calibration of HRS optics involves determination of these elements for accurate reconstruction of δ, $\theta_{\rm tg}$, $y_{\rm tg}$ and $\phi_{\rm tg}$.

3.4.2 Data Set

Experiment E12-07-108 was one of the first two experiments doing measurements with the HRS after replacing the superconducting Q1 with the SOS quad. To achieve good acceptance and resolution with the new magnet, the field strength in the SOS quad was carefully tuned until its field integral was very close to that of the original Q1. This was examined by reconstructing the reaction vertices of electron events scattered

from a multi-foil target with the HRS stock optics matrices during the commissioning of the spectrometer.

In order to precisely determined the optics matrix elements, two calibration data sets were collected at the beginning of Experiment E12-07-108 using a 2.2 GeV electron beam.

- The angular and vertex calibration used the deep inelastic scattering on a 20-cm-long, 9-foil carbon target (Sec. 2.5), with a sieve-slit collimator (Fig. A-1) in front of the spectrometer. The left HRS sat at 42° and the right HRS at 48°. Both spectrometers were set to detect scattered electrons of momentum 1 GeV/c. The deep inelastic scattering process has a larger cross section than other reactions at such a beam energy and can reduce the beam time needed to collect enough data for calibration. The cross section is also nearly constant across the acceptance of the HRS, minimizing the variation in the number of calibration events in different regions of the acceptance. The rasters were kept off during the collection of these data and the position of the electron beam was monitored by the BPMs for each event. As shown in Fig. A-1, the 1-inch-thick sieve slit plate is made of tungsten with holes drilled in a grid pattern. Electrons lost enough energy passing through tungsten, so that only the particle trajectories that went through the sieve holes could reach the detector hut. The set of foil targets and the holes on the sieve slit define the interaction point and actual angle of the trajectory for each event, from which one can deduce the values of the transverse position (y_{tg}) and the vertical (θ_{tg}) and horizontal (ϕ_{tg}) tangent angles in the target coordinate system.

- Electrons elastically scattered from a liquid hydrogen target were used for calibration of momentum reconstruction for HRS. The positions of the two HRSs were the same as those in collecting sieve data. The central momenta of both spectrometers were adjusted so that they were different from the momenta of elastically scattered electrons at that direction by a few percent. This deviation was varied from +4% to -4% in steps of 2%. Such a sweep is referred to

as a delta scan, by which the whole momentum acceptance was covered. The rasters were turned on to prevent potential damage due to the deposited energy of the incoming electrons on the target cell. To be able to calculate the scattered electron momentum, one needed to have good matrices for vertex and angular reconstruction first. The reconstructed vertices were used to correct for the energy loss of the incoming and scattered electrons, which proved crucially important in δ calibration with an extended target. The determination of the scattering angle for each event depended on a good reconstruction of the in-plane angle $\phi_{\rm tg}$.

It was also important that the positions and central angles of the two HRSs during optics calibration runs be well determined. This was achieved by performing a high precision survey to the following quantities:

- the spectrometer central angles,
- the position of the spectrometers relative to the ideal center of the experimental hall, and
- the position of the sieve slit central hole with respect to the spectrometer central axis.

The position of the target ladder during the experiment was monitored by the Hall A target group and found to be shifted 2.2 mm from the hall center towards downstream of the beam line [112].

3.4.3 Optimization Procedure

As described above, the "true" values of the target variables of the events collected in the optics calibration runs can be obtained from survey results or elastic scattering conditions. For example, in the elastic scattering of electrons off a proton target, the scattering momentum can be expressed as

$$E' = \frac{E - \Delta E}{1 + (E - \Delta E)/M_p(1 - \cos(\theta_0 + \phi_{\rm tg}))} - \Delta E', \tag{3.25}$$

where θ_0 is the central angle of the spectrometer, M_p is the proton mass, and E is the energy of the electron beam. ΔE and $\Delta E'$ are the amount of energy lost by the incoming and scattered electron in all the materials along their path, respectively, and are calculated by Eq. 3.31.

The thickness of the sieve slit plate is taken into account when calculating the average position of the electron events passing through a specific sieve hole. Only electrons that are blocked by neither the front nor the back surface of the sieve slit can make their way to the detectors. Thus the effective centroid of the projection of these electron trajectories onto the front surface of the sieve slit will not be at the center of each hole but moved towards the central ray of HRS [62]. To account for this effect, the intercept of the electron trajectories with the plane in the middle of the front and back surfaces of the sieve slit were used when calculating the reference values of $y_{\rm tg}$, $\theta_{\rm tg}$ and $\phi_{\rm tg}$.

The optics matrix elements are obtained by minimizing the aberration functions:

$$\Delta(W) = \sum_{\text{Events}} (W^{\text{recon}} - W^0)^2 = \sum_{\text{Events}} \left(\sum_{ijkl} C^W_{ijkl} x^i_{\rm fp} \theta^j_{\rm fp} y^k_{\rm fp} \phi^l_{\rm fp} - W^0 \right)^2, \tag{3.26}$$

where W can represent any target variables δ, $y_{\rm tg}$, $\theta_{\rm fp}$ or $\phi_{\rm tg}$, and W^0 is the corresponding "true", or reference values calculated from survey results or the elastic condition. The optics optimization program is written in C++ and adapted from the software package written for Experiment E06-010 [113]. It calls the target variable reconstruction subroutine of the `THaVDC` class in the standard Hall A Analyzer [96] and utilizes ROOT's [114] `ROOT::Math::Minimizer` [115] interface to interact with various minimization algorithms, including `Fumili` [116], `GSLMultiFit` [117], and `BFGS` [118], in addition to the well-tested `Migrad` [107] routine.

Starting with an initial optics database obtained by experiments in the 6 GeV era, the calibration program varies the optics matrix parameters to find the global minimum of the aberration function in Eq. 3.26. The angular and vertex parts of the optics matrices were optimized independently, and the momentum part was fitted in the end since the calculation of the reference momentum depends on the reconstruc-

tion of the other three target variables.

3.4.4 Results

Sieve Pattern Reconstruction

The reconstructed sieve pattern after the calibration process is shown in Fig. 3-15. One can easily compare the distribution of events to the design of the sieve slit in Fig. A-1. Two of the sieve holes are larger than the rest to allow identifying the center and orientation of the sieve. The corresponding holes have more statistics than the surrounding holes. It is clear that the acceptance of the spectrometer varies significantly as the reaction vertex moves along the beam line. Electrons scattered from the central foil have a large range in the in-plane and out-of-plane angles, while only a few edge holes are seen for the most upstream and downstream foils.

Multi-foil targets

The deviations of the reconstructed positions of the 9 carbon foils from their nominal positions are all within 0.2 mm. The resolution in vertex was found to be 2 mm at 42° for a 20 cm long target. The result is shown in Fig. 3-16.

Momentum Calibration

The result for delta calibration is shown in Fig. 3-17. The peak of reconstructed momentum is within 1×10^{-4} of the expected value from elastic scattering condition. The width of the momentum distribution is smaller than 1×10^{-3}. However, the intrinsic momentum resolution of HRS is much better than this value. The broadening of the momentum peak is caused by the energy straggling process experienced by the incident and scattered electrons in the LH_2 target.

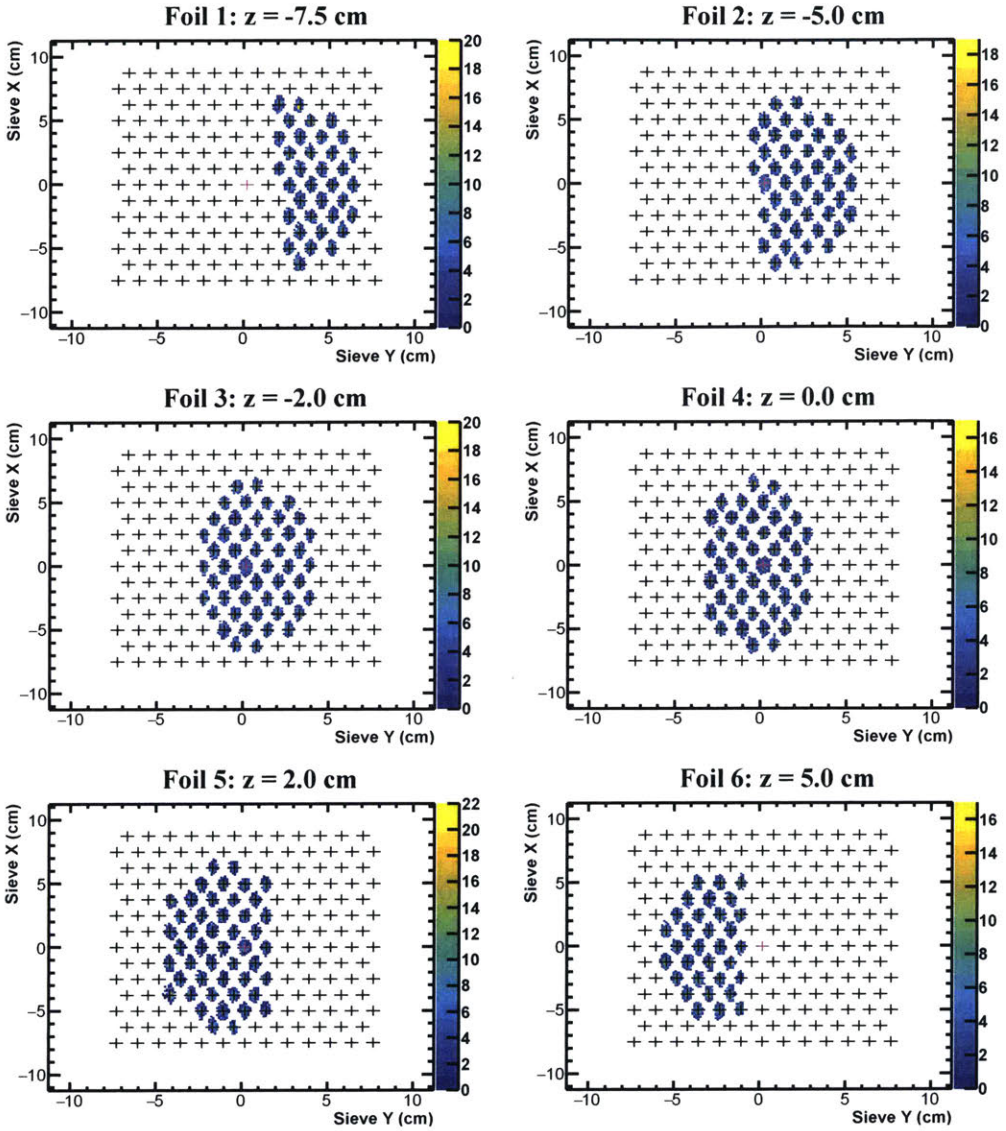

Figure 3-15: Reconstructed sieve pattern after optimization for 6 (out of 9) foils of the carbon targets. The position of each foil is labeled on top of the plot. The crosses mark the sieve hole positions. The magenta crosses correspond to the central sieve hole. The shifting pattern of sieve holes populated by scattering events from different target foils reflect the angular acceptance of HRS.

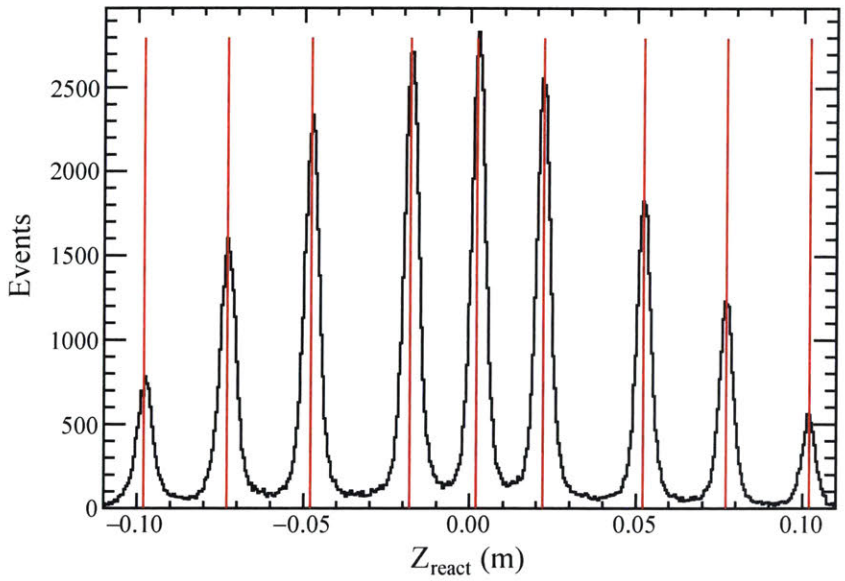

Figure 3-16: Reconstructed reaction vertex for multi-foil targets. The red lines show the nominal positions of the 9 carbon foils.

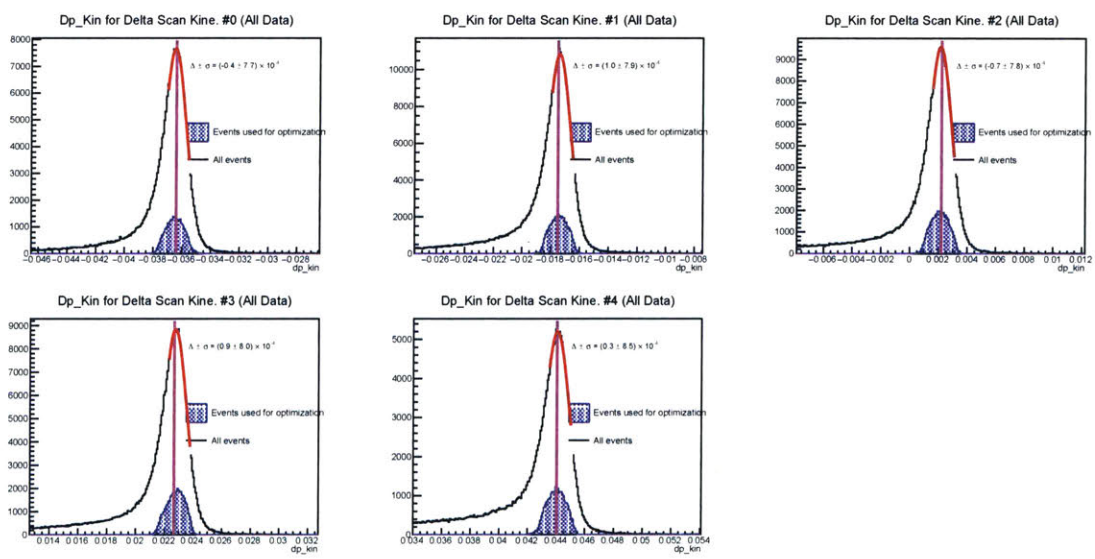

Figure 3-17: The distribution of momentum for delta scan runs after calibration. The shaded histogram shows the elastic events used for optimization procedure. The hollow histogram shows the distribution of all events, including the radiative tail. The red line depicts the elastic scattering momentum.

3.5 Scattering Angle

In order to gain insight about the elastic form factors, it is necessary to normalize the measured elastic cross sections by the Mott cross sections (Eq. 1.25) at the same kinematic settings. An accurate knowledge of the scattering angle is required for that purpose. The absolute scattering angle can be inferred from the spectrometer central angle and the reconstructed in-plane angle, combined with the direction of incoming beam. The beam direction was measured by the two BPMs in the beam line (Sec. 2.4.3) to about 0.03 mrad [67]. The determination of the direction of the spectrometer relative to the beam line is discussed below.

We used two methods to measure the spectrometer central angle. The first method is to perform a survey on the spectrometer position in the experimental hall. This method is believed to be most precise and its result was used in E12-07-108 analysis for kinematics where a survey was indeed carried out. However, the survey process required several hours of beam downtime to accomplish, and thus was not performed at all kinematics during Experiment E12-07-108 to maximize the usable beam time.

The spectrometer position was also monitored and recorded in the data stream by the EPICS system. The EPICS value of the spectrometer angle was calculated from the cross point of a vernier attached to the dipole and the floor marks that designated the 360° direction around the center of the experimental hall in a step of 0.25°. The results of the two approaches agreed within 0.02°. The EPICS spectrometer angles were used for kinematics when no survey results were available.

The accuracy of the HRS angle was tested by checking the spectra of reconstructed invariant mass for elastic scattering. The event reconstruction process is discussed in Sec. 3.6. The reconstructed peak positions of the W spectra for left HRS kinematics are shown in Fig. 3-18. The W peaks scatter around the proton mass, indicating no systematic overall offsets in the determined scattering angle. The error bars in Fig. 3-18 were translated from a 0.2 mrad uncertainty in the scattering angle for the surveyed kinematics and 0.3 mrad for unsurveyed ones. The differences between the proton mass and the reconstructed invariant masses were within 1.5 error bars.

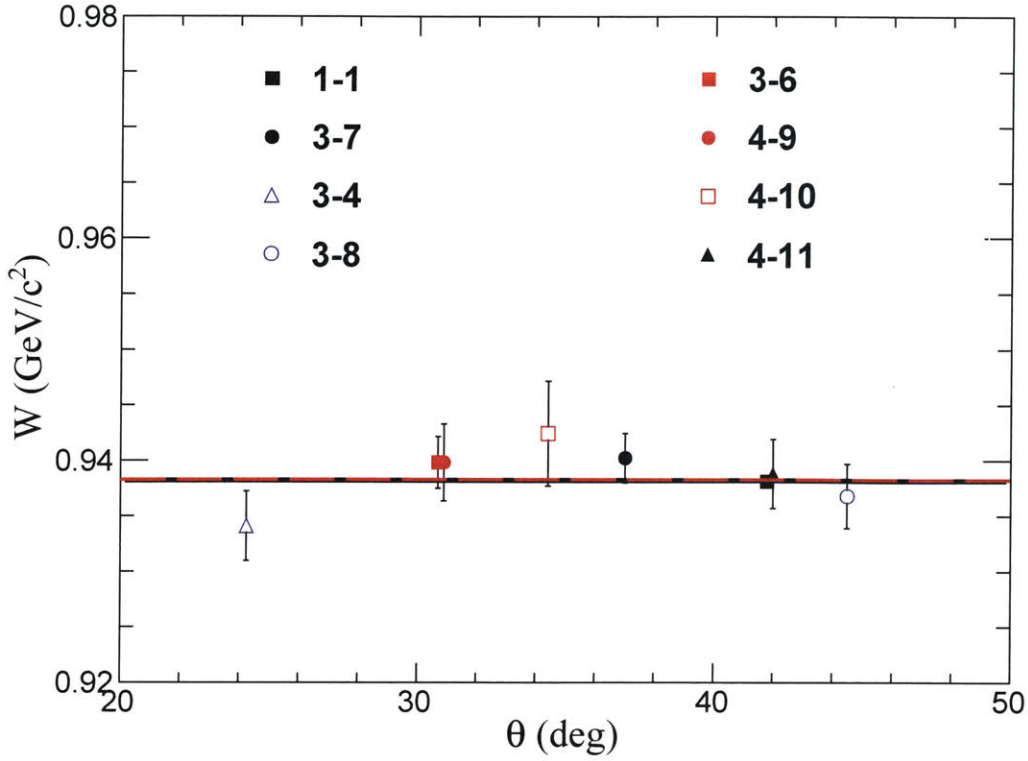

Figure 3-18: Peak positions of reconstructed invariant mass spectra for various left HRS kinematics. The solid (hollow) points represent kinematics where a survey of the HRS position was (not) performed, and their error bars correspond to an uncertainty of 0.2 mrad (0.3 mrad)in the spectrometer angle.

We decided to assign 0.3 mrad to the point-to-point uncertainty and 0.1 mrad to the normalization uncertainty in the scattering angle.

3.6 Event Reconstruction

A common criterion for selection of the elastically scattered electrons is the invariant mass W of the undetected system. The observed W spectrum exhibits a peak at the proton mass along with a long tail towards large W due to bremsstrahlung and inelastic scattering process. The background due to inelastic scattering can be eliminated by only considering events whose W values are below the pion production threshold. Thus the invariant mass is the physics variable of most interest to

E12-07-108 analysis.

3.6.1 Reconstruction Algorithm

The reconstruction of invariant mass is based on the following formula:

$$W = \sqrt{M_{\mathrm{p}}^2 + 2M_{\mathrm{p}}(E - E') - 4EE' \sin^2 \frac{\theta}{2}} \,. \tag{3.27}$$

The E and E' here denote the energies of the incident and scattered electrons respectively and θ is the angle between them. M_{p} is the proton mass.

An offset in the measured invariant mass W can be caused by offsets in the kinematic variables E, E' and θ. From Eq. 3.27, it is straightforward to derive the equations relating these offsets as follows:

$$\frac{\partial W}{\partial E} = \frac{M_{\mathrm{p}}}{W} - \frac{2E' \sin^2 \frac{\theta}{2}}{W} \approx \frac{E'}{E} \,, \tag{3.28}$$

$$\frac{\partial W}{\partial E'} = -\frac{M_{\mathrm{p}}}{W} - \frac{2E \sin^2 \frac{\theta}{2}}{W} \approx -\frac{E}{E'} \,, \tag{3.29}$$

$$\frac{\partial W}{\partial \theta} = -\frac{EE' \sin\theta}{W} \approx -\frac{EE' \sin\theta}{M_{\mathrm{p}}} \,. \tag{3.30}$$

The approximations in Eqs. 3.28, 3.29 and 3.30 are valid for events in the vicinity of elastic peak ($W \approx M_{\mathrm{p}}$).

In the analysis software, the scattering angle was determined for each individual event based on the settings of the spectrometer and the reconstructed in-plane angle ϕ_{tg}. The beam energy E was a fixed value for each kinematic setting which was extracted from the ARC measurement (Sec. 2.4.1). It can be seen from Eq. 3.28 that a 10^{-4} level fluctuation in the beam energy leads to a fluctuation of invariant mass below 1 MeV. Thus it is reasonable to use a constant beam energy when reconstructing W. In contrast, W is very sensitive to E' at large beam energies. The ionization loss of the scattered electrons in the target and other materials at the entrance and exit of the spectrometer is of the order of 2–3 MeV, which can result in a shift in the reconstructed W up to 6–10 MeV depending on the kinematics. Thus it is important

that these effects be taken into account in order to have an accurate W spectrum.

3.6.2 Ionization Loss

Electrons passing through the target material lose energy due to the ionization and excitation of the target atoms. This process leads to corrections in both E and E' in the reconstruction of invariant mass. Two possible ways to estimate the ionization loss exist. The mean energy loss rate (also referred to as stopping power in some literatures) depicts the average energy loss experienced by electrons in a material of unit thickness. The Hall A analysis software uses this quantity for energy loss correction by default [119]. However, for materials of moderate thickness (which is the case for the various materials traversed by electrons in E12-07-108, see Table 3.2 for details), the energy loss probability distribution is described by the highly-skewed Landau-Vavilov distribution [120], the average of which differs from its peak position by a significant amount. Since we are most interested in the peak position of invariant mass, most probable energy loss is more relevant in E12-07-108 analysis. It was also confirmed that corrections using most probable energy loss resulted in a more consistent peak position of the W spectra for various kinematics than does the mean stopping power.

The most probable energy loss in a material of density ρ (g/cm^3) and thickness t (g/cm^2) experienced by ultra-relativistic electrons can be calculated by [120, 121]

$$\begin{aligned}\Delta E_{\mathrm{MP}} &= \frac{2\pi\alpha^2(\hbar c)^2 N_A}{m_e c^2}\Big(\frac{Z}{M_A}\Big)t\Big[\ln\Big(\frac{\alpha m_e c^2}{\hbar c}\frac{t}{\rho}\Big)+0.198\Big] \\ &= 0.15354\Big(\frac{Z}{M_A}\Big)t\Big[\ln\Big(1.8897\times 10^8\frac{t}{\rho}\Big)+0.198\Big], \qquad (3.31)\end{aligned}$$

where N_A is Avogadro's constant, and M_A is the atomic mass of the nucleus. The resulting energy loss ΔE_{MP} is given in MeV. For a specific event, the reaction vertex is first reconstructed from the directions of the beam (determined by the driving currents in the rasters) and scattered electron. After that, the pathlength of the particles in various materials can be calculated. Finally the most probable energy

Table 3.2: The thicknesses of the materials at the target area and at the entrance of the spectrometer.

Name	Material	Density (g/cm^2)	Thickness (cm)
Beam Entrance	Al 7075	2.80	1.75×10^{-2}
Cell Wall	Al 7075	2.80	1.8×10^{-2}
Endcap	Al 7075	2.80	1.1×10^{-2}
Liquid H_2	Hydrogen	7.23×10^{-2}	15
Scattering Chamber	Aluminum	2.80	4.06×10^{-2}
LHRS Air	Air	1.20×10^{-3}	38.68
RHRS Air	Air	1.20×10^{-3}	37.57
Spectrometer entrance	Kapton	1.42	3.05×10^{-2}

loss can be estimated based on these pathlengths and the densities of the materials (Table 3.2). The result is illustrated in Fig. 3-19. The energy loss is then subtracted from the nominal beam energy for the incident electrons and added to the measured momentum for the scattered electrons, from which the energy-loss corrected invariant mass can be extracted. Fig. 3-20 illustrates that corrections for ionization loss brings the peak of the W spectrum close to the proton mass.

3.6.3 Extended Target Correction

In the HRS optics formalism (Sec. 3.4), the four target variables $y_{\rm tg}$, $\theta_{\rm tg}$, $\phi_{\rm tg}$ and δ are related by polynomials to the four track variables at the focal plane: $x_{\rm fp}$, $y_{\rm fp}$, $\theta_{\rm fp}$ and $\phi_{\rm fp}$. The particle position at the target side in the dispersive direction—$x_{\rm tg}$—is implicitly assumed to be zero (otherwise it is not possible to reconstruct five target variables from only four observables.). When the spectrometer is at an angle different than 90° and the target has a finite length, the optics matrices only produce a zeroth order approximation to the actual trajectory at the target. A first order correction linear to the vertical beam position can be applied to improve the reconstruction result. As it turns out, this correction is of the order of 2×10^{-4}/mm for δ and 6×10^{-4}/mm for $\theta_{\rm tg}$, and it is negligible for non-dispersive track parameters.

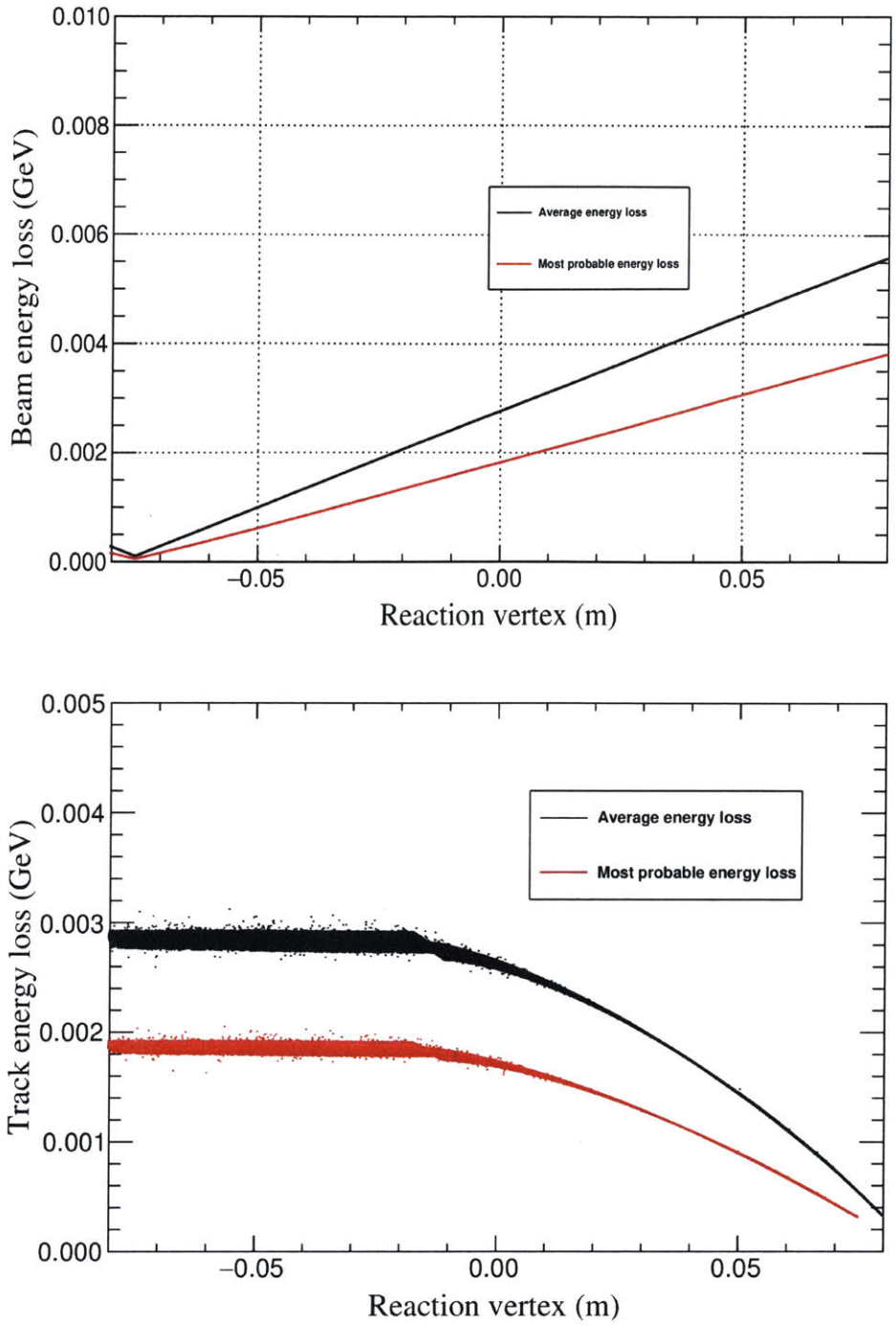

Figure 3-19: The mean (black) and most probable (red) energy loss of the incident (top) and scattered (bottom) electrons as a function of the reconstructed reaction vertex. The difference between the two calculations can be up to 1 MeV, which leads to visible impact on the position of the W peak. The most probable energy loss is used in E12-07-108 analysis.

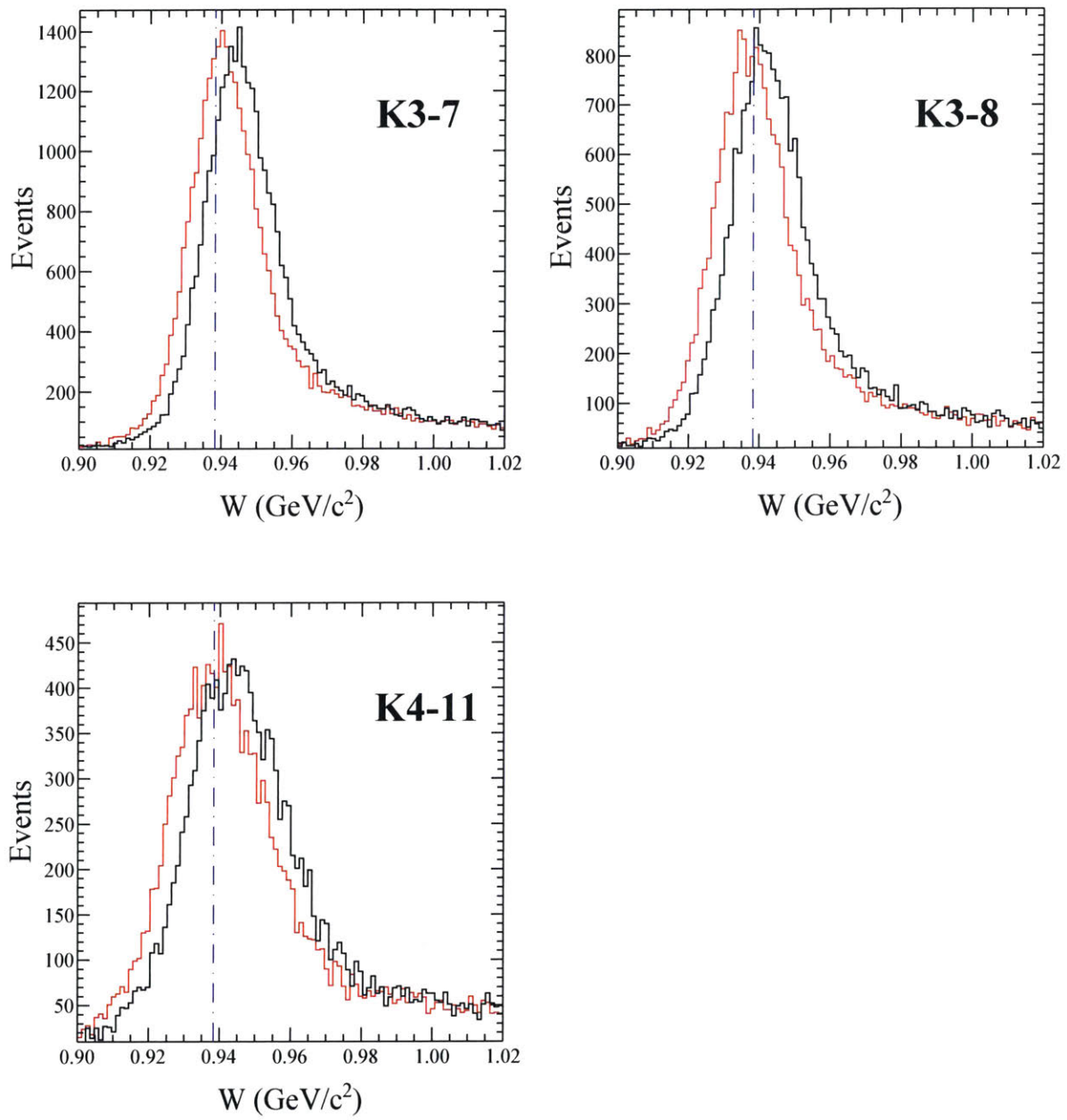

Figure 3-20: The W spectra for the kinematics with magnets of standard tune. The red (black) histogram is after (before) applying the energy loss correction. The blue line indicates the proton mass.

3.6.4 Saturation of SOS magnet

After correcting for the effects of energy straggling and extended target, the invariant mass spectra peaked at the value of the proton mass for all kinematics (Fig. 3-18), and no systematic discrepancy was observed. However, for the kinematics where the field in the SOS quad did not scale with its driving current due to saturation, the transport property of the spectrometer is different from where the optics calibration was performed (Table 3.1). If the optics matrices for standard magnet tune was used for replaying data collected for these kinematics, a broadened and distorted W spectra was obtained (Fig. 3-21).

No calibration data were collected specifically to study the magnet saturation effect during E12-07-108 due to the lack of beam time. Thus we had to use Monte Carlo simulation results to help understand the impacts, and sought a procedure to correct the reconstructed target variables when field saturations took place.

The COSY [98] simulation package was used in this procedure. The input file to COSY contains the geometries, positions and field settings of a series of magnets used in a spectrometer. Fringe field effects are also incorporated. A polynomial is then generated to depict the transportation of charged particles in each magnet element, and their combination determines the mapping from the trajectories at the target side to the track at the detector package. A reconstruction matrix is obtained by performing polynomial fits of the target variables to the track parameters at the focal plane.

An input file corresponding to the nominal tune of HRS was first used to produce the forward and backward matrices. In the next step, the magnetic field strength in the saturated SOS quad needs to be known for relevant kinematics. The readback value from the Hall probe is not accurate due to a pick up of the field from a nearby high current cable (see Sec. 3.2.2 for a complete discussion). The data collected on an aluminum dummy target was used to estimate the actual field reduction in SOS. This target consists of two endcap foils separated by 15 cm. The same magnetic settings as those for LH_2 target were used in these runs to study the contamination

Table 3.3: Reduction of SOS field strength at high HRS set momenta. A relative field strength value of 1 means no saturation in the magnet. For comparison, the results deducted from Hall probe measurements are also listed here.

Kinematics	Set Momentum (GeV/c)	Relative Field Strength	Hall Probe
K4-10	3.259	0.973	0.983
K4-9	3.685	0.948	0.957
K3-6	3.224	0.976	0.985
K3-4	3.962	0.927	0.935

of quasi-elastic scattering events from the aluminum endcaps of the LH_2 target cell.

The z vs $\phi_{\rm tg}$ spectra were then made for both upstream and downstream foils. Some dependence of z as a function of $\phi_{\rm tg}$ was seen due to the fact that the optics matrices obtained from low spectrometer set momentum (i.e., low drive current in SOS) were not directly applicable to the kinematics with set momentum larger than 3 GeV/c. The field settings in the simulation were then adjusted until the same amount of dependence was observed. See Ref. [122] for a complete description of the procedure. The correction factors to the field strength thus extracted are summarized in Table 3.3.

The field setting of the standard tune, multiplied by the factors in the third column of Table 3.3, was then used in the COSY input file to generate the corresponding forward and backward matrices. The differences between this "corrected" reconstruction matrices and those for the standard tune were then extracted and applied to the matrices that were used to replay raw data. The improvement in the W spectra is shown in Fig. 3-21. A complete discussion can be found in Ref. [123].

3.7 Event Selection

The selection of elastically scattered electron events incorporates multiple components which are discussed in this section.

- **Trigger type:** The main trigger used in the analysis is T1 (Sec. 2.8.3). A

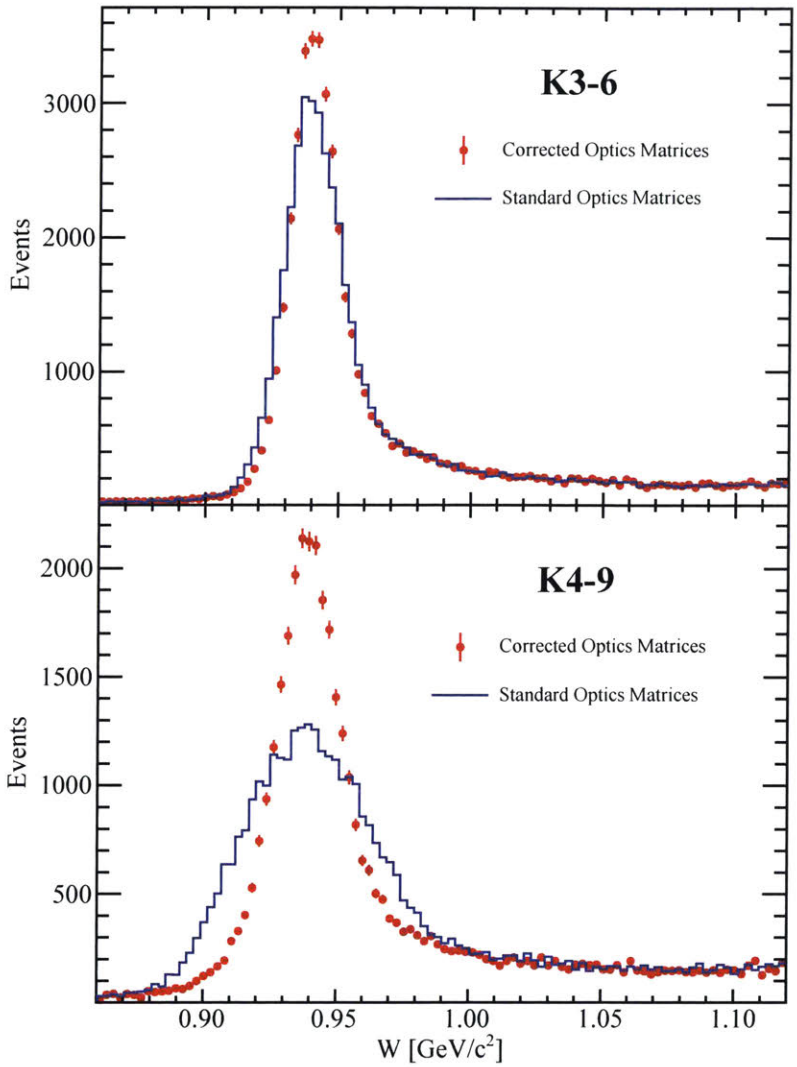

Figure 3-21: Corrections to the optics reconstruction matrices due to saturation of SOS magnetic field at large set momentum. The blue histograms show the reconstructed W spectra when using the standard optics matrices obtained by optics calibration described in Sec. 3.4. The red points are generated with the corrected optics matrices. See text for more details.

good event has to fire the two scintillator planes so that the lowest bit of the hexadecimal trigger type is set.

- **VDC single cluster cut:** It is required that a single cluster exist in each of the four VDC readout planes for an event to be considered in the analysis. This criterion eliminates the potential problematic tracks due to ambiguous cluster associations in track formation (see Refs. [67, 124]. Also see Sec. 3.8.1 for more discussion about the motivation of this cut). The fraction of events excluded by the single cluster cut is corrected by the VDC reconstruction efficiency (Sec. 3.8.1).

- **Large Cherenkov signal:** The sum of the 10 Cherenkov ADCs is required to be above 300 channels, which corresponds to 3 photo-electrons.

- **Large energy deposition in calorimeter:** The energy deposition in the shower detectors (RHRS) or pion rejectors (LHRS) is normalized by the track momentum and the ratio needs to be above 0.6 for LHRS and larger than 0.8 for RHRS to be considered an electron event. In addition, the normalized energy deposition in the first layer of calorimeter should not be less than 0.1.

- **Fiducial cuts:** A fiducial region is defined to exclude events where at least one of the target variables is not reconstructed in a reasonable range. The definitions are as follows:

$$-0.04 < \phi_{\rm tg} < 0.04,$$
$$-0.08 < \theta_{\rm tg} < 0.08,$$
$$-0.1 \cdot |\sin\theta_0| < y_{\rm tg}\ ({\rm m}) < 0.1 \cdot |\sin\theta_0|,$$

  where θ_0 is the angle between the beam line and the spectrometer central ray.

- **β cut:** Only those particles whose reconstructed velocity is larger than 0.2 are included in the analysis. This cut helps exclude cosmic contamination.

- **Momentum acceptance:** Only the events satisfying $-0.035 < \delta < 0.035$ were considered in the analysis. Outside this range, the acceptance of the spectrometer becomes sensitive to the position of various apertures and the simulation package might not model the acceptance very well.

- **Elastic cut:** It is also necessary to exclude background events from inelastic scattering. This is achieved by requiring $0.86 < W < 1.05$ (GeV/c^2) so that events beyond the pion production threshold are not included.

3.8 Efficiency Studies

The efficiencies of the cuts introduced in Sec. 3.7 for selecting electrons are studied in this section. They will be used for normalizing the W spectra to compare with simulation results.

3.8.1 VDC Reconstruction Efficiency

The VDC reconstruction efficiency is defined as the fraction of elastic electron events that results in successful track formation, which in E12-07-108 analysis means one single cluster reconstructed in each of the four VDC planes. This efficiency measures the loss of good events due to the single cluster cut in VDCs.

In order to determine the efficiency, we first selected a sample of good electron events. Only events of trigger 1[2] were considered and they had to have large signals in the Cherenkov and shower detectors. It is also worth pointing out that no fiducial cuts were incorporated since that would require that the value of target variables exist, meaning at least one track had to be formed for these particles, thus artificially throwing out zero-track events. For the same reason, the energy deposition in the shower detectors was normalized by the HRS set momentum instead of the track momentum for this analysis.

Due to the small elastic e-p cross sections at large Q^2 and low beam current during

[2]The coincidence of S0 and S2m signals. See Sec. 2.8.3 for more details.

data taking parallel to Experiment E12-06-114, each production run only accumulated tens of electron events or less in some kinematics, making a run-by-run calculation and correction of the efficiency unreliable. Thus one VDC efficiency value is extracted for individual kinematics by combining the statistics collected in all the runs.

The low event rate for large Q^2 settings also brought the problem of cosmic contamination in the sample for evaluating the VDC efficiency. The T1 trigger in E12-07-108 only requires a coincidence between the S0 paddle and one of the S2 paddles. During E12-07-108 commissioning, it was seen that cosmic ray events can fire the T1 trigger at a raw rate of 4–5 Hz. The majority of these backgrounds were killed by the particle identification cuts. However, a small portion could survive and be included in the VDC efficiency analysis. Cosmic rays usually come at wild angles towards the VDC and can lead to much lower reconstruction efficiency than do the scattered particles. Due to the low rate of elastically scattered electrons, this contamination could significantly bias the evaluation of VDC efficiency.

One effective way to eliminate cosmic events is by employing a TOF cut. Cosmic rays come to the detectors in the opposite direction to that of scattering events, leading to a negative TOF measured by the scintillators hodoscope. This is illustrated by Fig. 3-22. All the events shown there passed the PID cuts, yet a significant portion were cosmic events and resulted in a TOF peak around -5 ns. Thus a TOF cut at 2 ns was applied to select electron events resulting from scattering at the target.

The VDC efficiency was evaluated as

$$\eta_{\mathrm{VDC}} = \frac{\text{Number of one-cluster events in the sample}}{\text{Number of all events in the sample}}. \tag{3.32}$$

The result is summarized in Table 3.4.

Events with Multiple Clusters in VDCs

In this section we briefly discuss the reason that the single cluster cut is requested for good tracking events. The design of the VDCs as a pair of chambers, each composed of two wire planes oriented at 90° to one another, allows a simple analysis algorithm

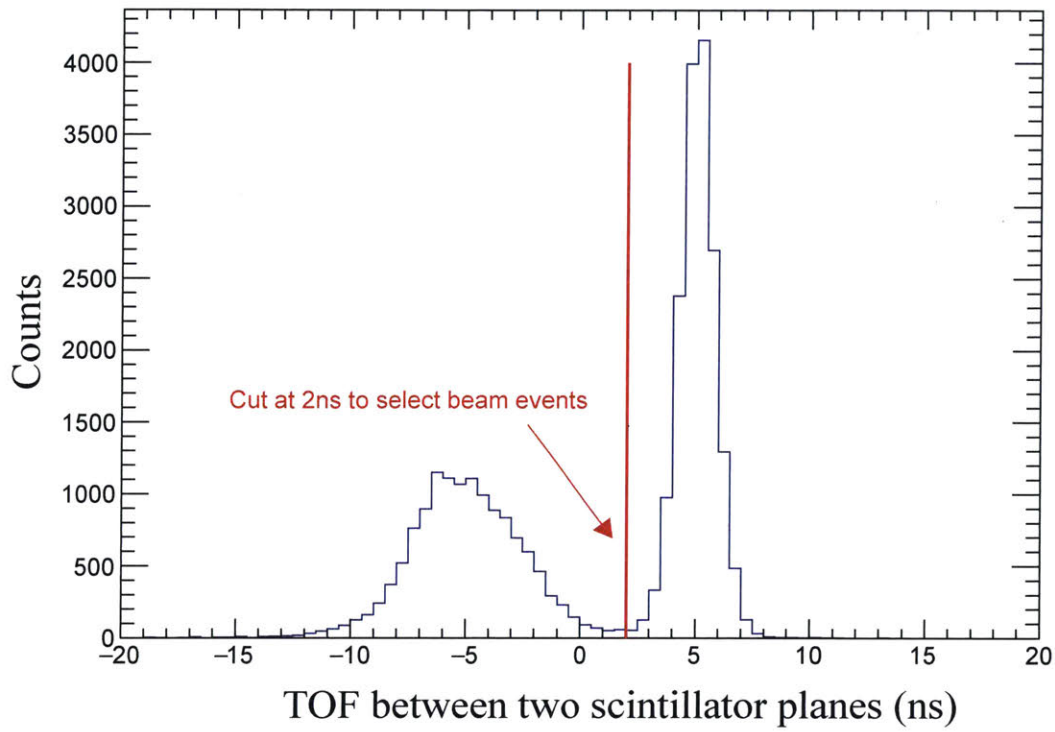

Figure 3-22: The reconstructed time-of-flight spectrum for kinematics K5-16. Events in this spectrum already passed the PID and trigger type cuts. The sharp peak at 5 ns corresponds to electrons scattered off the liquid hydrogen target; the broad peak at -5 ns corresponds to cosmic rays. Cosmic events hit S2m first and then S0, hence their time-of-flight is negative. Requiring a time-of-flight larger than 2 ns removes these backgrounds.

Table 3.4: VDC reconstruction efficiencies for E12-07-108 kinematics. The point-to-point systematic uncertainty in η_{VDC} is estimated to be 0.4% and the normalization uncertainty is about 0.5%.

Kinematics	Spectrometer	η_{VDC}	$\Delta\eta_{\mathrm{VDC}}$
K4-9	LHRS	0.8784	5.6×10^{-3}
K3-6	LHRS	0.8893	5.7×10^{-3}
K3-7	LHRS	0.8999	5.8×10^{-3}
K3-9	RHRS	0.9189	5.9×10^{-3}
K4-13(II)	RHRS	0.9182	5.9×10^{-3}
K5-16	RHRS	0.9163	5.9×10^{-3}
K1-2	RHRS	0.9244	5.9×10^{-3}

for precision measurement of single tracks. Here single tracks refer to those resulting in one single cluster in each of the four wire planes. For these events, the global tracks are determined from the two track cross-over positions measured in the two VDCs. The reconstruction of the cross-over coordinate in one VDC plane for a single track is illustrated in the top figure of Fig. 3-23.

When there are more than one cluster in at least one of the two readout planes, ambiguities arise in combining the U and V clusters to form a traversing position of the charged particle. This is illustrated by the bottom figure of Fig. 3-23.

As previously illustrated, the difficulty in finding the traversing point in a VDC chamber in the presence of multiple clusters lies in the hardware design of the tracking system in Hall A. With only two readout coordinates and two drift chambers, it could be very difficult to resolve the ambiguity in pairing the U and V wires by resorting to some algorithm tricks. A thorough code review of the analysis software in late 2013 revealed several bugs in the Release 1.5 of the Hall A analyzer when handling multi-cluster VDC events, which dictates such events be rejected in any analysis using the software. A complete description of the HRS tracking algorithm and the existing bugs can be found in Ref. [124]. The following is a summary of the effects of the defects in the tracking algorithm on the track reconstruction results:

- For (1, 1; 1, 1) cluster occupancy (each readout plane has only one cluster), the correct track is reconstructed.

- For (2, 1; 1, 1), (3, 1; 1, 1) and similar cluster occupancies, multiple clusters are present in one of the four readout planes, and the correct track is most likely found.

- For (2, 2; 1, 1) and similar, only one track is found by the current tracking algorithm, but there is a large probability of picking the wrong cluster combination, and hence resulting in bad reconstruction.

- For (2, 2; 2, 1), (2, 2; 2, 2) and higher cluster multiplicities, the probability of finding ghost track increases quickly and the reconstruction result becomes increasingly unreliable.

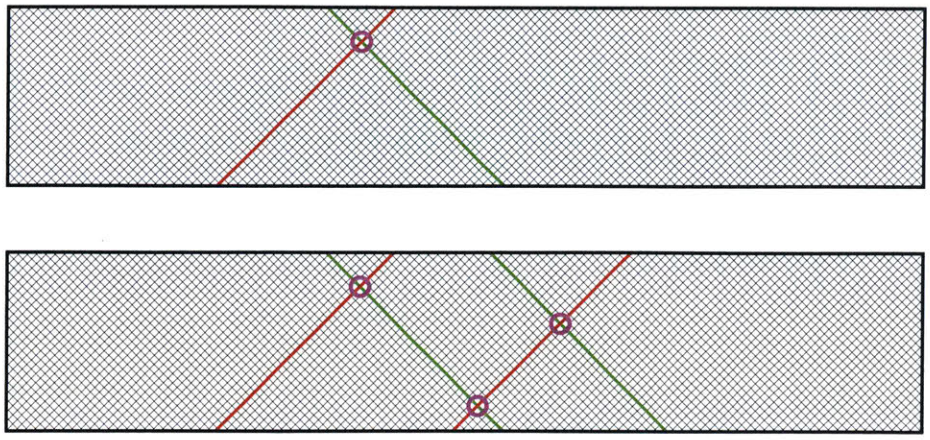

Figure 3-23: Illustration of the reconstruction of cross-over coordinates in a VDC chamber, when a single cluster is present in the U and V plane (top) and when multiple clusters are present in the U an V plane (bottom). The red and green lines represent the group of U and V wires fired in one event, and the magenta circles represent the (potential) reconstructed cluster positions.

Based on previous discussion, the trajectory of the charged particle can only be unambiguously determined for events with a single cluster in each of the four readout plane, and only for these events can the target variables (y_{tg}, ϕ_{tg}, θ_{tg} and δ) and kinematic variables (the invariant mass W) be reliably reconstructed.

Uncertainties in VDC Reconstruction Efficiency

The fraction of multi-cluster events in the observed electron sample is around 10%, so the knowledge of the uncertainty of such a large correction is of crucial importance to achieve the required precision in the extracted cross sections. The straw chamber in the HRS detector stack was used for studying this uncertainty.

The straw chamber effectively provides a third readout plane for the HRS tracking system. It is especially useful in identifying the tracks for such multi-cluster events that only one of the two VDCs has more than one cluster and there is exactly one cluster in the straw chamber. In this case, one can bypass the VDC with multiple clusters and only use the other two track planes to find the track parameters.

It is necessary to identify the hit clusters in the set of U (V) planes of the straw chamber before using it to form a track. One cluster consists of adjacent straws in

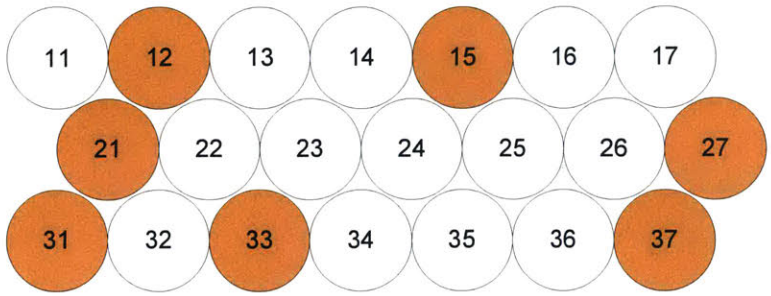

Figure 3-24: Illustration of the procedure to find clusters in a straw chamber. The three layers represent the three planes, and the circles are the cross sections of the straws. The filled circles represent the fired straws. The software will find a total of four clusters for this hit pattern: ($S12 \rightarrow S21 \rightarrow S31$), ($S12 \rightarrow S22 \rightarrow S33$), ($S15$), and ($S27 \rightarrow S37$).

the three wire planes. Due to the design of the straw chamber, at most one straw is fired by a charged particle in a wire plane. Thus it is also required that none of the straws in the same cluster belong to the same plane. It is also noted that a fired straw in the first and third plane, respectively, with no fired straws in the second plane, can also form a cluster, as long as one can find a straw in the second plane that, if fired, would make the cluster with the two straws. This criterion takes into account the fact that not every straw has high efficiency due to the aging of the hardware. Fig. 3-24 illustrates the procedure to find clusters in a straw chamber.

The second step in tracking with straw chamber is to identify the position of the cluster. It can be difficult to determine whether a track passed to the left or right of a straw. A traditional approach would be to fit to all possible combinations of straw position $\pm$ drift distance and pick the one resulting in the smallest χ^2. It is impossible to carry out the same procedure because the limited number of straw planes and their non-negligible inefficiencies lead to a lack of redundancy of coordinate measurements in the U or V direction. In addition, these fired straws are very close to each other. Fitting these hits can lead to very inaccurate track reconstruction due to the short lever arm.

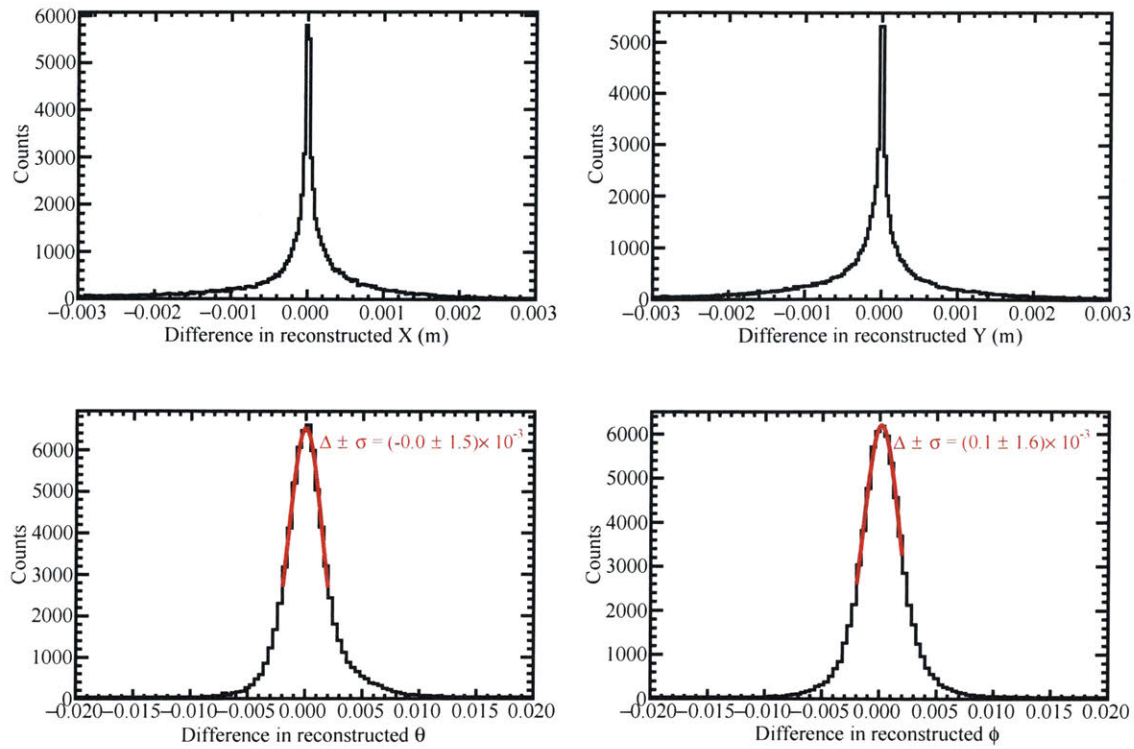

Figure 3-25: Examination of the differences between the VDC tracks and the VDC-straw-chamber tracks for single-cluster events to quantize the precision of the procedure depicted in the text for reconstruction of multi-cluster events. The track parameters shown here are in the TRANSPORT coordinate system.

For the purpose of reconstructing the multi-cluster events using the straw chamber and one of the two VDCs, we decided to use only the positions of the fired straw without considering the drift distance information. The accuracy of this procedure is tested with the "golden" events, which are those passing the VDC single-cluster cut. We first reconstructed the track parameters with VDCs only. Since there is no ambiguity in cluster matching for such events, the resulting track is supposed to be reliable. Then we used the cluster information in one of the two VDCs along with the cluster found in the straw chamber and performed a linear fit to form a second track. The differences in the track parameters between these two tracks are shown in Fig. 3-25.

Using the straw chamber, we analyzed the multi-cluster events where more than

one cluster is present in one of the two VDCs. We also required that a single cluster is identified in both the U and V planes of the straw chamber. The track parameters of such events are then reconstructed with the positions of the single clusters in the VDC and straw chamber. The scattering angle and particle momentum at the target can then be calculated by applying the HRS optics matrices to the track parameters in the TRANSPORT coordinates. In addition to the single-cluster events that are reconstructed by the VDCs alone, a significant amount (about 50%) of multi-cluster events are analyzed with the combined information in the VDC and straw chamber, boosting the overall reconstruction efficiency to about $\eta_{\mathrm{VDC-SC}} \approx 0.95$.

For each kinematics, we selected a sample of electron events. We first counted the number of single-cluster elastic electron events N_1 in this sample and calculated the tracking-efficiency corrected elastic yield:

$$N_{1c} = \frac{N_1}{\eta_{\mathrm{VDC}}}. \tag{3.33}$$

We then used the straw chamber to reconstruct the tracks for those multi-cluster events satisfying the aforementioned conditions. The total number of elastic events in this case was found to be N_1' and the corrected yield was

$$N_{1c}' = \frac{N_{1c}}{\eta_{\mathrm{VDC-SC}}}. \tag{3.34}$$

The corrected elastic yields N_{1c} and N_{1c}' from the two approaches agreed to better than 0.5%, and this is the value assigned to the systematic uncertainty of the VDC reconstruction efficiency.

3.8.2 PID efficiencies

The CO_2 Gas Cherenkov counter and lead glass calorimeter are two types of PID detectors in the HRS. The combination of the two are used to select electron events and suppress hadrons. Since their PID performance is independent, we can use one detector to select an electron sample and study the fraction of events that survive

Table 3.5: PID efficiencies for E12-07-108 kinematics. The uncertainties in the PID efficiencies are estimated to be below 0.2%.

Kinematics	Spectrometer	$\eta_{\rm cer}$	$\eta_{\rm cal}$	$\eta_{\rm PID}$
K4-9	LHRS	0.9998	0.9956	0.9954
K3-6	LHRS	0.9999	0.9958	0.9957
K3-7	LHRS	0.9997	0.9958	0.9955
K3-9	RHRS	0.9985	0.9773	0.9758
K4-13(II)	RHRS	0.9960	0.9728	0.9689
K5-16	RHRS	0.9936	0.9761	0.9699
K1-2	RHRS	0.9998	0.9859	0.9857

the PID cut of the other. The total efficiency is then the product of the individual detector efficiency:

$$\eta_{\rm PID} = \eta_{\rm cer} \times \eta_{\rm cal}. \tag{3.35}$$

The result is summarized in Table 3.5.

The Cherenkov efficiency is very close to 1 on both HRSs. This is due to the fact that the average number of photo-electrons detected in the Cherenkov counter is close to 20 and we only request more than 3 photo-electrons. The calorimeter efficiency is higher on the left HRS since its cut value for fraction energy deposition is 0.6, much lower than the value of 0.8 used on the right HRS, which has a much larger total radiation length.

3.9 Incident Charge

The accumulated beam charge on the LH_2 target was monitored by two beam current monitors in the beam line (Sec. 2.4.2). Each BCM had three different readouts, which were sent to scalers to record the total number of produced pulses. In the working current range of each readout system, the frequency of the digital pulses f_{BCM} coming from the BCM circuits was a linear function of the instantaneous beam current I_{beam}:

$$I_{beam} = a \cdot f_{BCM} + b. \tag{3.36}$$

Thus the total incident charge can be measured by the accumulated pulse counts. One new digital readout system was added to each BCM receiver and was supposed to provide linear output over the entire current range that the CEBAF accelerator can provide.

Several dedicated BCM calibration runs were taken to determine the coefficients a and b in Eq. 3.36. During the collection of calibration data, the responses of BCM readouts to beam currents ranging from 3 µA all the way up to about 75 µA were measured against the outputs from the Unser monitor. The beam was kept stable at each current value for a few minutes to accumulate enough counts to determine the average pulse rate. Before changing the current to the next desired value, the beam was first stopped for a short while. This procedure enabled one to measure the effect of drifts in the Unser output and minimize its influence on the calibration results.

Due to inappropriate tuning of the new digital receivers, their outputs were found to saturate when the beam currents were larger than 35 µA, so it was decided not to use these new readout system for E12-07-108 analysis. The old analog receivers have a long history of reliability and were carefully calibrated in an offline analysis. The calibration showed that the u1 readout was suitable for measurements of current above 10 µA and was used to determine the incident charge for runs with an average current above 15 µA (E12-07-108 dedicated kinematics in Table 2.1), while the charge for the runs below 10 µA was measured by d3.

The drifts in the calibration constants were found to be negligible by comparing the results from multiple measurements. The point-to-point uncertainty in the measured currents was estimated to be about 0.06 µA by looking at the distributions of the fit residuals in the calibration runs. The 0.1 µA normalization uncertainty was mostly due to the precision in the Unser calibration. Detailed information on the calibration of BCMs for Experiment E12-07-108 can be found in Ref. [125].

3.10 Live Time

The DAQ system is unable to record every single particle firing the trigger system. This effect is due to both electronic and computer dead time and must be corrected for during cross section calculation.

3.10.1 Electronic Dead Time

The electronic dead time comes from the processing time of various electronic components on the current input and the finite width of the output pulse. When an event causes a trigger, a logic gate is activated and kept for a finite time period τ. Other particles firing the trigger detectors within this time interval are not detected as separate particles. The corrections due to electronic dead time can be expressed in terms of the width of trigger signal τ and the event rate R. It is known that the number of scattering events in a time interval obeys the Poisson distribution. For every generated trigger pulse, the average number of ignored triggers is $R\tau$, thus the electronic live time can be calculated as

$$ELT = \frac{N_{\text{Measured}}}{N_{\text{Total}}} = \frac{1}{1 + R\tau}. \tag{3.37}$$

The correction factor $1/ELT$ is a linear function of the pulse width, so one way to correct for the electronic dead time is by feeding pulses of various width to the electronics and measuring the dependence of trigger rates on the pulse widths. A linear extrapolation of these rates to 0 ns then yields the ideal trigger rate with no electronic dead time. However, this was not implemented in E12-07-108 setup.

In Experiment E12-07-108, we used Eq. 3.37 to directly estimate the electronic live time. The trigger signals are generated from the MLU module and are of a fixed width. The width can be determined by the spectrum of time intervals between two consecutive hits in the TDC channel of the main trigger. It was found that τ equals 40 ns [126]. The corresponding electronic dead time is much less than 0.01% and can be safely ignored due to the low event rate for E12-07-108.

3.10.2 Computer Dead Time

The computer dead time needs to be measured to account for the portion of the time that the DAQ system is busy digitizing and recording the current event and unable to process new events. If the triggers are not prescaled, the incoming events follow a Poisson distribution and the dead time can be theoretically calculated just like in the case of electronic dead time. In a typical experiment, multiple triggers are used simultaneously and they can be prescaled by distinct factors, which makes direct calculations very difficult.

A measurement of computer dead time was performed using scalers. A copy of each trigger signal was sent to a scaler during E12-07-108 to count the total number of incoming pulses. An L1A signal was generated by the trigger supervisor whenever a trigger came in while the DAQ system was not occupied. The L1A signal lasted until the current event was fully processed. The L1A signal was also converted to a shorter pulse and sent to a scaler. In addition, the pattern of the fired trigger channels was recorded to help identify which triggers were present in a particular event. By knowing the total number of events $N_{\mathrm{T1,total}}$ recorded by the scaler, the number of trigger 1 events $N_{\mathrm{T1,DAQ}}$ in the data file, and its prescale factor PS_1, the correction due to computer dead time can be calculated as

$$CLT = \frac{\mathrm{PS}_1 \cdot N_{\mathrm{T1,DAQ}}}{N_{\mathrm{T1,total}}}. \tag{3.38}$$

The computer live time during Experiment E12-07-108 is typically larger than 0.98, except for the kinematics taken at very low Q^2 (e.g., K1-1 and K1-2), where up to 7% of the scattering events were not recorded by the trigger supervisor due to the computer dead time. A table of the computer live time for various kinematics can be found in Ref. [126].

3.11 Target Boiling Correction

The electron beam deposits energy in the target area which can cause the liquid hydrogen to boil and lead to local density reduction. In order to study the boiling effect, deeply inelastic scattering data were collected on LH_2 target with beam currents ranging from 3 to 60 µA. Another run with aluminum dummy target at a current of 40 µA was taken to estimate the contribution from endcaps. The number of good electron events in each run, corrected by VDC efficiency and live time and normalized by the accumulated charge, was then plotted as a function of the average beam current. The normalized yield exhibited a linearly decreasing tendency, which indicated that the target density ρ can be parameterized as a function of the current I as

$$\rho(I) = \rho_0(1.0 - aI), \tag{3.39}$$

where ρ_0 is the target density at zero current and a characterizes the rate at which the density decreases. Additional data were also taken on a carbon foil target for currents up to 75 µA. The normalized yield on carbon target was expected to exhibit no dependence on the beam current. Thus they were used for checking any systematics in this study and as a benchmark for LH_2 boiling results. For LH_2 data, the slope was found to be $a = (0.63 \pm 0.53) \times 10^{-4}$ µA$^-$1. The carbon data yielded a value of $(0.08 \pm 0.58) \times 10^{-4}$ µA$^-$1, consistent with zero.

The boiling correction factor was also extracted by a second approach, where the normalized T_1 scaler counts were calculated for each current setting. It is worth mentioning that the other two enabled triggers in these runs—T_2 and T_3—were not suitable for this study. They both incorporate the Cherenkov detector, which had a very high raw rate even at a relatively low current and hence led to an accidental rate that is proportional to the square of beam current. The advantage of scaler analysis is that no efficiency corrections are required. In addition, the accumulated scaler counts also provided sufficient statistics. The extracted slope for carbon data is again consistent with zero, while for liquid hydrogen target it was found to be $a = (2.23 \pm 0.41) \times 10^{-4}$ µA^{-1}.

To make use of the results from both approaches, we take the correction factor as their average, and assign an uncertainty to reflect the discrepancy, namely $a = (1.43 \pm 0.80) \times 10^{-4}\ \mu\text{A}^{-1}$.

Chapter 4

Extraction of Cross Sections

In this chapter the simulation tools for E12-07-108 are introduced, and the procedures to extract the elastic e-p cross sections based on the ratios of normalized yields in observed and simulated spectra are discussed. Analysis of systematic uncertainties is presented in Sec. 4.6.

4.1 Simulation Software

The simulation toolkit for E12-07-108 includes two pieces of software: SIMC [127] and COSY [98]. Their combination produces expected spectra of various physics variables by random sampling and are compared with the actual yield in the collected data.

The standard Hall C Monte Carlo program (SIMC) is used to simulate elastic scattering events. It was adapted from an $(e, e'p)$ simulation program used for the SLAC experiment NE18. The core components of SIMC include a realistic model of the two Hall A HRSs and a physics event generator. The e-p elastic scattering events are generated following the steps described below:

Incident particles The energies of incident particles are determined by sampling around the ARC measurement results and the range of sampling reflects a realistic estimate of the spread in the set energy (5.0×10^{-4}). In addition, a loss in the energy is employed by sampling from the Landau-Vavilov distribution based on the pathlength in the endcap and target material.

Vertices The vertices of scattering events are generated based on the raster size and target geometry.

Scattering kinematics The directions of scattered electrons are generated by uniformly sampling θ_{tg} and ϕ_{tg} in a range large enough to cover the whole HRS acceptance. The scattering angle is then calculated based on Eq. 3.18. The momentum of the outgoing electron is obtained by the constraint of energy and momentum conservation. In our case, the electrons and protons are generated in coincidence. However, only the generated electrons are sent through the spectrometers. Ionization losses are also employed for the scattered particles when they traverse the target material, cells and scattering chamber. In addition, SIMC allows for emissions of real or virtual photons from incoming and outgoing particles. The momentum vectors of the charged particles are adjusted correspondingly to respect the four-momentum conservation.

Transportation of charged particles in HRS Transporting the electrons through the various elements in the spectrometer is done using the optics matrices produced by the Monte Carlo simulation program COSY [98]. COSY generates both the forward and backward matrices to simulate the magnetic properties of HRS. The forward matrices transport the particle vectors from the entrance window of the spectrometer to its focal plane going through every major aperture in the spectrometer, including the front, middle, and back surfaces of each magnet element and the transition pipes between magnets. SIMC checks the intercepts of particle vectors at the surface of each individual aperture and only records those events within the acceptance of all apertures. A total of 23 apertures [128] are included in the simulation model based on our best knowledge of their geometries and relative positions in the HRS (Fig. A-4).

Event Reconstruction If an event makes its way to the focal plane, it is further projected to the various detectors to assure they fall in the acceptance of the E12-07-108 triggers. In addition, smearing is applied to the particle positions at the two VDCs to account for the VDC resolution. The backward matrix

elements then reconstruct the particle vectors at the target side. The most probable ionization losses of the incident and scattered electrons are calculated and used to correct the measured values, after which the various physics variables can be readily obtained.

Cross section weighting and normalization The simulated events are generated assuming a uniform cross section profile. In order to take into account the variations of elastic cross sections within the HRS acceptance, it is necessary to weight each reconstructed event by a realistic model of their actual cross sections. We used the model obtained from a global analysis of existing data of proton form factors described in Ref. [53]:

$$G_{Ep} = \frac{1 - 1.651\tau + 1.287\tau^2 - 0.185\tau^3}{1 + 9.531\tau + 0.591\tau^2 + 4.994\tau^5}, \tag{4.1}$$

$$G_{Mp}/\mu_p = \frac{1 - 2.151\tau + 4.261\tau^2 + 0.159\tau^3}{1 + 8.647\tau + 0.001\tau^2 + 5.245\tau^3 + 82.817\tau^4 + 14.191\tau^5}, \tag{4.2}$$

where $\tau = Q^2/4M_p^2$, and μ_p is the proton's magnetic moment. The impact of model selections on the cross section results are studied in Sec. 4.6.4. In addition, the Monte Carlo results are normalized so that the effective luminosity used in the simulation matches that of the collected data.

4.1.1 Radiative Corrections

The Born approximation of the e-p elastic scattering (Eq. 1.24) has only a scattered electron and a recoiling proton in the final state. In this case, the kinematics of the scattered electron can be unambiguously calculated by energy and momentum conservation. The observed invariant mass would be a delta function centered at the proton mass and broadened by the finite resolution of the apparatuses. Extraction of the cross section would be as simple as counting the number of observed events fallen in the peak region and normalizing it by the accumulated luminosity.

However, a realistic measurement of e-p elastic scattering is inevitably complicated by various higher-order radiative processes. On the one hand, real photons are emitted

when the electron and proton are accelerated by the fields of nuclei in the target material, which causes a discrepancy between the detected electron's momentum and its actual momentum at the scattering vertex, leading to distortions in the extracted experimental spectra. On the other hand, additional virtual photons exchanged in the scattering process introduce next-to-leading order terms to the magnitude of the measured cross section. In order to extract the Born cross section from raw data, one has to unfold these radiative effects. In this section, the standard procedure for performing radiative corrections in inclusive elastic *e-p* scattering is discussed, followed by descriptions on the implementation of the radiative processes in SIMC.

General Formalism

The amplitude of the *e-p* elastic scattering process, derived under the assumption of the exchange of a single photon between the incident electron and the struck proton, only contains terms in the lowest order of the fine structure constant α. The corresponding cross section $\left(\frac{d\sigma}{d\Omega}\right)_{1\gamma}$ is often referred to as the Born cross section. In contrast, the cross section directly extracted from the observed data, $\left(\frac{d\sigma}{d\Omega}\right)_{\text{obs}}$, contains contributions from higher order processes and is related to $\left(\frac{d\sigma}{d\Omega}\right)_{1\gamma}$ by

$$\left(\frac{d\sigma}{d\Omega}\right)_{\text{obs}} = \left(\frac{d\sigma}{d\Omega}\right)_{1\gamma} \cdot RC. \tag{4.3}$$

The multiplicative factor RC is called the radiative correction factor and depends on the kinematics of the scattering process and the cutoff value at the radiative tail used in extracting the cross section. Its determination requires thorough knowledge of the underlying physics processes as well as details of the experimental setup.

Evaluation of Radiative Correction Factor for Inclusive *e-p* Elastic Scattering

The physics processes contributing to RC can be divided into two categories based on whether an extra virtual or real photon was produced in addition to the one exchanged between the incident electron and the struck proton. If a higher order

Feynman diagram contains only virtual photons, the final state is the same as that of the Born process, and its amplitude is added coherently to the Born amplitude. These processes are characterized by a loop in their Feynman diagrams (Fig. 4-1). According to the location of the loop in the diagram, these corrections are referred to as vacuum polarization, vertex correction, electron self-energy, two-photon exchange, etc. respectively. Loops in the Feynman diagram lead to divergences that are cancelled by incorporating the processes of real photon emission, also termed internal bremsstrahlung (Fig. 4-2). Emissions of real photons affect the detected momenta of scattered particles, hence corrections to them depend on the kinematic cuts applied in the analysis. Bremsstrahlung can also take place at nuclei other than the proton involved in the primary scattering vertex, which also needs to be considered in the radiative correction procedures.

The standard procedures for determining the radiative correction factor RC in Eq. 4.3 for inclusive electron elastic scattering experiments were first developed and discussed in Refs. [130–132] and later improved in Ref. [121]. Contributions from virtual photon emission (Fig. 4-1) and bremsstrahlung process (Fig. 4-2) were evaluated separately and then summed to cancel any divergences caused by the zero mass of photon (the so-called infrared divergence). In the treatment, the electron vertex correction and vacuum polarization term can be calculated exactly from Quantum Electrodynamics. Other high order diagrams in Fig. 4-1 involve couplings between a photon and a potentially off-shell proton. Their evaluations contain the strong interaction and depend on the model of proton internal structure. The practice used by Refs. [130, 131] is to assume that one of the two virtual photons is soft such that the proton can always be taken to be on shell, and then only extract the infrared divergent component from these diagrams. The error caused by neglect of non-divergent components was investigated in some early literatures and estimated to be smaller than 1% [133]. This approximation implies that in the last two diagrams in Fig. 4-1, the contribution from the scenario of two-hard-photon exchange (i.e., both photons have a sizeable momentum) is not taken into account. The overall correction factor

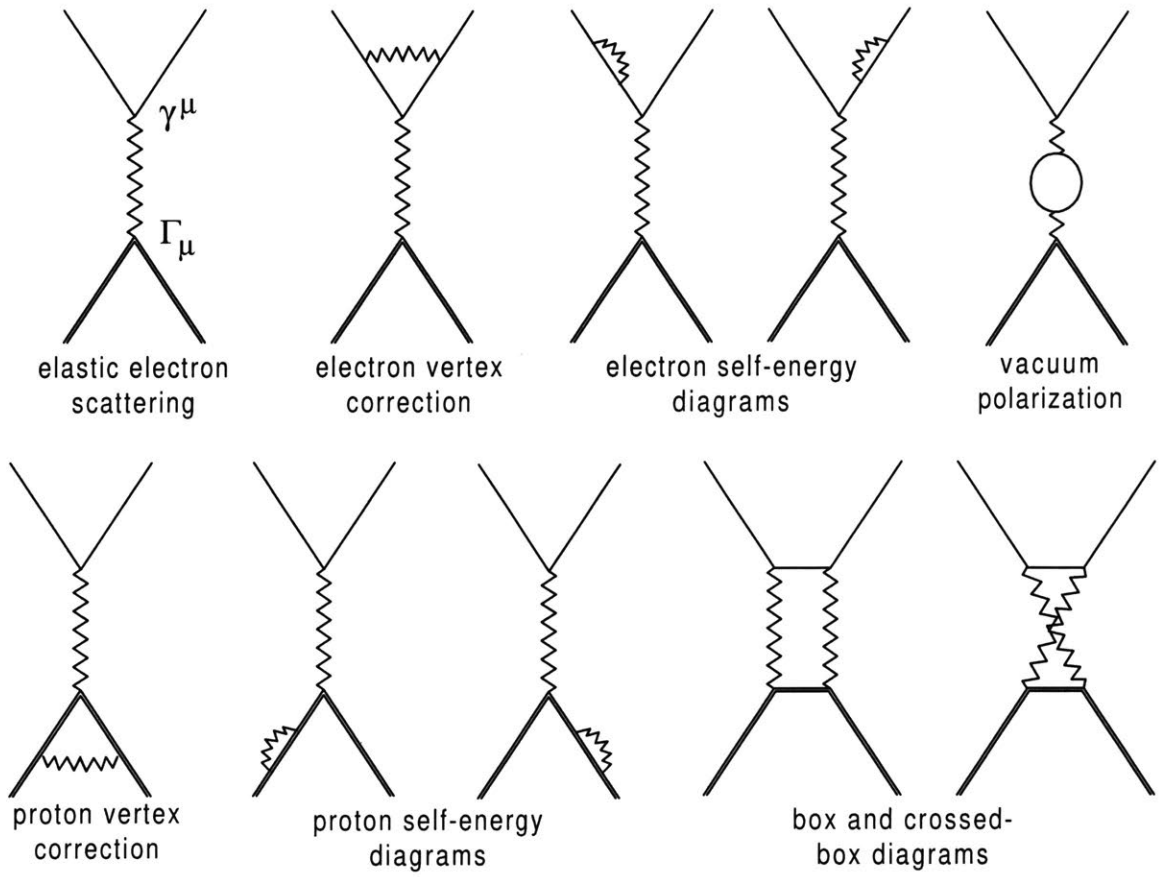

Figure 4-1: Leading and next-to-leading order Feynman diagrams for e-p elastic scattering. Reproduced from Ref. [129].

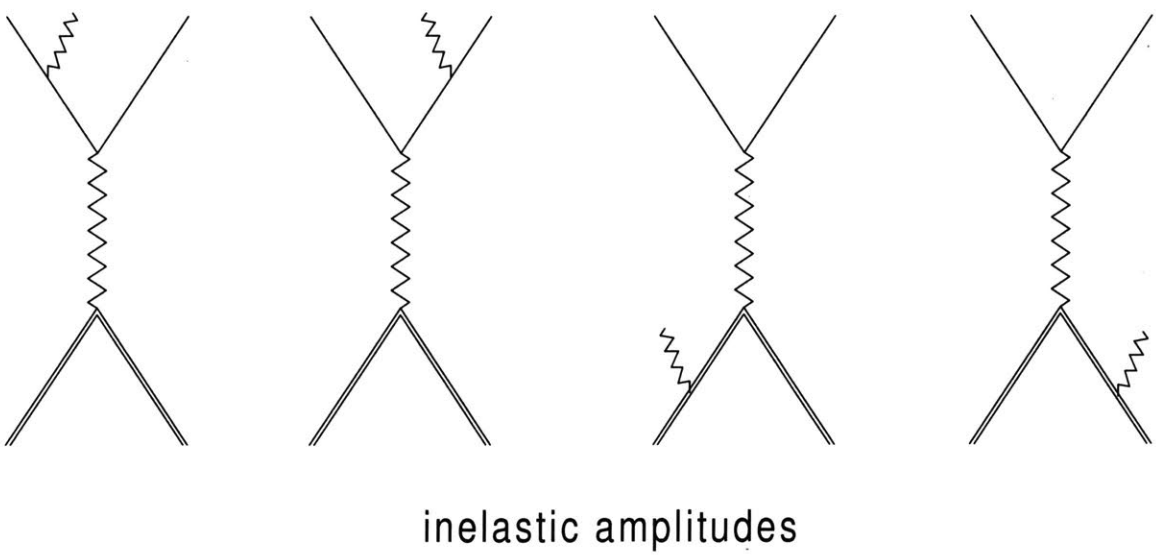

Figure 4-2: Feynman diagrams for real photon emission in e-p scattering. Reproduced from Ref. [129].

due to the loop diagrams in Fig. 4-1 was found to be [121, 131, 132, 134]

$$RC_{\text{virtual}} = e^{\delta_{\text{virtual}}} = e^{\delta_{\text{vertex}}+\delta^q_{\text{vac}}+\sum_{l=e,\mu,\tau}\delta^l_{\text{vac}}}, \tag{4.4}$$

where

$$\begin{aligned}
\delta^l_{\text{vac}} &= \frac{2\alpha}{\pi}\Big[-\frac{5}{9}+\frac{4}{3}\frac{m_l^2}{Q^2}+\big(\frac{1}{3}-\frac{2}{3}\frac{m_l^2}{Q^2}\big)\sqrt{1+\frac{4m_l^2}{Q^2}}\ln\Big(\frac{\sqrt{1+\frac{4m_l^2}{Q^2}}+1}{\sqrt{1+\frac{4m_l^2}{Q^2}}-1}\Big)\Big] && (4.5)\\
&\approx \frac{2\alpha}{\pi}\Big[-\frac{5}{9}+\frac{1}{3}\ln\frac{Q^2}{m_l^2}\Big] \qquad (Q^2 \gg m_l^2)\,, && (4.6)\\
\delta^q_{\text{vac}} &= -2\big[-1.513\times10^{-3}-2.822\times10^{-3}\ln\big(1+1.218Q^2\big)\big]\,, && (4.7)
\end{aligned}$$

and

$$\delta_{\text{vertex}} = \frac{2\alpha}{\pi}\Big[-1+\frac{3}{4}\ln\frac{Q^2}{m_e^2}\Big] \tag{4.8}$$

denote the contribution from lepton production in the vacuum polarization loop, quark production in the loop, and electron vertex contribution respectively.

The modification to the overall scattering amplitude due to internal bremsstrahlung (Fig. 4-2) was first calculated under the assumption that $\Delta E(1+2E_0/M_p) \ll E'$ in Ref. [130], where E_0 and E' are the energies of incident and elastically scattered electrons respectively, M_p is the proton mass, and ΔE is the energy cut-off of the scattered electrons in the radiative tail. This condition makes the Born amplitude factorize from the expression of single photon emission amplitude, and the resulting correction naturally falls in the general formalism of Eq. 4.3. Corrections for this approximation were introduced in Ref. [121]. An additional correction by Schwinger [135] was also included to account for the noninfrared divergent part of the soft photon emission cross section [121, 132]. The formulae for some of these terms are lengthy and complicated so they are not included here. Interested readers should refer to Refs. [121, 129–132] for more details. If we denote the three aforementioned corrections as $\delta_{\text{brem\_MT}}$, $\delta_{\text{brem\_Walker}}$, and δ_{Sch} respectively, the radiative correction factor

for internal bremsstrahlung can be expressed as

$$RC_{\text{real}} = e^{\delta_{\text{real}}} = e^{\delta_{\text{brem\_MT}}+\delta_{\text{brem\_Walker}}+\delta_{\text{Sch}}}, \tag{4.9}$$

and the total radiative correction factor is

$$RC = RC_{\text{virtual}} \cdot RC_{\text{real}}. \tag{4.10}$$

A complete treatment of radiative corrections also takes into account other processes whose effects on the scattered electrons are inseparable from those of the internal bremsstrahlung, including ionization loss and bremsstrahlung in the field of target nuclei that do not participate in the primary hard scattering (also called external bremsstrahlung). Evaluations of these corrections are very dependent on the details of the experimental setup, such as the geometry of the target and the thickness of various vacuum windows, and can vary significantly in the acceptance of the spectrometer. In order to measure the one-photon-exchange cross section with high precision, the radiative correction factor needs to be calculated for each individual bin of the acceptance which can be a complicated task.

Implementation of Radiative Processes in a Coincidence Framework (SIMC)

The Monte Carlo program SIMC simulates full $(e, e'p)$ coincidence events. In such a framework, radiative photons can be emitted by electrons and/or recoiling protons. Thus one can no longer integrate over all final states of the scattered proton as in the inclusive elastic scattering experiments. In SIMC, implementation of radiative effects follows the prescription of Refs. [134, 136] and is briefly described here for completeness.

In order to obtain the angular distribution of photon bremsstrahlung, it was first assumed that the emitted photon is soft, i.e., its energy is much less than the momenta of the initial and final state fermions. This is called the soft photon approximation (SPA). In this limit, one can derive the angular distribution for single photon emission

from a direct evaluation of the scattering amplitudes of the Feynman diagrams in Fig. 4-2:

$$A(\hat{\omega}) = -\frac{\alpha}{4\pi^2}\Big[\frac{k'}{\hat{\omega}\cdot k'} - \frac{p'}{\hat{\omega}\cdot p'} - \frac{k}{\hat{\omega}\cdot k} + \frac{p}{\hat{\omega}\cdot p}\Big]. \tag{4.11}$$

Here $\hat{\omega}$ is a unit 3-vector along the photon direction. k and k' (p and p') denote the four-momenta of initial and final states of the electron (proton) respectively.

The distribution of Eq. 4.11 is strongly peaked in the direction of the incoming and outgoing electron. In addition, a broad peak appears at the direction of the recoiling proton. It is thus justified to use the "extended peaking approximation" to approximate the distribution as follows:

$$A_{\text{peaking}}(\hat{\omega}) = \lambda_e\delta(\hat{\omega}-\hat{k}) + \lambda_{e'}\delta(\hat{\omega}-\hat{k'}) + \lambda_{p'}\delta(\hat{\omega}-\hat{p'}). \tag{4.12}$$

The $\hat{k}$ is a unit 3-vector along the direction of the space components of k, and $\hat{k'}$ and $\hat{p'}$ bear similar meanings. The three λ's are functions of the elastic kinematics and determined by distributing the integration of Eq. 4.11 among the three peaks. Their full expressions can be found in Ref. [134].

The distribution of energies lost in internal and external bremsstrahlung by the incident electron (E_e), the scattered electron ($E_{e'}$) and the recoiling proton ($E_{p'}$) is described by the following cross section [134]:

$$\begin{aligned}\frac{\mathrm{d}\sigma}{\mathrm{d}\Omega\,\mathrm{d}E_e\,\mathrm{d}E_{e'}\,\mathrm{d}E_{p'}} &= \Big(\frac{\mathrm{d}\sigma}{\mathrm{d}\Omega}\Big)_{1\gamma}(1-\delta_{\text{hard}})\frac{1}{\Gamma(1+bt_e)}\frac{1}{\Gamma(1+bt_{e'})}\\ &\times\frac{bt_e+\lambda_e}{k^{bt_e}(\sqrt{k\cdot k'})^{\lambda_e}}\frac{bt_f+\lambda_{e'}}{k'^{bt_{e'}}(\sqrt{k\cdot k'})^{\lambda_{e'}}}\frac{1}{E_e^{1-\lambda_e-bt_e}}\frac{1}{E_{e'}^{1-\lambda_{e'}-bt_{e'}}}\\ &\times\Big(1-\frac{bt_e}{bt_e+\lambda_e}\frac{E_e}{|\mathbf{k}|}\Big)\Big(1-\frac{bt_f}{bt_f+\lambda_f}\frac{E_f}{|\mathbf{k}'|}\Big)\\ &\times\frac{\lambda_{p'}}{E_{p'}}\Big(\frac{E_{p'}}{\sqrt{M_p p'^0}}\Big)^{\lambda_{p'}}\end{aligned} \tag{4.13}$$

The δ_{hard} term is the modification to the Born cross section due to virtual photon emissions and is equal to δ_{virtual} in Eq. 4.4; t_e ($t_{e'}$) is the total thickness in radiation length of the materials traversed by the incident (scattered) electron; b is a constant close to 4/3 characterizing particles' external bremsstrahlung spectra; $\Gamma(x)$ is the

Table 4.1: Cuts used for selection of MC events.

Fractional momentum δ	$-0.035 < delta < 0.035$
Out-of-plane angle $\theta_{\rm tg}$	$-0.08 < \theta_{\rm tg} < 0.08$
In-plane angle $\phi_{\rm tg}$	$-0.04 < \phi_{\rm tg} < 0.04$
$y_{\rm tg}$(cm)	$-0.1\lvert\sin\theta_0\rvert < y_{\rm tg} < 0.1\lvert\sin\theta_0\rvert$
Invariant mass W (GeV/c^2)	$0.86 < W < 1.05$

Gamma function.

The cross section in Eq. 4.13 factorizes into three independent distributions for the photons emitted by the incoming electron, the outgoing electron, and the recoiling proton. Thus in the SIMC program, E_e, $E_{e'}$, and $E_{p'}$ are generated independently from their marginal distribution and are assumed to be along the directions of $\mathbf{k}$, $\mathbf{k}'$ and $\mathbf{p}'$, respectively. Radiation along the direction of a given particle is then interpreted as radiation due to that particle and its momentum is adjusted accordingly. In this way, the correct particle momenta at the scattering vertex are used to evaluate the Born cross section. This effectively serves the same purpose as introducing the correction factor $\delta_{\rm brem\_Walker}$ in Eq. 4.9. The scattered electron is then transported to the spectrometer for further analysis.

To have the correct shape for the radiative tail in the reconstructed spectra, it is also necessary to have the correct weights for each generated scattering events. Details about the procedure to determine the weighting factor can be found in Ref. [137].

4.1.2 Selection of Monte Carlo Events

The simulation program only generates electron events, thus no PID cuts are needed in analyzing the simulated spectra. To make a sensible comparison to the collected data, we applied the same acceptance cuts to the simulated events as those described in Sec. 3.7. A summary of the cuts used for selecting simulated events can be found in Table 4.1.

4.2 Empty Target Background Subtraction

Electrons scattered from the nucleons in the aluminum entrance and endcap comprise a background in the observed elastic scattering rate and need to be subtracted. These quasi-elastic scattering events result in a broad peak near the proton mass in the invariant mass spectrum due to the Fermi motions of the nucleons inside a nuclei and are hard to isolate. Therefore, an aluminum dummy target consisting of two aluminum foils located at the positions of the entrance and endcap of the LH_2 target cell was used to determine the yield of such events. At each kinematics, electron scattering data from the dummy target were collected for a short period of time. The total thickness of the dummy target is about 0.02 radiation lengths, which is about 6 times more than that of the aluminum in LH_2 target cell (0.002 radiation lengths at the entrance and 0.0013 radiation length at the endcap). The purpose is two fold. On the one hand, the increased thickness leads to a higher scattering rate, which allows for a shorter data acquisition time for a given statistics; on the other hand, the dummy target is designed to have roughly the same overall radiation lengths as the LH_2 target, reducing the difference in the observed cross sections due to external bremsstrahlung. The settings of the dummy runs, including beam position, raster size, and set momentum, were all identical to these used in production runs.

The dummy target data were analyzed in the same manner as the production data. The number of electron events N^d_{raw} in the elastic window in the W spectrum was evaluated, as well as live time LT^d and VDC tracking efficiency η^d_{VDC}. The normalized yield is then

$$N^d_{\text{norm}} = \frac{N^d_{\text{raw}}}{LT^d \cdot \eta^d_{\text{VDC}}}. \tag{4.14}$$

The total background in the LH_2 data from scattering from the target entrance and endcap can be determined as

$$\text{BG}^c = \frac{t^c Q^c}{t^d Q^d} N^d_{\text{norm}} \cdot C_{br}, \tag{4.15}$$

where $Q^{c(d)}$ is the total charge incident on the LH_2 target cell (dummy target) and

$t^{c(d)}$ is the total thickness of the endcaps (dummy target).

The correction factor C_{br} accounts for the difference in external bremsstrahlung emission due to the distinct overall radiation length. When particles go through material of larger thickness, they tend to lose more energy and the observed distribution of events is shifted towards lower scattering energy (or higher W). This effect was studied in simulation with a phenomenological fit to the Born and radiative cross section data for various targets [138, 139]. Quasi-elastic scattering events from aluminum were generated by uniformly sampling from the phase space followed by a cross section weighting. The cross sections used here already employed the radiative effects. This process were first carried out for aluminum targets with a thickness of the dummy target, and then repeated for another target whose overall thickness is equal to that of the LH_2 endcaps. The resulting histograms were compared. The result is shown in Fig. 4-3.

The correction factors were determined for particles scattered off the entrance and hemispherical tip of the target cell separately (Table 4.2). It was found that C_{br} is slightly larger at the entrance due to the larger distinction in the experienced material thickness by electrons in the two targets. However, their difference was found to be within 2% for all kinematics. Since the typical fraction of the dummy background in the observed spectrum was less than 3%, it suffices to use the weighted average of the two values for the overall estimate of C_{br}, where the weights are determined by the relative thickness of the entrance and the endcap. The quasi-elastic cross section model does not work for the kinematics K5-16 due to the very large Q^2, where we took those values from K4-13(II) as an educated guess for C_{br} at K5-16. We assigned a 1% uncertainty to the correction factors for all kinematics. The largest contribution to uncertainties in the aluminum background subtraction comes from the uncertainties in the measured thickness of the cell tip of about 10% and that of the cell entrance of about 5%. Since the quasi-elastically scattered electrons only account for about 3% of all observed events, they lead to approximately a 0.21% uncertainty in the subtracted yield for all kinematics.

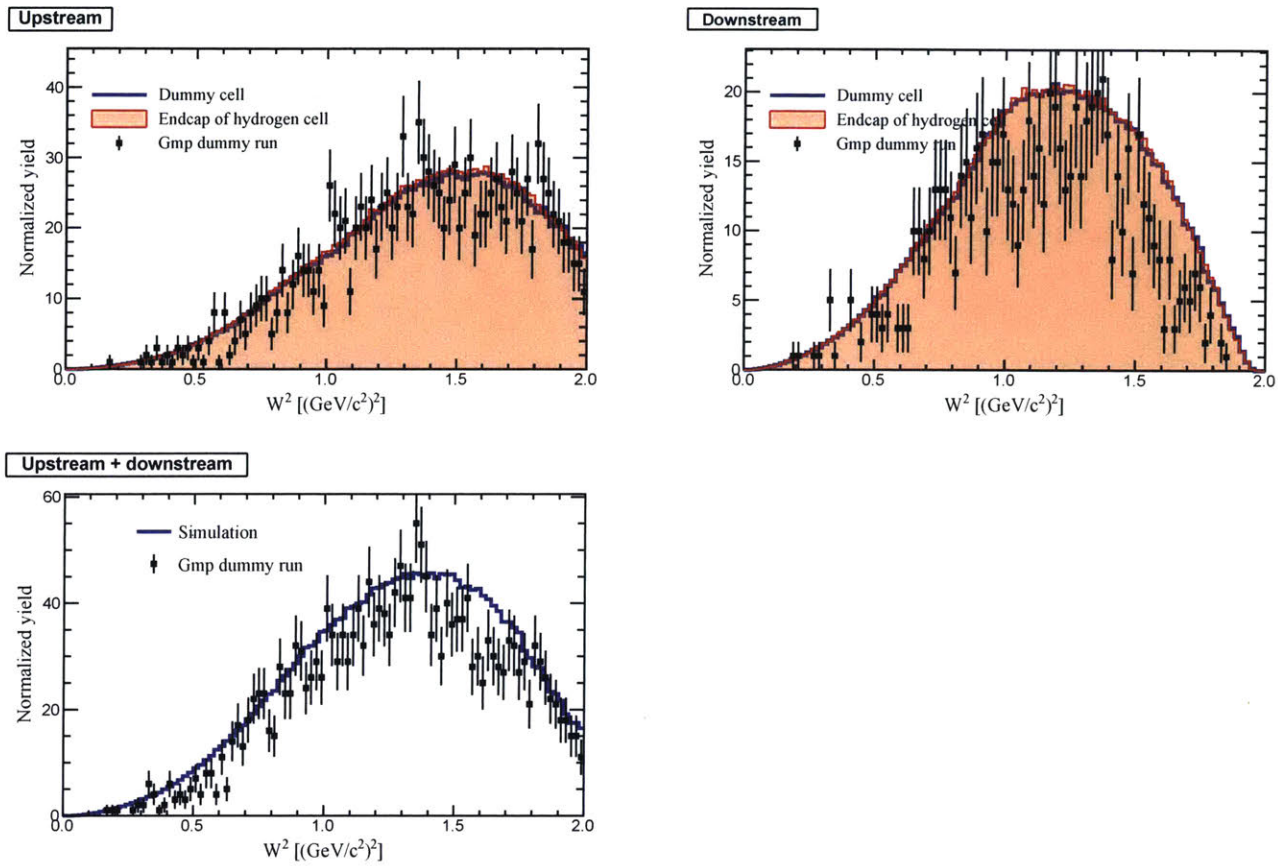

Figure 4-3: Determination of correction factor C_{br} in Eq. 4.15. The result shown here is for Kinematic K3-7.

Table 4.2: The values of C_{br} for various E12-07-108 kinematics

Kinematics	C_{br} (Entrance)	C_{br} (Endcap)	C_{br} (Average)
K4-9	1.029	1.010	1.022
K3-6	1.029	1.010	1.022
K3-7	1.030	1.013	1.023
K3-9	1.032	1.028	1.030
K4-13(II)	1.026	1.025	1.026
K5-16	N.A.	N.A.	N.A.
K1-2	1.030	1.014	1.024

4.3 Extraction of Cross Section

4.3.1 Formalism

The measured cross section $\frac{\mathrm{d}\sigma}{\mathrm{d}\Omega}^{data}$ is related to the observed yield and various correction factors by

$$\frac{\mathrm{d}\sigma}{\mathrm{d}\Omega}^{data} = \int \mathrm{d}E' \frac{N^{data}(E', \theta_{scatt}) - N^{\mathrm{BG}}(E', \theta_{scatt})}{\mathcal{L}^{data} \cdot \eta} \cdot \frac{RC^{data}}{A^{data}(E', \theta_{scatt})}, \tag{4.16}$$

where $N^{data}(E', \theta_{scatt})$ is the number of detected elastically scattered electrons with a momentum E' and at an angle θ_{scatt}, and $N^{\mathrm{BG}}(E', \theta_{scatt})$ is the yield resulting from other processes, most notably quasi-elastic scattering events from the target endcaps, as described in Sec. 4.2. $\eta = \eta_{\mathrm{PID}} \cdot \eta_{\mathrm{VDC}} \cdot ELT \cdot CLT$ corrects for various efficiencies and dead times. $\mathcal{L}^{data}$ is the integrated luminosity and is determined by the accumulated beam charge Q, target density ρ_{H_2}, and target length L:

$$\mathcal{L}^{data} = \frac{Q}{e} \cdot \frac{\rho_{H_2} L}{A_H} N_A. \tag{4.17}$$

Here $e = 1.60 \times 10^{-19}\,\mathrm{C}$ is the elementary charge, $N_A = 6.02 \times 10^{23}\,\mathrm{mol}^{-1}$ is the Avogadro constant, and A_H is the atomic weight of hydrogen.

The other two important ingredients in Eq. 4.16 are the radiative correction factor RC^{data} and the acceptance function $A^{data}(E', \theta_{scatt})$. Discussions on the radiative corrections can be found in Sec. 4.1.1. The acceptance function describes the probability of an electron being detected by the spectrometer.

There are two different approaches to extracting the cross section from data based on Eq. 4.16. The first approach attempts to evaluate the radiative correction factor and acceptance function for each bin of the target variables. Calculations of RC follows Eqs. 4.4, 4.9 and 4.10. A Monte Carlo program is usually used to evaluate the acceptance function. Physical apertures within the spectrometer might block the passage of electrons and only those within the spectrometer acceptance can make their way to the detector area. In the simplest model, electrons that are emitted at

a specific value of $(\delta, X_{tg}, Y_{tg}, \theta_{tg}, \phi_{tg})$ will have either a 100% probability of reaching the detector hut or a 100% probability of being blocked by the spectrometer apertures and magnets. In this case the acceptance function is a five-dimensional function that takes on a value of 1 in the area with perfect acceptance, and 0 in the area of perfect rejection. In practice, however, multiple scattering and the finite resolution of VDCs and spectrometer optics, smears out the edges of the acceptance function. On the other hand, the physics process depends only upon the momentum and full scattering angle, thus it makes sense to take the average of acceptance function over X_{tg}, Y_{tg} and the out-of-plane angle θ_{tg}, and convert it to a two-dimensional function of E' and θ_{scatt} only. A careful bin-by-bin calculation of the acceptance function can be performed by Monte Carlo simulations with a realistic spectrometer model, following which the cross section values can be extracted. This is the procedure taken by many previous cross section experiments [24, 121].

The second approach incorporates a cross section model in the simulation program, so the simulated spectra can be directly compared with data. The simulation software, as described in Sec. 4.1, uniformly generates electron events at the target and transports them through a realistic HRS model. They also experience various physics processes during the propagation, including multiple scattering, energy straggling, and emissions of radiative photons. The reconstructed events are then weighted by a phenomenological model of elastic e-p scattering. Similar to Eq. 4.16, we have

$$\frac{\mathrm{d}\sigma}{\mathrm{d}\Omega}^{MC} = \int \mathrm{d}E' \, \frac{N^{MC}(E', \theta_{scatt})}{\mathcal{L}^{MC}} \cdot \frac{RC^{MC}}{A^{MC}(E', \theta_{scatt})}, \tag{4.18}$$

where $N^{MC}(E', \theta_{scatt})$ is the yield in the simulation after cross section weighting. The effective luminosity $\mathcal{L}^{MC}$ can be inferred from the total number of generated Monte Carlo events N_{gen} and the volume of phase space $\Delta\theta_{tg} \cdot \Delta\phi_{tg}$ within which the events are sampled. Before being weighted by the modelled physics cross section, these events are picked from a uniform distribution in the phase space corresponding to unit cross section, thus

$$\mathcal{L}^{MC} = \frac{N_{gen}}{\int \mathrm{d}\Omega} = \frac{N_{gen}}{\Delta\theta_{tg} \cdot \Delta\phi_{tg}} \tag{4.19}$$

The applied acceptance cuts (Sec. 4.1.2) eliminated the region near the edge of the acceptance where the agreement between the data and simulation is not very good. It is assumed that $A^{data}(E', \theta_{scatt}) = A^{MC}(E', \theta_{scatt})$ for the rest of acceptance. The implementation of radiation of bremsstrahlung photons in the simulation also agrees with well-tested calculations of radiative correction factor [24]. Taking the ratio of Eq. 4.16 to Eq. 4.18, we have

$$\begin{aligned} \frac{\mathrm{d}\sigma}{\mathrm{d}\Omega}^{data} \Big/ \frac{\mathrm{d}\sigma}{\mathrm{d}\Omega}^{MC} &= \int \mathrm{d}E' \, \frac{N^{data}(E', \theta_{scatt}) - N^{\mathrm{BG}}(E', \theta_{scatt})}{\mathcal{L}^{data} \cdot \eta} \Big/ \int \mathrm{d}E' \, \frac{N^{MC}(E', \theta_{scatt})}{\mathcal{L}^{MC}} \\ &= \left(Y^{data} \Big/ Y^{MC}\right) \cdot \left(\mathcal{L}^{MC} / \mathcal{L}^{data}\right). \end{aligned} \tag{4.20}$$

Thus, the ratio of the yields in data and Monte Carlo simulation, when properly normalized, represents the ratio of the measured cross section to the model cross section. This approach was adopted in the analysis of several recent e-p elastic cross section experiments [32, 140] and proved to work well.

4.4 Alignment of Elastic Peak

The integral in Eq. 4.20 is performed over the energy of the scattered electron, E'. In order to calculate the ratio, one needs to decide on the lower and upper bounds of the integral for computing the yield. The value of the lower bound is selected to be above the pion production threshold to avoid contamination of inelastic scattering events. It also needs to be smaller than and far enough from the momentum dictated by elastic kinematics to reduce the influence of finite energy and angle resolution on the extracted cross sections. The upper bound is chosen to be higher than the elastic momentum to include the whole elastic peak. Since all we care about is the number of observed electrons within this energy range, we can also choose other kinematic variables to count the elastic events. A very convenient choice is the invariant mass of the undetected system, W, because its value is a direct indicator for the underlying process. Elastically scattered electrons results in a peak in the W spectrum at the proton mass and a long tail due to bremsstrahlung. For inelastic events, some of

the incident energy is absorbed to create new particles or resonances, and we have $W \geq M_p + m_{\pi^0} = 1.073\,\mathrm{GeV}/c^2$. We considered the region $0.86 < W < 1.05\,\mathrm{GeV}/c^2$ when extracting the ratios of the yields in the data and simulation.

Because of the uncertainties in the measured scattering angle, beam energy, and spectrometer momentum, there could be a slight offset between the position of reconstructed W peak and proton mass. To assure that we are comparing the yield in the same W range, we first performed a Gaussian fit to find the W peak position in the data and shifted it to the proton mass. The integral was then performed with respect to the "corrected" W spectrum and compared to the result in the simulation.

4.5 Results

As shown in Eq. 4.20, the ratio R of observed yield to Monto Carlo yield, after proper normalization by their individual luminosity, can be used to extract the measured cross sections from our phenomenological model:

$$\sigma_R^{data} = R\sigma_R^{MC} = R[\tau G_{Mp}^2(Q^2) + \epsilon G_{Ep}^2(Q^2)]. \tag{4.21}$$

Here the subscript R denotes reduced cross sections. The form factors $G_{Ep}(Q^2)$ and $G_{Mp}(Q^2)$ at a given Q^2 point are determined from the Arrington parameterizations described in Eqs. 4.1 and 4.2. The full cross sections are then derived from Eq. 1.26. Table 4.6 lists the extracted full cross sections and their uncertainties for the 7 E12-07-108 kinematics analyzed in this thesis.

4.6 Systematic Uncertainties Analysis

In this section, the study of the various systematic uncertainties in the cross sections extracted by the procedure described in Sec. 4.3 are described. In addition to the statistical uncertainty, they are important components of the total uncertainties and need to be thoroughly understood.

The two High Resolution Spectrometers in Hall A are modeled by a pair of COSY-generated optics matrices and a series of physical apertures implemented in the SIMC program. The COSY matrices determine the transport of charged particles in the spectrometer and the mapping from the particle tracks at the focal plane to the kinematic variables at the scattering vertex. At each aperture, the simulation program checks whether the trajectory is within its acceptance. If a particle is blocked by any of the aperture on its way to the detectors, this event is considered a miss and will be discarded. E12-07-108 analysis used a detailed model of the HRS where all apertures which are present in its technical drawing (Appendix A) are included in the simulation.

Two types of uncertainties are folded into the simulation in this process: one related to the spectrometer acceptance and the other to the generated COSY matrices. They are discussed in Sec. 4.6.1 and Sec. 4.6.2 respectively. Additional uncertainties resulting from the various approximations in implementing the radiative process must be considered as well. This is discussed in Sec. 4.6.3. The impacts of cross section models on the extracted cross sections are studied in Sec. 4.6.4.

4.6.1 Spectrometer Acceptance and Optics

The uncertainty due to spectrometer acceptance was studied by varying the acceptance cuts used in extracting the cross sections and observing the variation in the final results. The physics cross section should have no dependence on the selected acceptance cuts, thus the fluctuation is a measure of how well the spectrometer was modeled by the simulation program across its acceptance. It is important to note that this uncertainty is actually a combined result of acceptance effect and optics resolution, since the comparison between the data and simulation spectra relies on the reconstructed target variables.

Five sets of cuts were applied to extract the cross section for this study. The first set includes only these cuts described in Sec. 3.7 and the final E12-07-108 results were obtained with them. In the second and third sets, an additional requirement that the track projection be within the vicinity of the spectrometer central ray are

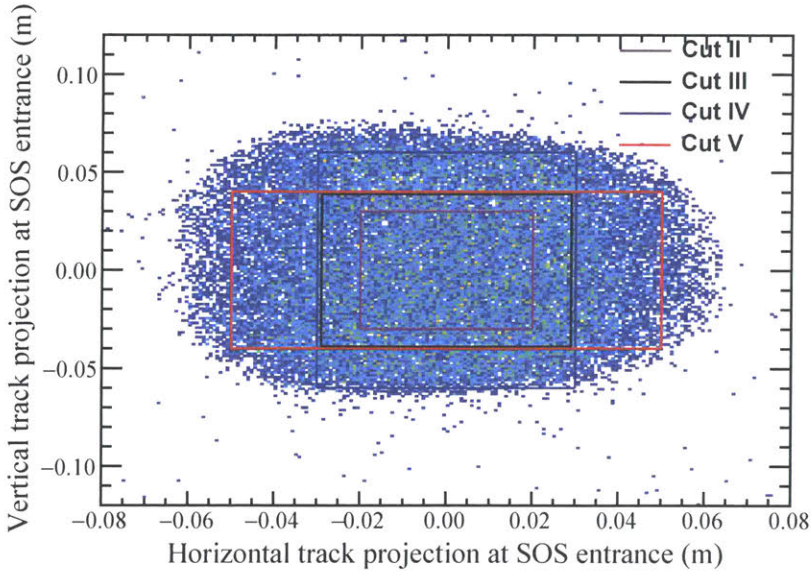

Figure 4-4: Visualization of the acceptance regions at the entrance of the spectrometer for cuts II, III, IV and V. Cut III is shrunk by a tiny amount so that it is visible in the plot. The events shown here are elastic electrons collected in K3-7 production runs.

imposed. The fourth and fifth sets are both similar to the second and the third but with an extended acceptance area at the entrance of HRS (Fig. 4-4). When the particle trajectories are close to the spectrometer central ray, they are most likely within the spectrometer acceptance, so whether these events can make their way to the detector hut is not sensitive to the positions of various apertures. However, the resolutions in the reconstructed target variables impacts the accuracy of the track projections, so the uncertainty in the result will be dictated by the optics precision. In contrast, the events with wild trajectory come close to the edge of the acceptance. Thus if the spectrometer model in the simulation is not accurate, one will be able to see a discrepancy between the simulated and observed spectra.

The extracted e-p cross sections with the five sets of cuts for the left HRS kinematics are summarized in Table 4.3. The variations of the extracted data-to-MC ratio are within 1.5%. Adding a cut at the spectrometer entrance can cause an increase in the extracted cross section in some kinematics, but a reduction in others.

Table 4.3: The dependence of extracted data to MC ratio on the acceptance cuts. See text for more details.

Kinematics	Cut I	Cut II	Cut III	Cut IV	Cut V
K3-6	1.0087	1.0043	1.0038	1.0104	1.0157
K3-7	1.0119	0.9992	0.9987	1.0020	1.0101
K4-9	1.0082	1.0014	1.0175	1.0134	1.0202

For example, Cut III is observed to decrease the data-to-MC ratio by about 0.5% for K3-6 and 1.2% for K3-7. Yet the ratio for K4-9 is larger by about 0.9% when using the same cuts. Based on these observations, a 1.5% point-to-point uncertainty and a 1.5% normalization uncertainty are assigned to the cross sections due to the spectrometer acceptance and optics.

4.6.2 Magnetic Field

The forward and backward matrices are generated based on the set field and geometry of each magnetic component in the spectrometer. A standard tune of the HRS magnets was used to generate these matrices for E12-07-108 analysis. The fluctuations in the actual magnetic field due to hardware instability, electronic noise and measurement resolution introduce uncertainties in the magnetic settings. This effect was studied in the simulation by varying the field of each magnet by about 0.25% independently and checking the variation in the values of the measured cross section. The effect produces a point-to-point uncertainty of 0.4% and a normalization uncertainty of 0.4%.

4.6.3 Radiative Correction

Radiative correction is a common topic in inclusive electron scattering experiments. The uncertainties in the radiative correction procedures described by Sec. 4.1.1 have been well studied in Refs. [6, 12, 24]. The point-to-point systematic uncertainty was estimated to be about 0.5% and the normalization error was 1.0%. These are the

values used in the E12-07-108 analysis. In addition, the uncertainties resulting from the choice of the cutoff values at the radiative tail of the W spectra were also added in quadrature. For the W cutoff values ranging from 1.00 GeV/c to 1.06 GeV/c, the typical point-to-point difference in the ratios between the data and simulation histograms is within 0.8%, which is taken as the estimated random point-to-point uncertainty on the implementation of the radiative process in the simulation software. Besides that, the normalization difference between the smallest and the largest values of W cutoff was observed to be about 1.2%. This difference not only comes from the distinct shapes of the radiative tail in the data and simulation, but it is also a consequence of unoptimized resolution matching of the drift chamber and optics matrices [24]. In the end, we took 1.0% as the estimated normalization uncertainty in picking the cutoff values for histogram integration and include it in the total normalization error of the radiative corrections.

4.6.4 Model Dependence

The simulation program takes a cross section model as an input for implementation of radiative processes and calculation of weights for each accepted simulation events. It is important that the models of the electromagnetic form factors G_{Ep} and G_{Mp} used here were fitted only to the Rosenbluth cross section data, excluding those from measurements of polarization transfer and beam asymmetry experiments. This is due to the intrinsic discrepancy between the two data sets which is believed to be ascribed to the contribution of two-hard-photon exchange process. Our radiative correction procedures followed the scheme described in Refs. [130–132, 134] and did not correct for any effects due to two-hard-photon exchange. This means that we should only compare our data to previous measurements where the radiative correction procedures were applied in a consistent manner. The polarization transfer measurements, on the contrary, are intrinsically insensitive to two-photon-exchange process. Thus form factor models based on polarization measurements are not suitable for cross section analysis.

To understand the dependence of extracted cross sections on the phenomenologi-

cal model used in the simulation software, we replaced Eqs. 4.1 and 4.2 by the global fitting result from Ref. [141] and compared to our current results. The largest variation in the extracted cross sections was less than 0.2% and the overall variation was about 0.1%. This is taken as the normalization uncertainty due to the cross section model. The point-to-point differences exhibit a small variation, and we assign a 0.1% point-to-point systematic error to the extracted cross sections.

4.6.5 Summary of Results

The estimated random point-to-point systematic uncertainties for the experiment are listed in Table 4.4. Table 4.5 includes the factors that affects the overall normalization uncertainty. The normalization uncertainties have the same impact on the data taken with the same spectrometer, but are independent for different spectrometers. The kinematics taken parallel with Experiment E12-06-114 was with low beam current ($\sim 10\,\mu A$) and their uncertainties in the beam charge are larger than the ones taken in the E12-07-108 dedicated period, where a much larger beam current ($\sim 60\,\mu A$) was used. The quadrature sum of the point-to-point and normalization uncertainties gives the absolute systematic uncertainties on the extracted cross sections. The results for Born cross sections are given in Table 4.6.

Table 4.4: E12-07-108 point-to-point systematic uncertainties.

Experimental Quantity	Uncertainty	$\Delta\sigma/\sigma$ (%)
Beam Energy	5×10^{-4}	0.3
Scattering Angle	0.3 mrad	0.1–0.5
Target Density	0.002	0.2
Beam Charge	0.06 µA	0.1–0.6
Acceptance	0.015	1.5
Tracking Efficiency	0.004	0.4
Deadtime Corrections	0.002	0.2
Target Cell Background	0.004–0.1	0.4–1
Radiative Corrections	0.008	0.8
HRS Magnetic Setting	0.004	0.4
Total		1.9–2.2

Table 4.5: E12-07-108 normalization uncertainties.

Experimental Quantity	Uncertainty	$\Delta\sigma/\sigma$ (%)
Beam Energy	5×10^{-4}	0.3
Scattering Angle	0.1 mrad	0.03–0.15
Target Density	0.0048	0.48
Target Length	0.0017	0.17
Beam Charge	0.1 µA	0.16–1
Acceptance	0.015	1.5
Tracking Efficiency	0.005	0.5
Deadtime Corrections	0.001	0.1
Target Cell Background	0.003–0.1	0.3–1
Radiative Corrections	0.01	1
Cross Section Model	0.001	0.1
HRS Magnetic Setting	0.004	0.4
Total		2.0–2.5

Table 4.6: Summary of the E12-07-108 kinematics and extracted elastic cross sections analyzed in this thesis.

HRS	E_{beam} (GeV)	θ_e (°)	Q^2 (GeV/c)^2	ϵ	$\sigma \pm \Delta\sigma_{\text{stat}} \pm \Delta\sigma_{\text{sys}} \pm \Delta\sigma_{\text{norm}}$ (µb/sr)
R	2.222	48.666	1.8585	0.6154	$(5.2998 \pm 0.0093 \pm 0.1006 \pm 0.1080) \times 10^{-4}$
R	6.427	55.900	9.0526	0.3322	$(2.0539 \pm 0.0207 \pm 0.0394 \pm 0.0428) \times 10^{-7}$
R	8.518	53.501	12.5678	0.3011	$(3.5516 \pm 0.0835 \pm 0.0776 \pm 0.0875) \times 10^{-8}$
R	10.587	48.666	15.7549	0.3088	$(1.3584 \pm 0.0255 \pm 0.0297 \pm 0.0335) \times 10^{-8}$
L	6.427	30.909	5.9471	0.7087	$(1.1001 \pm 0.0058 \pm 0.0219 \pm 0.0229) \times 10^{-5}$
L	6.427	37.008	6.9929	0.5992	$(2.8939 \pm 0.0145 \pm 0.0576 \pm 0.0601) \times 10^{-6}$
L	8.518	30.909	9.0021	0.6478	$(1.2704 \pm 0.0076 \pm 0.0253 \pm 0.0264) \times 10^{-6}$

Chapter 5

Results and Discussions

5.1 Comparison to Previous Measurements

The e-p elastic cross sections were extracted for 7 different kinematic settings of Experiment E12-07-108 in previous chapters of this thesis. In this section, we compare our results to previous measurements at similar Q^2 values.

The e-p elastic cross section is a function of both Q^2 and ϵ and their relation is described by Eq. 1.24. In order to make meaningful comparison, we first normalize the cross section values by a dipole cross section, which is defined as the cross section when both G_{Ep} and G_{Mp} are described by the dipole form factor:

$$\left(\frac{\mathrm{d}\sigma}{\mathrm{d}\Omega}\right)_{1\gamma,\mathrm{Dipole}} = \left(\frac{\mathrm{d}\sigma}{\mathrm{d}\Omega}\right)_{\mathrm{Mott}} \frac{\epsilon G_D^2(Q^2) + \tau\mu_p^2 G_D^2(Q^2)}{\epsilon(1+\tau)}, \tag{5.1}$$

where $G_D(Q^2)$ is given by Eq. 1.33. If the dipole approximation was reasonably good, the ratio between the measured cross section and Eq. 5.1 would be very close to 1. The results for various experiments are shown in Fig. 5-1. The data included here are from three SLAC experiments [6, 11, 12], two JLab experiments in the 6 GeV era [24, 32], and Experiment E12-07-108.

The main benefit of the E12-07-108 data lies in the range of intermediate to high Q^2 ($Q^2 \gtrsim 5\,\mathrm{GeV}^2$), where there had been no independent check of the SLAC results prior to this work. The measured cross sections from this thesis are in good

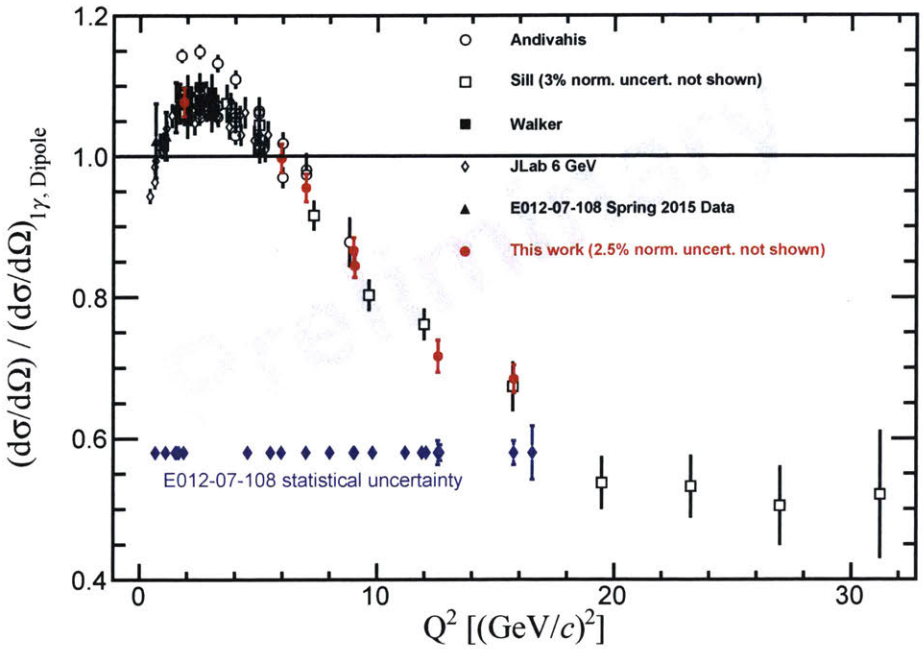

Figure 5-1: The e-p elastic cross sections normalized by the cross sections when a dipole form of the Sachs form factors is assumed.

agreement with the older data in this Q^2 range, but with a much smaller statistical and systematic uncertainties than the previous results. For example, Ref. [11] determined the e-p elastic cross section at $Q^2 = 15.72\,\mathrm{GeV}^2$ with a statistical uncertainty of 5% and a combined point-to-point and normalization uncertainty of 3.4%, while we measured the cross section at $Q^2 = 15.75\,\mathrm{GeV}^2$ with a 1.9% statistical uncertainty and the total systematic uncertainty is decreased to 2.7%. This translates to a reduction in the total uncertainties by a factor of 2.

It is also interesting to compare the kinematic coverage of Experiment E12-07-108 to the work in Ref. [11]. Fig. 5-2 shows the Q^2 and ϵ values for the data points collected in the two experiments. The SLAC data were taken at forward angles and much larger beam energy than that is available at CEBAF, while our experiment detected electrons scattered at large angles. As a result, the range of ϵ covered by the two data sets are very distinct at similar Q^2 values. The results presented in this thesis, as well as other E12-07-108 data points that will be analyzed in the near

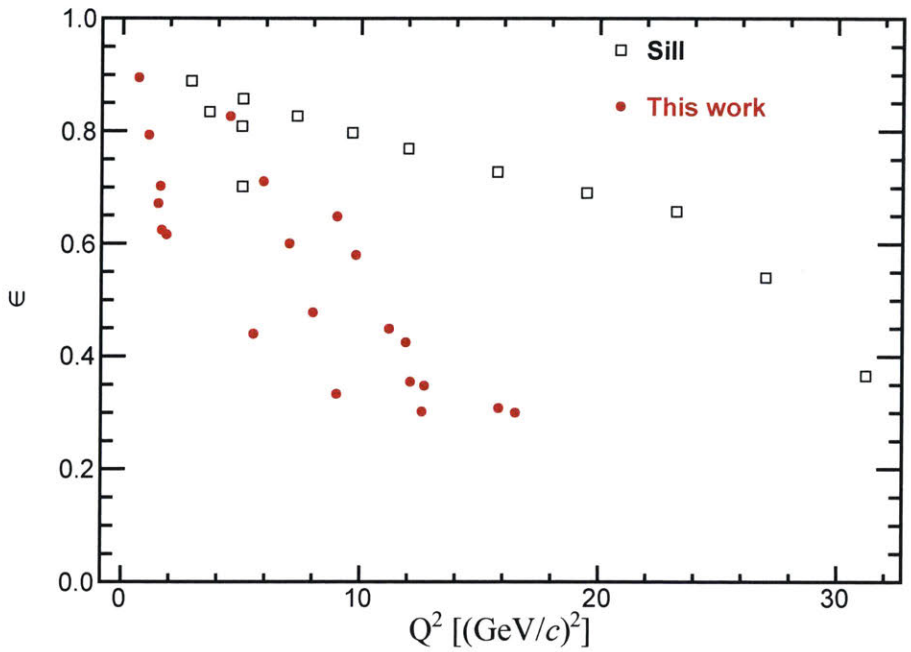

Figure 5-2: Comparison of kinematic coverage between Experiment E12-07-108 and that described in Ref. [11].

future, represent a great complement to the world cross section data set by extending the existing measurements to large scattering angle at large Q^2 values, and are very important for extracting a reliable parametrization of the proton form factors and the elastic cross sections in this Q^2 range.

The distinct ϵ ranges in the two data sets also lead to a major difference in the sources of the uncertainties in the extracted form factors. The reduced cross section in the Born approximation (Eq. 1.26) is a combination of contributions from the electric term and the magnetic term. At reasonably high Q^2, the magnetic term dominates due to two reasons. First of all, G_{Mp} is roughly 2.79 times larger than G_{Ep} even if the scaling behavior is true (which has been proved doubtable by recent polarization transfer results) due to the proton magnetic moment. Secondly, the magnetic term is weighted by τ, which increases linearly with Q^2. When it is impractical to perform the Rosenbluth separation technique to extract both G_{Ep} and G_{Mp} at large Q^2, one can still obtain the value of G_{Mp} with fairly good precision since it largely determines

the Born cross section. The reduced ϵ values in the E12-07-108 data translate into reduced contribution from G_{Ep} and allow for cleaner extractions of G_{Mp}. However, it will be more sensitive to the TPE corrections, whose effect decreases with ϵ, and drops to completely zero at $\epsilon = 1$ [142]. In contrast, the SLAC data are less sensitive to TPE contribution while the G_{Ep} contribution limits the precision of extracted G_{Mp} values there.

5.2 Extraction of Form Factors

Experiment E12-07-108 only conducted one cross section measurement at each Q^2 setting, thus the regular Rosenbluth separation technique cannot be deployed to extract the form factors. Since the magnetic form factors dominate the elastic cross sections in the relevant Q^2 range, one can obtain G_{Mp} with reasonable uncertainties by making assumptions about the form factor ratios. Prior to the observation of decreasing form factor ratio with Q^2 in the polarization transfer experiments, it was widely accepted that the Sachs electric and magnetic form factors satisfy the following relation at $Q^2 \gtrsim 2\,\mathrm{GeV}^2$:

$$\mu_p G_{Ep}/G_{Mp} = 1. \tag{5.2}$$

This assumption has been used in extracting the proton form factors from cross section measurements at $Q^2 > 9\,\mathrm{GeV}^2$ [11].

At the beginning of the twenty-first century, several polarization transfer experiments carried out at Jefferson Lab established the fact that the ratio of the form factors show a clear decreasing tendency in the current accessible Q^2 range. Ref. [18] performed a global fit of the polarization results up to $8.6\,\mathrm{GeV}^2$ and obtained the following parametrization for the relation between the ratio and Q^2:

$$\mu_p \frac{G_{Ep}}{G_{Mp}} = \frac{1 + B_0\tau + B_1\tau^2 + B_2\tau^3}{1 + B_3\tau + B_4\tau^2 + B_5\tau^3 + B_6\tau^4}, \tag{5.3}$$

with $B_0 = -5.7891$, $B_1 = 14.493$, $B_2 = -3.5032$, $B_3 = -5.5839$, $B_4 = 12.909$, $B_5 = 0.88996$ and $B_6 = 1.5420$. The curve representing such a function is shown in

Table 5.1: Extraction of G_{Mp} from the cross section results in Table 4.6. Two different assumptions were made in the calculation. The first assumes $\mu_p G_{Ep}/G_{Mp} = 1$. The second utilizes the polarization transfer result on the form factor ratio and extends it to $Q^2 > 8.6\,\mathrm{GeV}^2$.

Q^2 (GeV^2)	θ (°)	Assumption I		Assumption II	
		G_{Mp} term in σ (%)	G_{Mp}/μ_p	G_{Mp} term in σ (%)	G_{Mp}/μ_p
1.8585	48.666	87.00	$(7.93 \pm 0.11) \times 10^{-2}$	91.81	$(8.15 \pm 0.11) \times 10^{-2}$
9.0526	55.900	98.37	$(4.86 \pm 0.07) \times 10^{-3}$	99.97	$(4.90 \pm 0.07) \times 10^{-3}$
12.5678	53.501	98.93	$(2.42 \pm 0.05) \times 10^{-3}$	100.00	$(2.43 \pm 0.05) \times 10^{-3}$
15.7549	48.666	99.12	$(1.54 \pm 0.03) \times 10^{-3}$	100.00	$(1.55 \pm 0.03) \times 10^{-3}$
5.9471	30.909	94.90	$(1.14 \pm 0.01) \times 10^{-2}$	99.36	$(1.16 \pm 0.01) \times 10^{-2}$
6.9929	37.008	96.28	$(8.30 \pm 0.12) \times 10^{-3}$	99.72	$(8.45 \pm 0.12) \times 10^{-3}$
9.0021	30.909	96.85	$(4.97 \pm 0.07) \times 10^{-3}$	99.93	$(5.05 \pm 0.07) \times 10^{-3}$

Fig. 1-6.

Table 5.1 compares the G_{Mp} values as extracted based on the two assumptions. One can see that the magnetic form factor is much more significant than the electric form factor and amounts to more than 95% contribution to the total cross section at $Q^2 > 6\,\mathrm{GeV}^2$ in both cases. Eq. 5.3 corresponds to a form factor ratio which is much smaller than 1 at even intermediate Q^2, hence it results in a larger contribution from G_{Mp} to the total cross section. However, the distinction in the extracted G_{Mp} values between the two assumptions is in general very small relative to the total experimental uncertainties. The largest difference is seen at the lowest Q^2 value and is roughly the same size as the total error bar on G_{Mp}[1]. We will take the values extracted based on Eq. 5.3 (Assumption II in Table 5.1) for the analysis in the following sections. Notice that the ratio of G_{Ep}/G_{Mp} has not been measured above $8.6\,\mathrm{GeV}^2$, thus it is not clear whether Eq. 5.3 is still a reasonable parameterization at very large Q^2. However, as can be seen from Table 5.1, the values of extracted G_{Mp} do not change appreciably if the relation $|\mu_p G_{Ep}/G_{Mp}| < 1$ still holders. This is indeed predicted to be the case

[1]Because the cross section is proportional to the squares of the form factors, the relative uncertainty in G_{Mp} is half of that in the cross section. We have also neglected the uncertainty due to TPE effects here.

in various theoretical models. On the contrary, the G_{Mp} values extracted from SLAC data [11] are more sensitive to the actual values of $\mu_p G_{Ep}/G_{Mp}$. For example, at $Q^2 = 12$ and $15\,\mathrm{GeV}^2$, the difference in the magnetic contribution to the total cross section between the two assumptions amounts up to 2% for the SLAC data, while it is less than 1.1% for our kinematics. Our extraction of G_{Mp} is less model dependent in this sense.

Fig. 5-3 shows the proton magnetic form factor G_{Mp} extracted in Experiment E12-07-108, along with the results from Refs. [6, 11, 12, 24, 32]. These data represent the high precision G_{Mp} data at intermediate to high Q^2 from unpolarized e-p elastic scattering cross section experiments. Our data appear higher than those of the other experiments at $Q^2 < 6\,\mathrm{GeV}^2$. This discrepancy comes from the fact that we used the polarization transfer result (Eq. 5.3) to estimate the form factor ratio, which is not consistent with the ratio measured by unpolarized cross section experiments. At higher Q^2, the discrepancies in the G_{Mp} values diminish, thanks to the complete dominance of G_{Mp} over G_{Ep}.

5.3 Comparison to Existing Fits

Various parametrizations of the proton magnetic form factor exist. They either originate from a phenomenological model with some physics inspiration and a few tunable free parameters, or are completely from an empirical fit of the experimental data. Some of these fits are presented in Fig. 5-3.

Kelly [27] proposed a parametrization of the form factor which ensures the Q^{-4} asymptotic behavior at high Q^2 dictated by the dimensional scaling rule:

$$G_{Mp}(Q^2) = \frac{1 + a_1\tau}{1 + b_1\tau + b_2\tau^2 + b_3\tau^3}, \tag{5.4}$$

where both numerator and denominator are polynomials in $\tau = Q^2/4M_p^2$ and the degree of the denominator is larger than that of the numerator by 2. The parameters were found by fitting to a selection of experimental results of unpolarized cross section

and polarization measurements available then. Data for G_{Ep} using the Rosenbluth method were omitted for $Q^2 > 1\,\mathrm{GeV}^2$ to emphasize recoil or target polarization results. The parametrization is shown as the red solid curve in Fig. 5-3.

Arrington performed a global analysis of proton elastic form factor data using calculations of two-photon-exchange effects in the framework of Ref. [44]. In order to have a fit valid at both very low Q^2 and the highest Q^2 values of the existing data, a fitting function in a similar form as Eq. 5.4 was used, but with a 3rd-order polynomial in the numerator and a 5th-order polynomial in the denominator. The fitting to TPE-corrected cross section data and the form factor ratios from polarization transfer experiments resulted in a parametrization that can reasonably reconcile the discrepancy in the extracted values for $\mu_p G_{Ep}/G_{Mp}$ between the two approaches. The fitting result for G_{Mp} is illustrated by the blue dotted curve in Fig. 5-3. In addition, a parametrization of the TPE-uncorrected elastic cross sections is provided by the effective magnetic and electric form factors. They are supposed to describe the Born cross section data that were radiatively corrected in the framework of Refs. [131, 132]. This is shown as the gray dashed curve.

The Kelly fit and Arrington fit with TPE correction both describe the evolution of E12-07-108 data points with Q^2 very well, with corresponding χ^2 of 0.819 and 0.791 per degree of freedom respectively. The Arrington fit to TPE uncorrected data does not catch the trend of G_{Mp} data at intermediate Q^2 values. For instance, the measured magnetic form factor at $Q^2 = 5.95\,\mathrm{GeV}^2$ is about 2.9 error bars away from the value predicted by the parameterization. This is not surprising since the difference in the obtained G_{Mp} values from the two assumptions in Table 5.1 for this Q^2 value has the size of about 2 error bars. The TPE-uncorrected cross section data is known to have intrinsic disagreement with the polarization transfer data. The assumption II that we used in extracting our magnetic form factors comes from polarization transfer experiments and will lead to inconsistency with the gray dashed curve in Fig. 5-3, whose average χ^2 is found to be 2.07 per degree of freedom.

We also plotted one of the most successful VMD fits—the Lomon fit [143]—against the experimental results for the proton magnetic form factor in Fig. 5-3. It is based

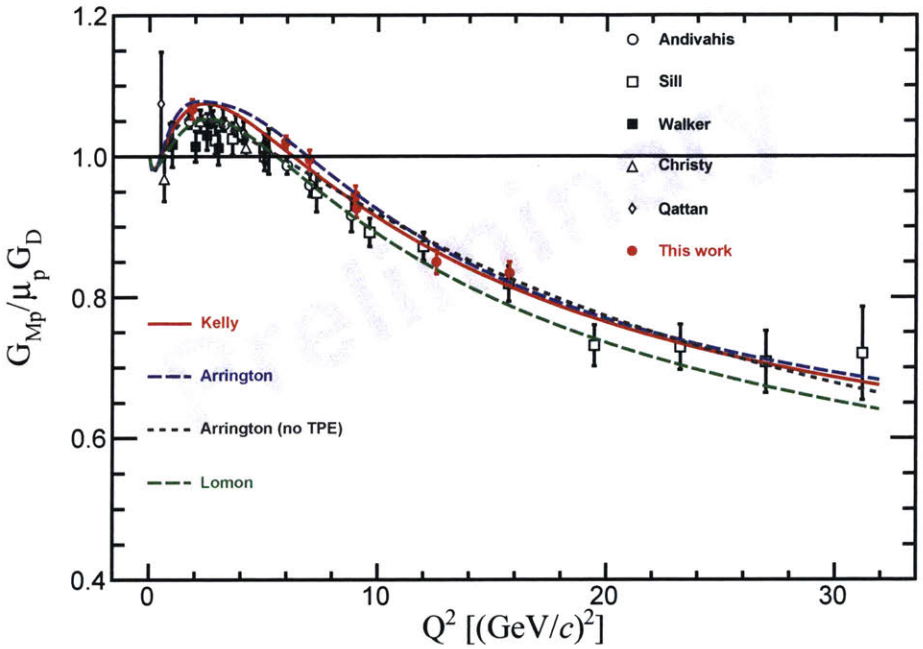

Figure 5-3: Extracted G_{Mp} values from Experiment E12-07-108. Also shown here are experimental results from Refs. [6, 11, 12, 24, 32]. The phenomenological fits in the figure are from Kelly [27], Arrington [53], Lomon [143]

on the model proposed by Gari and Krümpelmann [144] in which the ρ, ω, and ϕ vector meson pole contributions evolve at high momentum transfer to conform to the predictions of perturbative QCD. Lomon extended the Gari-Krümpelmann models to include the width of the ρ meson by substituting the result of dispersion relations for the pole and the addition of the $\rho'(1450)$ isovector vector meson pole and the $\omega'(1419)$ isoscalar vector meson pole. This model is phenomenological in nature and involves a number of free parameters to be tuned to fit the data. The values of the best fit parameters provide important information about the roles played by mesons in the electromagnetic form factors of the nucleon at low Q^2 and the transition from meson dynamics to perturbative QCD behavior at high Q^2. While the Lomon fit is known to be successful in representing the existing data across the entire available Q^2 range, it appears systematically lower than our data points. This difference is only made prominent by the much higher precision of our result when compared to the old data from Ref. [6] and Ref. [11]. A refit of the Lomon model is desired to better describe the trend of the magnetic form factor at large Q^2 revealed by our data.

Table 5.2 shows the χ^2 values for previous measurements and our results of the proton magnetic form factor compared to the four parametrizations shown in Fig. 5-3 at Q^2 larger than $5\,\mathrm{GeV}^2$. The fairly poor agreement between Lomon fit and our data points is obvious. The relatively large χ^2 value for the Arrington model with TPE corrections results from the fact that these form factors were extracted with only standard radiative corrections applied.

5.4 Conclusions

Experiment E12-07-108 performed high precision measurements of e-p elastic cross sections over a Q^2 range from below $1\,\mathrm{GeV}^2$ up to $16.5\,\mathrm{GeV}^2$. As one of the first two experiments carried out at Jefferson Lab after the 12 GeV energy upgrade of the CEBAF accelerator, enormous experience has been gained on the operation and performance of various experimental apparatus, which will be beneficial for upcoming experiments in the JLab 12 GeV physics program.

Table 5.2: χ^2 of the measured G_{Mp} values compared to the predictions of the four phenomenological models shown in Fig. 5-3. The results for two data sets are presented here. The first set (labelled as "previous data" in the table) includes all data points prior to Experiment E12-07-108 and with $Q^2 > 5\,\mathrm{GeV}^2$ in Fig. 5-3. The second set contains our data points with $Q^2 > 5\,\mathrm{GeV}^2$.

Model	Previous data		Our data	
	χ^2	Data points	χ^2	Data points
Kelly	20.25	15	5.69	6
Arrington	52.39	15	5.05	6
Arrington (no TPE)	9.72	15	13.67	6
Lomon	6.16	15	34.13	6

The E12-07-108 data is an important independent check of the SLAC results at large Q^2. In addition, the overall precision of the measured cross sections is greatly improved over the existing data. This thesis presented the results for 7 out of all collected kinematics. The final results for all E12-07-108 kinematics are expected in the near future.

The high precision E12-07-108 data allow for stringent tests of various QCD models in the intermediate to high Q^2 regime, which is also widely believed to be the transition region from non-perturbative to perturbative QCD. Our measurements will be a crucial piece of information for settling theoretical debate over the behavior of the nucleon form factors in this Q^2 range. The results show that our measurements are in general agreement with previous data, but with different kinematic coverage. In addition, our high quality, high precision data also provide the possibility to improve the parametrization of the nucleon form factors. The full E12-07-108 results will be used for understanding the dimensional scaling, constrain the pQCD model, and provide one of the cornerstones of GPD modeling.

Understanding of nucleon form factors at large Q^2 is one of the most important topics in the JLab 12 GeV physics program. The Experiment E12-07-109 intends to extend the proton form factor ratio data to $11.0\,\mathrm{GeV}^2$. The Experiment E12-09-019 proposes to measure the neutron magnetic form factor at Q^2 values as high as

13.5 GeV^2. The Experiment E12-09-016 aims at mapping the neuron electric form factor in a Q^2 range up to 10 GeV^2. These experiments, combined with the E12-07-108 results, will provide benchmarks for all theoretical predictions of nucleon structure, and serve as important inputs to the interpretation of many other experiments in nuclear and hadronic physics. They will also encourage more theoretical efforts towards a better understanding of QCD.

Appendix A

Miscellaneous Experimental Records

This appendix includes a collection of technical drawings for the apparatuses used in Experiment E12-07-108, including sieve slit (Fig. A-1), scattering chamber (Fig. A-2), assembly of various targets on the target ladder (Fig. A-3), and the high resolution spectrometer (Fig. A-4).

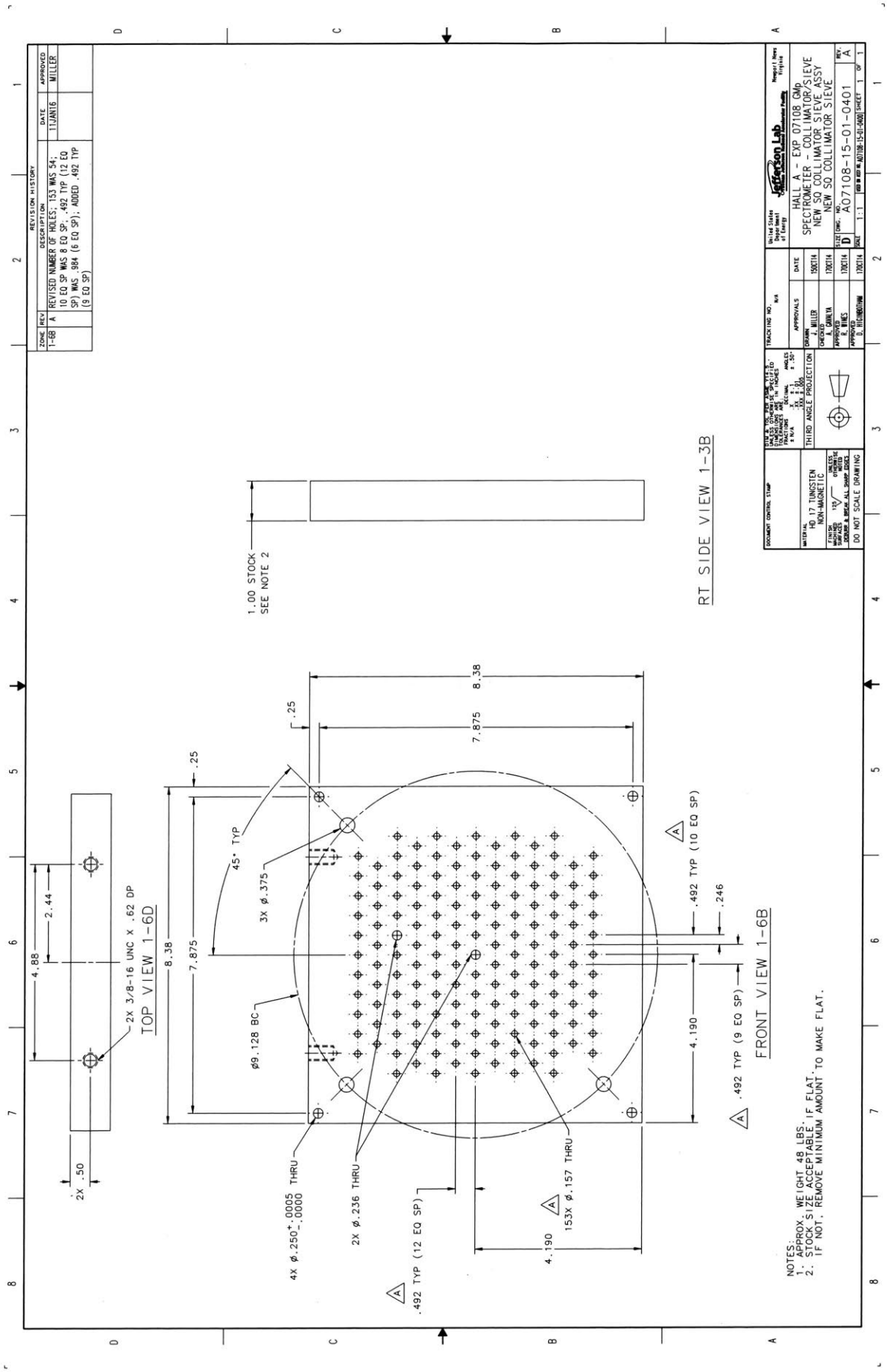

Figure A-1: Technical drawing for the sieve slit used in E12-07-108 optics calibration.

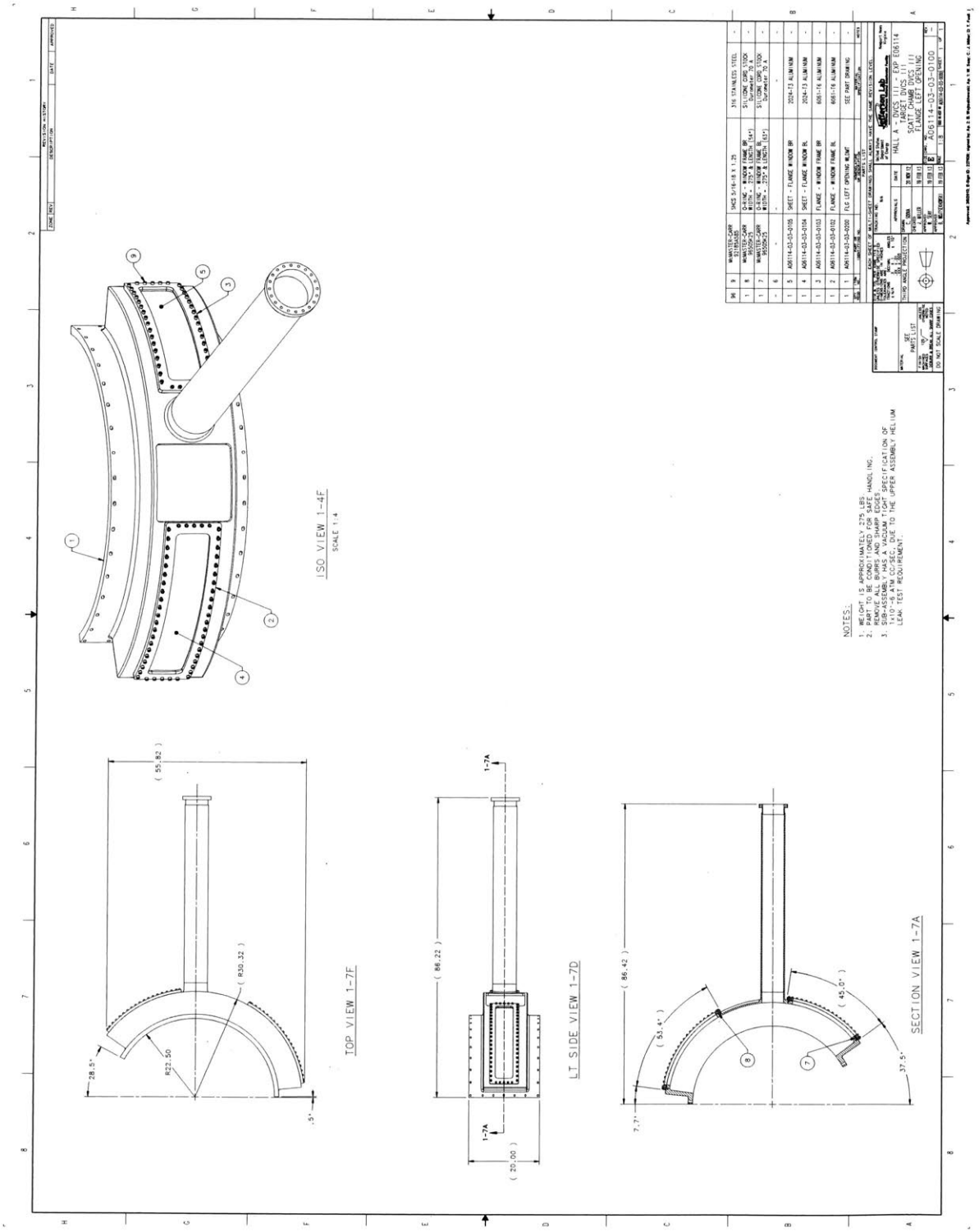

Figure A-2: Design of the scattering chamber for Experiments E12-07-108 and E12-06-114.

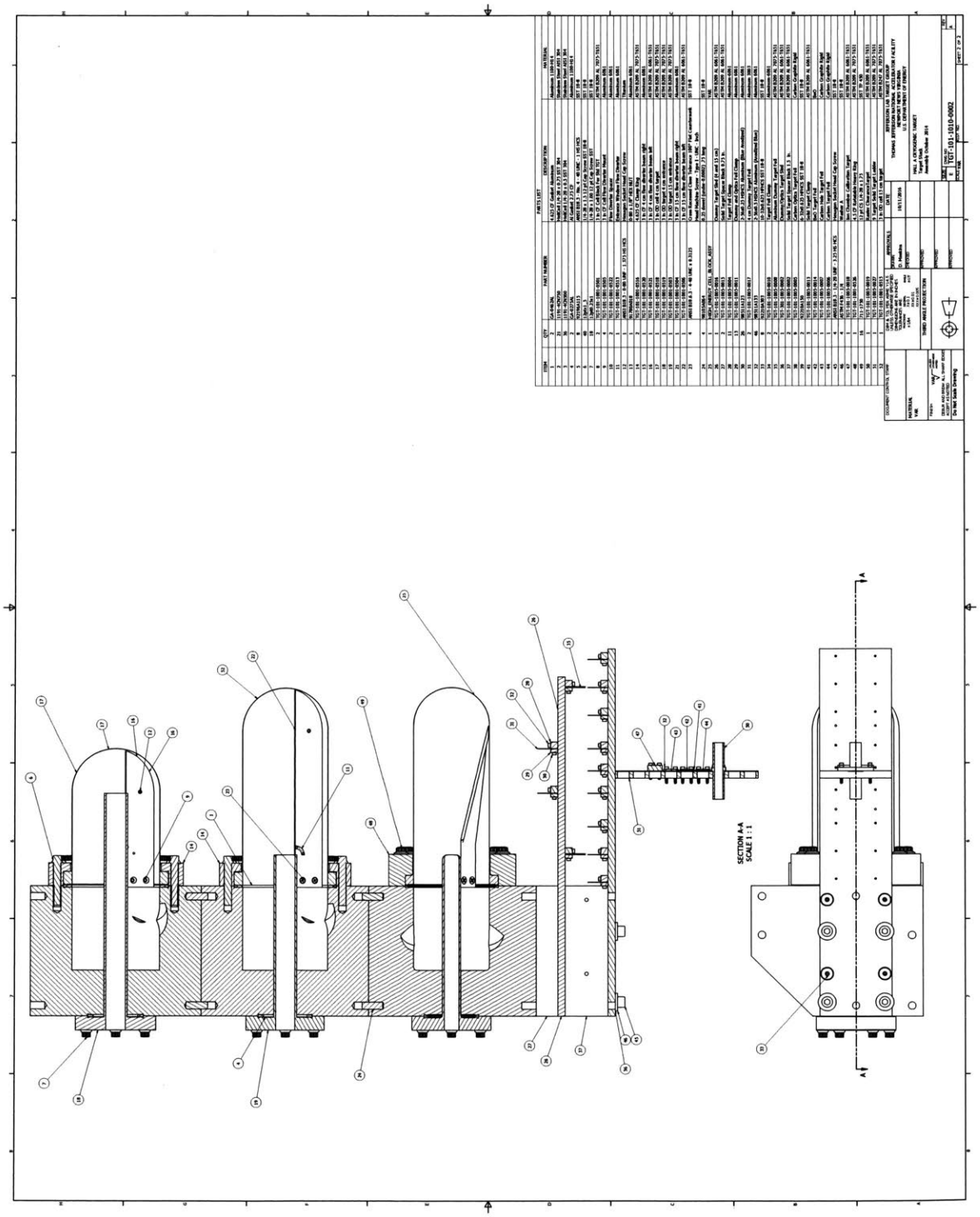

Figure A-3: Target ladder assembly for Experiments E12-07-108 and E12-06-114.

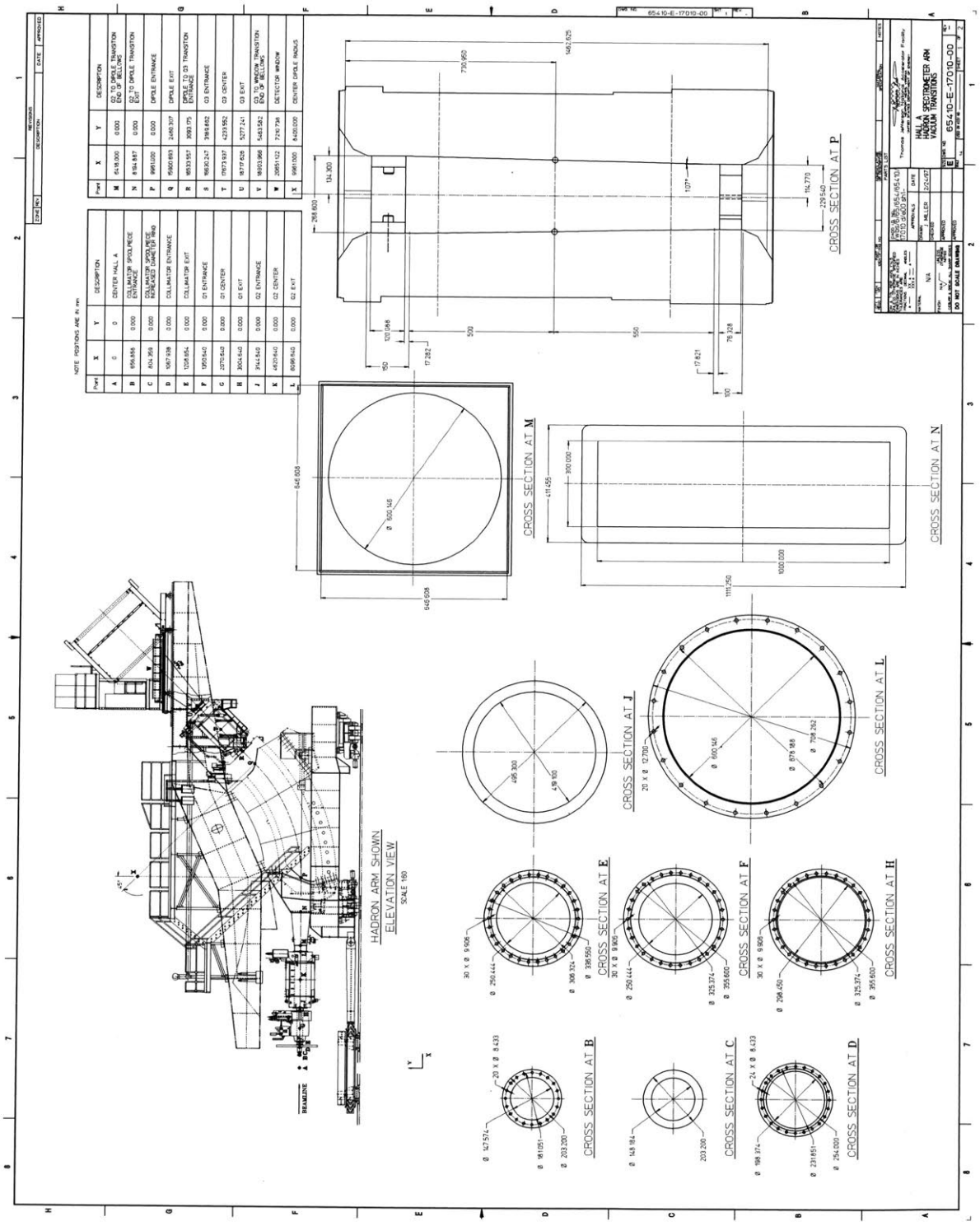
HADRON ARM SHOWN
ELEVATION VIEW
SCALE 1:60
BEAMLINE
CROSS SECTION AT M
CROSS SECTION AT N
CROSS SECTION AT P
CROSS SECTION AT J
CROSS SECTION AT L
CROSS SECTION AT E
CROSS SECTION AT F
CROSS SECTION AT H
CROSS SECTION AT B
CROSS SECTION AT C
CROSS SECTION AT D
NOTE: POSITIONS ARE IN mm
HALL A SPECTROMETER ARM VACUUM TRANSITIONS
65410-E-17010-00
DO NOT SCALE DRAWING

(a)

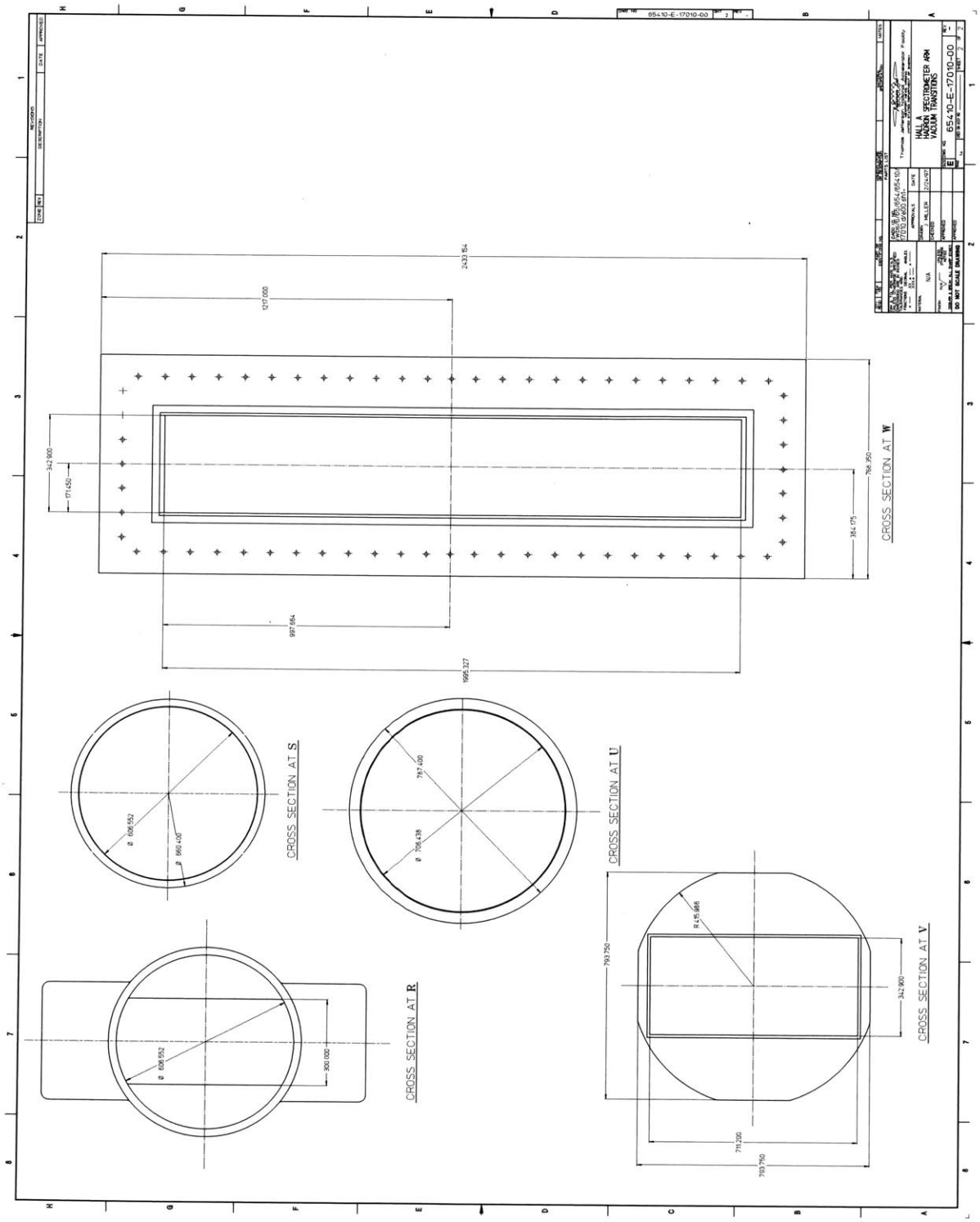

(b)

Figure A-4: Drawing of the HRS and the positions and shapes of various apertures

Bibliography

[1] I. Estermann, R. Frisch, and O. Stern, Nature **132**, 169 (1933).

[2] R. W. McAllister and R. Hofstadter, Phys. Rev. **102**, 851 (1956).

[3] R. Hofstadter, Rev. Mod. Phys. **28**, 214 (1956).

[4] M. Breidenbach, J. I. Friedman, H. W. Kendall, E. D. Bloom, D. H. Coward, H. DeStaebler, J. Drees, L. W. Mo, and R. E. Taylor, Phys. Rev. Lett. **23**, 935 (1969).

[5] A. W. Thomas and W. Weise, *The Structure of the Nucleon* (Wiley-VCH, 2001).

[6] L. Andivahis *et al.*, Phys. Rev. D **50**, 5491 (1994).

[7] W. Bartel *et al.*, Nucl. Phys. B **58**, 429 (1973).

[8] C. Berger *et al.*, Phys. Lett. B **35**, 87 (1971).

[9] T. Janssens *et al.*, Phys. Rev. **142**, 922 (1966).

[10] J. Litt *et al.*, Phys. Lett. B **31**, 40 (1970).

[11] A. F. Sill *et al.*, Phys. Rev. D **48**, 29 (1993).

[12] R. C. Walker *et al.*, Phys. Rev. D **49**, 5671 (1994).

[13] X. Ji, Phys. Rev. Lett. **78**, 610 (1997).

[14] A. Radyushkin, Phys. Lett. B **380**, 417 (1996).

[15] I. C. Cloët, C. D. Roberts, and A. W. Thomas, Phys. Rev. Lett. **111**, 101803 (2013).

[16] F. Halzen and A. D. Martin, *Quarks and Leptons: An Introductory Course in Modern Particle Physics* (Wiley, 1984).

[17] D. J. Griffiths, *Introduction to Elementary Particles*, 2nd ed. (Wiley-VCH, 2008).

[18] V. Punjabi, C. F. Perdrisat, M. K. Jones, E. J. Brash, and C. E. Carlson, Eur. Phys. J. A **51**, 79 (2015).

[19] V. Punjabi *et al.* (Jefferson Lab Hall A Collaboration), Phys. Rev. C **71**, 055202 (2005).

[20] L. N. Hand, D. G. Miller, and R. Wilson, Rev. Mod. Phys. **35**, 335 (1963).

[21] L. E. Price, J. R. Dunning, M. Goitein, K. Hanson, T. Kirk, and R. Wilson, Phys. Rev. D **4**, 45 (1971).

[22] F. Borkowski, G. Simon, V. Walther, and R. Wendling, Nucl. Phys. B **93**, 461 (1975).

[23] G. Simon, C. Schmitt, F. Borkowski, and V. Walther, Nucl. Phys. A **333**, 381 (1980).

[24] M. E. Christy *et al.* (E94110 Collaboration), Phys. Rev. C **70**, 015206 (2004).

[25] I. A. Qattan *et al.* (E01001 Collaboration), Phys. Rev. Lett. **94**, 142301 (2005).

[26] P. N. Kirk *et al.*, Phys. Rev. D **8**, 63 (1973).

[27] J. J. Kelly, Phys. Rev. C **70**, 068202 (2004).

[28] E. J. Brash, A. Kozlov, S. Li, and G. M. Huber, Phys. Rev. C **65**, 051001 (2002).

[29] M. Meziane *et al.* (GEp2γ Collaboration), Phys. Rev. Lett. **106**, 132501 (2011).

[30] A. J. R. Puckett *et al.* (The Jefferson Lab Hall A Collaboration), Phys. Rev. C **85**, 045203 (2012).

[31] A. J. R. Puckett *et al.*, Phys. Rev. Lett. **104**, 242301 (2010).

[32] I. A. Qattan, *Precision Rosenbluth Measurement of the Proton Elastic Electromagnetic Form Factors and Their Ratio at for* $Q^2 = 2.64,\ 3.20,$ *and* $4.10\ \mathrm{GeV}^2$, Ph.D. thesis, Northwestern University (2005).

[33] B. D. Milbrath *et al.* (Bates FPP Collaboration), Phys. Rev. Lett. **80**, 452 (1998).

[34] T. Pospischil *et al.*, Eur. Phys. J. A **12**, 125 (2001).

[35] M. K. Jones *et al.* (The Jefferson Lab Hall A Collaboration), Phys. Rev. Lett. **84**, 1398 (2000).

[36] O. Gayou *et al.* (Jefferson Lab Hall A Collaboration), Phys. Rev. Lett. **88**, 092301 (2002).

[37] A. J. R. Puckett *et al.*, Phys. Rev. C **96**, 055203 (2017).

[38] P. A. M. Guichon and M. Vanderhaeghen, Phys. Rev. Lett. **91**, 142303 (2003).

[39] J. Arrington, P. Blunden, and W. Melnitchouk, Prog. Part. Nucl. Phys. **66**, 782 (2011).

[40] P. G. Blunden, W. Melnitchouk, and J. A. Tjon, Phys. Rev. Lett. **91**, 142304 (2003).

[41] S. Kondratyuk, P. G. Blunden, W. Melnitchouk, and J. A. Tjon, Phys. Rev. Lett. **95**, 172503 (2005).

[42] S. Kondratyuk and P. G. Blunden, Phys. Rev. C **75**, 038201 (2007).

[43] D. Borisyuk and A. Kobushkin, Phys. Rev. C **78**, 025208 (2008).

[44] P. G. Blunden, W. Melnitchouk, and J. A. Tjon, Phys. Rev. C **72**, 034612 (2005).

[45] D. Borisyuk and A. Kobushkin, Phys. Rev. C **74**, 065203 (2006).

[46] Y.-C. Chen, A. Afanasev, S. J. Brodsky, C. E. Carlson, and M. Vanderhaeghen, Phys. Rev. Lett. **93**, 122301 (2004).

[47] A. V. Afanasev, S. J. Brodsky, C. E. Carlson, Y.-C. Chen, and M. Vanderhaeghen, Phys. Rev. D **72**, 013008 (2005).

[48] D. Borisyuk and A. Kobushkin, Phys. Rev. D **79**, 034001 (2009).

[49] N. Kivel and M. Vanderhaeghen, Phys. Rev. Lett. **103**, 092004 (2009).

[50] I. A. Rachek *et al.*, Phys. Rev. Lett. **114**, 062005 (2015).

[51] D. Rimal *et al.* (The CLAS Collaboration), Phys. Rev. C **95**, 065201 (2017).

[52] B. S. Henderson *et al.* (OLYMPUS Collaboration), Phys. Rev. Lett. **118**, 092501 (2017).

[53] J. Arrington, W. Melnitchouk, and J. A. Tjon, Phys. Rev. C **76**, 035205 (2007).

[54] F. Iachello, A. Jackson, and A. Lande, Phys. Lett. B **43**, 191 (1973).

[55] C. Perdrisat, V. Punjabi, and M. Vanderhaeghen, Prog. Part. Nucl. Phys. **59**, 694 (2007).

[56] E. L. Lomon, Phys. Rev. C **66**, 045501 (2002).

[57] S. J. Brodsky and G. R. Farrar, Phys. Rev. D **11**, 1309 (1975).

[58] A. V. Belitsky, X. Ji, and F. Yuan, Phys. Rev. Lett. **91**, 092003 (2003).

[59] M. Guidal, M. V. Polyakov, A. V. Radyushkin, and M. Vanderhaeghen, Phys. Rev. D **72**, 054013 (2005).

[60] W. Bertozzi *et al.* (E12-07-108 Collaboration), *Precision Measurement of the Proton Elastic Cross Section at High Q^2*, Jefferson Lab PAC32 Proposal (2007).

[61] J. Roche *et al.* (E12-06-114 Collaboration), *Measurements of the Electron-Helicity Dependent Cross Sections of Deeply Virtual Compton Scattering with CEBAF at 12 GeV*, Jefferson Lab PAC30 Proposal (2006).

[62] Y. Wang, *Measurement of the Elastic ep Cross Section at Q^2 = 0.66, 1.10, 1.51 and 1.65 GeV^2*, Ph.D. thesis, College of William and Mary (2017).

[63] F. Gross, J. Phys.: Conf. Ser. **299**, 012001 (2011).

[64] Jefferson Lab 12 GeV Upgrade, `https://www.jlab.org/12GeV/`.

[65] R. Kazimi, in *Proceedings of the 4th International Particle Accelerator Conference* (2013) p. 3502.

[66] D. Marchand, Ph.D. thesis, University of Blaise Pascal, Clermont-Ferrand (1997).

[67] J. Alcorn *et al.* (Jefferson Lab Hall A Collaboration), Nucl. Instrum. Meth. A **522**, 294 (2004).

[68] K. Unser, IEEE Trans. Nucl. Sci. **28**, 2344 (1981).

[69] W. Barry *et al.*, *Beam Position Measurement in the CEBAF Recirculating Linacs by Use of Pseudorandom Pulse Sequences*, JLAB-TN-90-246 (1990).

[70] W. Barry *et al.*, *Basic Noise Considerations for CEBAF Beam Position Monitors*, JLAB-TN-91-087 (1991).

[71] Hall A Rasters, `https://hallaweb.jlab.org/wiki/index.php/Raster`.

[72] D. Meekins, *Hall A Target Configuration*, Jefferson Lab Target Group (2016), available at `http://hallaweb.jlab.org/12GeV/experiment/E12-07-108/Documents/Target/Fall2016/HallATargetConfiguration10-11-16.pdf`.

[73] *Thermophysical Properties of Fluid Systems*, National Institute of Standards and Technology, `https://webbook.nist.gov/chemistry/fluid/`.

[74] J. R. Arrington, *Inclusive electron scattering from nuclei at $x > 1$ and high Q^2*, Ph.D. thesis, California Institute of Technology (1998).

[75] B. Schmookler, in *Hall A Collaboration Meeting* (Jefferson Lab, 2014).

[76] K. Fissum *et al.*, Nucl. Instrum. Meth. A **474**, 108 (2001).

[77] W. R. Leo, *Techniques for Nuclear and Particle Physics Experiments: A How-to Approach*, 2nd ed. (Springer-Verlag, Berlin, Heidelberg, 1994).

[78] F. Sauli, *Gaseous Radiation Detectors: Fundamentals and Applications*, Cambridge Monographs on Particle Physics, Nuclear Physics and Cosmology (Cambridge University Press, Cambridge, 2014).

[79] HRS Focal Plane Polarimeter, `http://hallaweb.jlab.org/equipment/detectors/fpp.html`.

[80] X. Zhan, *High Precision Measurement of the Proton Elastic Form Factor Ratio at Low Q^2*, Ph.D. thesis, Massachusetts Institute of Technology (2010).

[81] M. K. Jones, C. Perdrisat, and V. Punjabi, *Manual for Front Chambers of the FPP* (1996), `https://userweb.jlab.org/~jones/fpp/manual_front_chambers.html`.

[82] L. Lagamba *et al.*, Nucl. Instrum. Meth. A **471**, 325 (2001).

[83] M. Iodice *et al.*, Nucl. Instrum. Meth. A **411**, 223 (1998).

[84] D. Green, *The Physics of Particle Detectors*, Cambridge Monographs on Particle Physics, Nuclear Physics and Cosmology (Cambridge University Press, Cambridge, 2005).

[85] C. Grupen and B. Shwartz, *Particle Detectors*, 2nd ed., Cambridge Monographs on Particle Physics, Nuclear Physics and Cosmology (Cambridge University Press, Cambridge, 2008).

[86] Y. Qiang, *Search for Pentaquark Partners Θ^{++}, Σ^0 and N^0 in H(e,e'K(π))X Reactions at Jefferson Lab Hall A*, Ph.D. thesis, Massachusetts Institute of Technology (2007).

[87] L. Ou and V. Sulkosky, *Number of Photoelectrons for HRS Cherenkovs*, E12-07-108 Technical Note (Jefferson Lab, 2013).

[88] K. Allada, C. Hurlbut, L. Ou, B. Schmookler, A. Shahinyan, and B. Wojtsekhowski, Nucl. Instrum. Meth. A **782**, 87 (2015).

[89] *Materials for EM calorimeters*, Jefferson Lab Experiment E99114, `http://hallaweb.jlab.org/physics/experiments/RCS/public/calorimeter_material.html`.

[90] R. W. Michaels, Hall A Trigger and Data Acquisition (2014), `http://hallaweb.jlab.org/equipment/daq/daq_trig.html`.

[91] CODA, `https://coda.jlab.org/drupal/`.

[92] E. Jastrzembski, *Trigger Supervisor: Version 2*, Jefferson Lab Data Acquisition Group.

[93] EPICS Home Page, `https://epics.anl.gov/`.

[94] R. W. Michaels, MLU Programming, https://hallaweb.jlab.org/wiki/index.php/MLU_Programming.

[95] V. Sulkosky, *Data Acquisition for the Hall A High Resolution Spectrometers During 12 GeV*, E12-07-108 Technical Note (University of Virginia, 2014).

[96] Hall A Analyzer, https://redmine.jlab.org/projects/podd/wiki.

[97] R. Brun and F. Rademakers, Nucl. Instrum. Meth. A **389**, 81 (1997).

[98] M. Berz, H. Hoffmann, and H. Wollnik, Nucl. Instrum. Meth. A **258**, 402 (1987).

[99] R. W. Michaels, Hall A Raw Data Structure (2005), http://hallaweb.jlab.org/equipment/daq/dstruct.html.

[100] Cryotarget Training (12 GeV Era), available at http://hallaweb.jlab.org/equipment/targets/cryotargets/TOtraining.pptx.

[101] J.-P. Chen, private communication.

[102] L. Ou, E12-07-108 Analysis Log 77 (2017), available at https://hallaweb.jlab.org/dvcslog/Gmp/77.

[103] J. Gomez, private communication.

[104] T. Gautam, Ph.D. thesis, Hampton University (2018).

[105] N. Liyanage, *Optics Calibration of the Hall A High Resolution Spectrometers Using the New Optimizer*, JLAB-TN-02-012 (2002).

[106] R. K. Bock and W. Krischer, *The Data Analysis BriefBook* (Springer-Verlag, Berlin, Heidelberg, 1998).

[107] F. James and M. Winkler, *Minuit2 Manual*, https://root.cern.ch/root/htmldoc/guides/minuit2/Minuit2.html.

[108] D. Flay, *Measurements of the Neutron Longitudinal Spin Asymmetry A_1 and Flavor Decomposition in the Valence Quark Region*, Ph.D. thesis, Temple University (2014).

[109] B. Schmookler, E12-07-108 Analysis Log 16 (2016), available at https://hallaweb.jlab.org/dvcslog/Gmp/16.

[110] B. Schmookler, E12-07-108 Analysis Log 43 (2016), available at https://hallaweb.jlab.org/dvcslog/Gmp/43.

[111] A. Ketikyan, H. Voskanyan, and B. Wojtsekhowski, *About Shower Detector Software*, Technical Note (Jefferson Lab, 1997).

[112] D. Meekins, private communication.

[113] J. Huang, *Double Spin Asymmetry A_{LT} in Charged Pion Production from Deep Inelastic Scattering on a Transversely Polarized ^{3}He Target*, Ph.D. thesis, Massachusetts Institute of Technology (2012).

[114] ROOT: Data Analysis Framework, `https://root.cern.ch/`.

[115] `ROOT::Math::Minimizer` Class Reference, `https://root.cern.ch/doc/master/classROOT_1_1Math_1_1Minimizer.html`.

[116] S. Dymov, V. Kurbatov, I. Silin, and S. Yaschenko, Nucl. Instrum. Meth. A **440**, 431 (2000).

[117] `ROOT::Math::GSLmultiFit` Class Reference, `https://root.cern/doc/master/classROOT_1_1Math_1_1GSLMultiFit.html`.

[118] M. Avriel, *Nonlinear Programming: Analysis and Methods* (Dover Publishing, 2003).

[119] J. Mougey, *ESPACE Energy Loss Corrections Revisited*, E89044 Analysis Progress Report (2000).

[120] C. Patrignani *et al.* (Particle Data Group), Chin. Phys. C **40**, 100001 (2016).

[121] R. C. Walker, *A Measurement of the Proton Elastic Form Factors for* $1 \leq Q^2 \leq 3$ (GeV/c)^2, Ph.D. thesis, California Institute of Technology (1989).

[122] T. Gautam, E12-07-108 Analysis Log 165 (2018), available at `https://hallaweb.jlab.org/dvcslog/Gmp/165`.

[123] T. Gautam, E12-07-108 Analysis Log 185 (2018), available at `https://hallaweb.jlab.org/dvcslog/Gmp/185`.

[124] O. Hansen, in *Hall A Weekly Meeting* (2014) available at `https://userweb.jlab.org/~brads/bethe-heitler/VDC_tracking/HRS-Tracking-HallAMtg.pdf`.

[125] T. Gautam, *Charge Calibration at Hall A*, E12-07-108 Technical Note (2018).

[126] B. Schmookler and B. Aljawrneh, *Efficiency Studies for the GMp Experiment*, E12-07-108 Technical Note (2018).

[127] SIMC Monte Carlo, `https://hallcweb.jlab.org/wiki/index.php/SIMC_Monte_Carlo`.

[128] L. Ou, E12-07-108 Analysis Log 149 (2017), available at `https://hallaweb.jlab.org/dvcslog/Gmp/149`.

[129] L. C. Maximon and J. A. Tjon, Phys. Rev. C **62**, 054320 (2000).

[130] Y. S. Tsai, Phys. Rev. **122**, 1898 (1961).

[131] L. W. Mo and Y. S. Tsai, Rev. Mod. Phys. **41**, 205 (1969).

[132] Y. S. Tsai, *Radiative Corrections to Electron Scatterings*, SLAC-PUB-848 (1971).

[133] S. D. Drell and S. Fubini, Phys. Rev. **113**, 741 (1959).

[134] R. Ent, B. W. Filippone, N. C. R. Makins, R. G. Milner, T. G. O'Neill, and D. A. Wasson, Phys. Rev. C **64**, 054610 (2001).

[135] J. Schwinger, Phys. Rev. **76**, 790 (1949).

[136] N. C. R. Makins, *Measurement of the Nuclear Dependence and Momentum Transfer Dependence of Quasielastic* $(e, e'p)$ *Scattering at Large Momentum Transfer*, Ph.D. thesis, Massachusetts Institute of Technology (1994).

[137] D. Dutta, *Radiative Corrections—The SIMC Way*, Technical Note.

[138] M. E. Christy and P. E. Bosted, Phys. Rev. C **81**, 055213 (2010).

[139] P. E. Bosted and V. Mamyan, "Empirical Fit to electron-nucleus scattering," (2012), arXiv:1203.2262 .

[140] J. C. Bernauer, *Measurement of the elastic electron-proton cross section and separation of the electric and magnetic form factor in the* Q^2 *range from 0.004 to 1* $(\mathrm{GeV}/c)^2$, Ph.D. thesis, Johannes Gutenberg-Universität Mainz (2010).

[141] P. E. Bosted, Phys. Rev. C **51**, 409 (1995).

[142] N. Kivel and M. Vanderhaeghen, J. High Energy Phys. **04**, 029 (2013).

[143] E. L. Lomon, *Effect of revised* R_n *measurements on extended Gari-Krümpelmann model fits to nucleon electromagnetic form factors*, MIT-CTP-3765 (Massachusetts Institute of Technology, 2006) arXiv:nucl-th/0609020 .

[144] M. Gari and W. Krümpelmann, Phys. Lett. B **274**, 159 (1992).